ABSTRACT

Title of Dissertation: MICROBRIDGE FORMATION FOR LOW RESISTANCE INTERLINE CONNECTION USING PULSED LASER TECHNIQUES

Kuan-Jung Chung, Doctor of Philosophy, 2005

Directed By: Associate Professor Joseph B. Bernstein
Department of Mechanical Engineering
Department of Electric and Computer Engineering

MakeLink® technology has been applied in many semiconductor devices to achieve high performance. Sometimes one-type-link design doesn't make desirous links for all IC manufacturing processes. In this work, four new structures, called microbridge, were designed to form all types of link. Laser processing experiments were performed to verify the designs. The results show that two-lower-level-metal-line design has higher performance (low link resistance), higher productivity (broad energy window), and higher yield than the three-lower-level-metal-line design. Therefore, it can be considered as the optimal design from the processing point of view. Two-lower-level-metal-line with lateral gap structure provides better scalability and it can be used in next generation ICs. If high-speed is the primary concern, an advanced-lateral structure is best, corresponding to its much lower resistance. The reliability tests indicate that the median-times-to-failure of all test structures are greater than nine years in operating condition, presenting reasonable lifetimes for integrated circuits used in the market.

A two-dimensional finite element plane models for microbridge formation is developed. Results are compared to the experiments with process windows to present their consistence. The model allowed for using different geometric parameters and metal-dielectric combinations optimizing the design. An optimal design diagram for the Al/SiO_2 system is created to provide the designer with criteria to avoid the failure of structure. Trade-off requirements, such as process window and structure size, are also provided. Guidelines are obtained for the Cu/Low-K dielectric system.

MICROBRIDGE FORMATION FOR LOW RESISTANCE INTERLINE CONNECTION USING PULSED LASER TECNIQUES

By

Kuan-Jung Chung

Dissertation submitted to the Faculty of the Graduate School of the
University of Maryland, College Park, in partial fulfillment
of the requirements for the degree of
Doctor of Philosophy
2005

Advisory Committee:

Associate Professor Joseph B. Bernstein, Chair/Advisor
Professor Martin C. Peckerar, Dean's Representative
Professor Ali Mosleh
Professor John Melngailis
Associate Professor Carol Smidts

Dedication

To my parents, and my wife Li-Yun

Acknowledgements

I am glad to thank my advisor, Professor Joseph Bernstein, for the time and encouragement given to me during this work. Without his support, this document would not exist. I would like to specially thank professor Martin Peckerar, for his valuable advises to the outline, FE simulation, and design optimization of my dissertation. And I acknowledge the consenting to join the advisory committee and reviewing this dissertation of Professor Ali Mosleh, Professor John Melngailis, and Professor Carol Smidts. I would also like to thank all of the laser processing group members for their help.

I deeply thank to my parents for their selfless love to support me all the time. And my warm and grateful appreciation goes to my wife, Li-Yun (Lori), for her understanding and encouragement during the preparation of this dissertation.

Finally, I would like to express my special thanks to the Tao members. And I sincerely appreciate all to God who kindly leads my life to the right way and allow me to finish this work.

Table of Contents

List of Tables

List of Figures

Chapter1: Introduction

1.1 Laser Processing Semiconductor Devices

The first flash lamp-pumped ruby laser was created in 1960, using microwave tubes and transistor to push the upper limit of coherent electronics from the millimeter wave range out to include the sub-millimeter, infrared, visible, ultraviolet spectral regions [1]. In the early years of laser development for materials processing, laser was regarded by engineers as " an alternative expensive solution of the problem." But now laser processing materials has become a significant part of this field since more and more "problems" are solved by affordable and efficient lasers. New applications of laser processing materials continue to be found ranging from medical to semiconductor industry.

Methods of laser repair for integrated circuits (IC) chips exhibiting large-scale design redundancy have been improved for yield enhancement [2]. A short pulse laser is employed to remove defective elements and replace them with redundant ones. In present semiconductor manufacturing, the laser is general used to cut metal lines. This has become increasingly difficult to

achieve due to the development of multilevel metallization processes. The lower corner cracks of the metal lines were demonstrated to be unfavorable for the electrical disconnection of the fuse, as it leads to the low yields and eventually becomes the limit for the laser energy process window [3].

A complementary, laser formed connection called **MakeLink**®[1] has much greater promise for future redundant and programmatic requirements. Different laser-induced metal anti-fuse structures have been developed and some of them have shown wide process windows and high yields [4]-[7]. Therefore, many applications of using MakeLink, such as Laser PROM, laser field programmable gate array and analog array (LFPGA and LFPAA), have been developed to achieve high performance.

The designs of the MakeLink, developed by Bernstein et al, can be classified to lateral-link and vertical-link. Lateral-link structure is a direct metal-to-metal connection between two adjacent metal lines on the same level of metallization. The laser pulse energy causes the thermal expansion of metal, which cracks the dielectrics, then the molten metal fills the crack to

[1] MakeLink is a US registered trademark for laser programmed 'microbridge' connections, owned by Professor Joseph B. Bernstein from the University of Maryland.

form the link [6] [8]. Vertical-link is formed by the same mechanism but the link connection is between two different levels of metallization.

The primary advantage of the lateral-link is its low resistance due to its geometric "short" arm. Designers prefer to use this structure since it is able to achieve the requirement of low power consumption for more dense integrated circuits. The structure is generally laid out at the upper-level interconnect layer to result in a narrow energy window than that of vertical-link in order to avoid cracking passivation. Additionally, vertical-link structure presents higher reliability due to his geometric "strong" arm [9] [10].

Sometimes, these structures do not form desirous-links in all processes. That means undesirable cracks may occur due to the process and material variations by different manufacturers. For example, in previous work, we found the undesirable lower corner lateral cracks occurred in some vertical-link design, shown in fig. 1.1. However, the same vertical-link design was proven to be successful for the other manufacturer's process, shown in fig. 1.2. To overcome this issue, we need to design a novel architecture, which is able to form both inter- and intra-level connections after laser processing. Further

note, the new structure is necessary to meet the requirements of low power consumption (low resistance), high yields, and high scalability for the future applications. In this study, we refer to the laterally oriented, interlayer MakeLink as a "**Microbridge**" to be the new design. Four new structures of forming microbridge were presented, and some experiments were performed to verify the designs involving process development, scalability tests, and reliability tests.

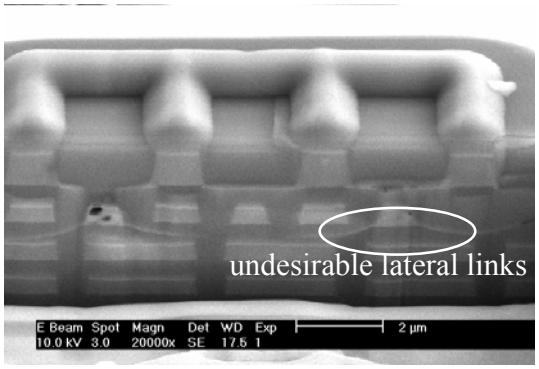

Fig. 1.1 The case of undesirable lateral links at vertical-link design

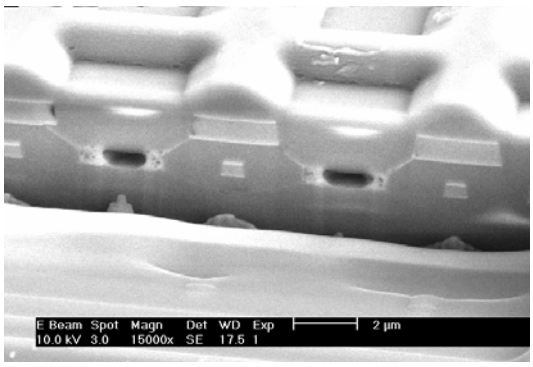

Fig. 1.2 The case of desirous-vertical-links at vertical-link design

1.2 Simulation of Microbridge Formation

The process of forming microbridge within the interconnect layer with a pulsed laser is quite complex, involving thermal transfer by a pulsed heat source, thermal stress generated by the conductivity mismatch between the metal line and dielectric and crack formation in dielectric. A lot studies have been focused on the short-pulse laser heating process with a free air boundary. For instance, Cohen and Bernstein, etc [11][12][13], obtained some closed-forms with the process of melting a thin conducting film using a pulsed laser. Yilbas developed a finite element model to do thermo-elasto-plastic analysis for short-pulse laser heating process [14]. These study don't involve the crack formation and a restricted boundary in this problem. On the other hand, according to author's survey, there is no publication yet to present the research in fracture behavior of ceramic suffered from extra fast thermal shock with the nano-second pulsed laser in a micro-scale region. Therefore, it is necessary to create a new model simultaneously considering thermal response and fracture behavior for a micro-scale sample with a restricted boundary to simulate the microbridge forming process.

It is impossible to obtain analytic solution in the case of multilevel interconnects of microelectronic device, which usually deposit inter-level dielectric around conducting lines to form confined boundary. Instead, a numerical method is required in order to obtain approximate solution. To simulate the microbridge formation, Finite element method (FEM) is applied since it is able to find the solution for this complicated problem by replacing it by a simpler one. Moreover, it is possible to improve or refine the approximate solution by spending more computational effort [15]. In this work, a general-purpose finite element software code, called ANSYS®[2], is applied to generate the thermomechanical and fracture coupled model of the microbridge formation.

In our study, we rely on methods described by Frewin [16]. Frewin used a finite element model for pulsed laser welding process. He reports that the weld dimensions are a strong function of the absorptivity and energy distribution of the laser beam. A proper heat source is able to improve the welding quality. In

[2] ANSYS ® is a registered trademark of Swanson Analysis Systems, Inc.

other words, an optimal dimension/laser energy combination is able to increase structure performance, production yield, and reliability.

In this work, the finite element model is applied to optimize the design of the structure using various geometric parameters such as interline spacing of two metal lines as well as width-to-height ratio of the metal line for two metal-dielectric combinations, Al/SiO_2 and Cu/Low-k. Results are compared to the experiments with process windows. The structure was fabricated using a commercial 0.18 μm *CMOS* process with aluminum (1% Silicon and 0.5% Copper) and silicon dioxide interconnect combination. A " optimal design parameter zone" diagram for the Al/SiO_2 system is created to provide the designer criteria for avoiding unformed links. Using our model, the designer can study trade-off requirements such as resistance and size for improving yield. Design Guidelines for the Cu/Low-k will be shown.

1.3 Objectives, Organization, and Contributions

In order to proceed the applications of the microbridge to practical devices produced by next generation semiconductor processes, the goal of this work is

to find the optimal design for the new microbridge structure, which possesses high performance (low resistance), high productivity (wide process window), high scalability, high yield, and high reliability. Accordingly, there are three main parts in this research except introduction (chapter 1), and conclusions as well as future work (chapter 8):

1. Chapter 2, which presents theories of microbridge formation.
2. Chapters from 3 to 5 to show the experiments involving process development, scalability tests, and reliability tests for microbridge structure.
3. Chapter 6 and 7, which demonstrate the details of simulations involving finite element analysis and design optimization.

Chapter 2 introduces the theory of heat conduction by a pulsed laser source, the relationship of stress and strain caused by thermal effect, and fundamental theory of fracture mechanics involving the stress intensity factors for three failure modes.

Chapter 3 presents laser processing experiments to verify the designs of four test structures. We setup an optimal laser spot size to be 3.5 μm for large

structures. The process windows displaying the link resistances in different energies for 100% yields were obtained. Some pilot runs were performed to evaluate the yield for each structure.

An experiment-based scalability estimation for the small structures is presented in chapter 4. As the results, we predict the robust design for next generation IC applications. Chapter 5 shows the reliability assessment by electromigration tests to calculate the median time to failures at operating and storage temperatures.

A new finite element model involving thermal response and fracture behavior of materials for the microbridge formation is presented in Chapter 6. Results are compared to the experiments with process windows. Chapter 7 shows optimal design diagram for the Al/SiO_2 system. Design Guidelines for the Cu/Low-k will be shown.

In summary, there are five unique contributions in this work:

1. We design new microbridge structures using 0.18 μm semiconductor interconnect processes and verified by laser processing experiments.

They demonstrate high performance (low resistance), high productivity (broad process windows), and high yields.

2. We scale down the size of these structures and then successfully verified by laser processing experiments.

3. We performed electromigration tests to assess the reliability of these structures. The median times to failure of these structures meet the requirements of lifetimes of ICs used in the market.

4. We developed finite element model coupled with heat conduction by a pulsed heat source, thermal stress-strain as well as fracture mechanics. The results of the FE analysis for microbridge formation are consistent with the experimental results. This demonstrates the model's ability to predict the success of more complex processes and patterns. .

5. We derived an optimal design diagram from FE simulations to provide the designer with maximum link yield for a given set of requirements (such as resistance and size).

Chapter 2: Theories

2.1 Introduction

The process of forming microbridge using pulse laser in the interconnect layers of ICs is complicated, involving thermal transfer by a pulsed heat source, thermal stress generated by the conductivity mismatch between the metal line and dielectric, and crack formation in dielectric. The purpose of this chapter is to introduce theories involved in this process as fundamental for modeling. In this chapter, section 2.1 presents the conduction theory with a pulsed heat source. For the microbridge formation it states the transient temperature distribution of the structure in the period of laser processing.

Section 2.2 describes the relationships of thermal stress and strain due to the mismatch of conductivity between aluminum and silicon dioxide while thermal loading is applied. Section 2.3 introduces the fracture mechanics with stress intensity factor, which is used to as the failure criterion of forming the microbridge.

2.2 Heat Conduction

Heat conduction is the essential thermal energy transport phenomena in solid system. Energy is moved through solid materials when temperature gradients exist inside them. The Fourier law can be applied to generate the energy conservation statement where heat may be conducted at a point in a Cartesian frame [17]:

$$\frac{\partial}{\partial x}\left(k\frac{\partial T}{\partial x}\right)+\frac{\partial}{\partial y}\left(k\frac{\partial T}{\partial y}\right)+\frac{\partial}{\partial z}\left(k\frac{\partial T}{\partial z}\right)+\dot{q}=\rho c\frac{\partial T}{\partial t} \qquad 2\text{-}1$$

The form of the heat conduction equation for pulse laser application describes in following [11]:

(a) the temperature is promised to be unsteady (time dependent),

(b) the internal heat effect $\dot{q}$ presents the laser heat source,

(c) the specific heat c, the thermal conductivity k, and the density ρ are all temperature dependent, and

(d) ρcT is ignored to the latent heat of melting regarding its small contribution.

The laser heat source imposed by a pulsed laser presents a short duration of time and confined in space to a small spot. It yields

$$\dot{q}(x,y,z;t) = (1 - R_f)I(x,y,z;t)f(z) \ , \qquad 2\text{-}2$$

where R_f, $I(x,y,z;t)$, and $f(z)$ stand the reflectivity of the target, laser beam's power density, and absorption function of the target respectively.

For the application of microelectronic interconnect system, they are either aluminum or copper. We may simplify to assume that the reflectivity is constant [12]. The beam's power density per unit of volume for a circular symmetry Gaussian beam is defined as,

$$I(x,y,z;t) = \frac{I_0(t)}{\pi x_e^2}\alpha \, exp\left(-\frac{x^2+y^2}{x_e^2}\right) \qquad 2\text{-}3$$

where $I_0(t)$ is the time-dependent laser intensity at the center of the laser beam, and x_e is the $1/e$ radii of the beam, and α is the absorption coefficient. The temporal profile of the laser intensity is simply treated as increasing linearly

from zero to the half time of the pulse width, then decreasing linearly to zero at the end of the pulse width.

The absorption function may be approximated by $f(y) = exp(-\alpha y)$ if we assume the absorption coefficient to be depth independent [13]. Thus the general form of the Gaussian heat source function is given by

$$\dot{q}(x,y,z;t) = \frac{\alpha(1-R_f)I_0(t)}{\pi x_e^2} exp\left(-\frac{x^2+z^2}{x_e^2}\right) exp(-\alpha y) \ . \qquad 2\text{-}4$$

Form 2-1 states the nonlinear and non-homogeneous second order partial differential equation with a non-uniformed pulse laser heat source, which requires one initial and two boundary conditions. Some closed-form analytic expressions applied to the melting of a thin conducting film on the free air boundary have been obtained by S. Cohen, etc [11], [12], and [13]. Edward proves the magnitude of the temperature profile remains the same type of the pulsed laser (Gaussian intensity distribution) since over the very short duration there is insufficient time for significant amounts of heat to flow in order to equalize the temperature [18]. However, it is impossible to obtain the analytic

solutions in the case of multilevel interconnects of microelectronic device, which usually deposit inter-level dielectric around conducting lines to form confined boundary. A numerical analysis must be developed to solve the complex geometry and multi-materials composition heat transfer problem.

2.3 Thermal Stresses and Strain

The fundamental study of thermal stress theory is in the field of thermoelasticity, which states the behavior of stress and strain in an elastic body, due to a heating, under the simplifying assumption that the influence of the deformation on the temperature field may be neglected [19]. In advance, knowing the temperature distribution obtained from solution of the classic heat conduction equation, which does not contain the term due to the deformation of the body, the displacement equations of the theory of elasticity were solved using the temperature distribution function gotten from equation 2-1. The following will focus on the motion of the elastic solid applied in the mentioned case.

It may be able to state that there exists a particular relationship between stress and strain components in an isotropic elastic solid in an equilibrium condition by generalized Hooke's law [20],

$$\sigma_{ij} = \lambda \varepsilon_{kk} \delta_{ij} + 2\mu \varepsilon_{ij} \qquad 2\text{-}5$$

where

$\lambda = \dfrac{E\nu}{(1+\nu)(1-2\nu)}$, Lamé Constant (E: Young's modulus; υ: Poisson's ratio)

$\mu = G$, shear modulus of elasticity

$\delta_{ij} = \begin{cases} 1, i = j \\ 0, i \neq j \end{cases}$, Kronecker delta.

Considering the absorption of the focus laser energy results in a nonuniform direct heating of the absorbing metallic interconnects filled insulating dielectric, thermal stress is dramatically produced due to the mismatch of strength and thermal expansion coefficient of two different

materials. Thus the coupled thermoelastic equation based on the generalized Hooke's law is given by,

$$\sigma_{ij} = \lambda\varepsilon_{kk}\delta_{ij} + 2\mu\varepsilon_{ij} - \frac{E}{1-2\nu}\alpha\Delta T\delta_{ij} \qquad 2\text{-}6$$

where α is thermal expansion coefficient, and the temperature ΔT is measured relative to the ambient. Form 2-6 is so called Duhamel-Neumann relations.

In the case of a metallic film of cubic symmetry irradiated by axisymmetric laser source in multilevel interconnects, the corresponding matrix form yields

$$\left\{\sigma\right\} = \begin{Bmatrix} \sigma_{rr} \\ \sigma_{zz} \\ \sigma_{\theta\theta} \\ \sigma_{rz} \end{Bmatrix} = \frac{E(1-\nu)}{(1+\nu)(1-2\nu)} \begin{bmatrix} 1 & \frac{\nu}{1-\nu} & \frac{\nu}{1-\nu} & 0 \\ \frac{\nu}{1-\nu} & 1 & \frac{\nu}{1-\nu} & 0 \\ \frac{\nu}{1-\nu} & \frac{\nu}{1-\nu} & 1 & 0 \\ 0 & 0 & 0 & \frac{1-2\nu}{2(1-\nu)} \end{bmatrix} \begin{Bmatrix} \varepsilon_{rr} \\ \varepsilon_{zz} \\ \varepsilon_{\theta\theta} \\ \varepsilon_{rz} \end{Bmatrix} - \frac{E\alpha\Delta T}{1-2\nu} \begin{Bmatrix} 1 \\ 1 \\ 1 \\ 0 \end{Bmatrix} \qquad 2\text{-}7$$

The elements of stress considered in this case are radial stress σ_{rr}, axial stress σ_{zz}, hoop stress, $\sigma_{\theta\theta}$ (θ is the angle that the radius makes with a chosen radial direction), and shear stress, σ_{rz}, the corresponding strains are ε_{rr}, ε_{zz}, $\varepsilon_{\theta\theta}$,

and ε_{rz} respectively. If u_r u_θ and u_z present the related displacements in the cylindrical coordinate, then the relative strains are given by

$$\varepsilon_{rr} = \frac{\partial u_r}{\partial r}$$
$$\varepsilon_{zz} = \frac{\partial u_z}{\partial z}$$
$$\varepsilon_{\theta\theta} = \frac{(u_r + \frac{\partial u_\theta}{\partial \theta})}{r} \qquad \text{2-8}$$
$$\varepsilon_{rz} = \frac{1}{2}(\frac{\partial u_r}{\partial z} + \frac{\partial u_z}{\partial r})$$

Equation 2-7 and 2-8 presents the thermoelastic stress–strain-displacement relationships in the axisymmetric cylindrical coordinate. The special case developed by S. S. Cohen, etc. [21] applied to thin metallic film with free boundary on the top surface of the film to find the minimal power needed for plastic deformation using a simplificative temperature distribution. Considering a real case of forming microbridges between metallic films, which have complex geometry and dissimilar material behavior (metallic films are treated as ductile materials but dielectrics except for low k ones are acted with regard to brittle materials), the close-form solution has its difficulty to be

determined. Instead, a numerical method has to be applied in order to obtain the approximate solution.

2.4 Fracture Mechanics

The discipline of fracture mechanics is focused on the prevention of material fracture according to the analysis of the characteristics of materials. For instance, scientists and engineers perform a series of material toughness tests, and develop a mathematical relationship among toughness, stress, and flaw size in order to obtain safety factors to prevent the possible failures in the materials. Therefore, understanding fracture behavior of the materials is dramatically significant of determining the lifetime of components or products.

In general, the fracture of materials is based on the assumption that cracks inherently exist inside of them. There is a singular stress field at the tip of a crack to lead a stress concentration when applied loads. For certain cracked configurations subjected to external forces, Westergaard, Irwin, Sneddon, Williams, Paris, as well as Sih were among to derive closed-form solutions for the stresses in the body, assuming isotropic linear elastic material behavior

[22][23]. Prior to deriving the stress analysis of crack, three basic modes of loading that a crack can experience, as shown in fig. 2.1, have to be defined. Mode I denotes the tendency of opening the crack when the principal load is applied normal to the crack plane. Mode II corresponds to in-plane shear loading and tends to slide one crack face with regarding to the other. Mode III describes the out-of-plane shear loading, called tearing mode as well. Materials with any one crack body can be loaded in any one of these fracture modes, or a combination of two or three modes.

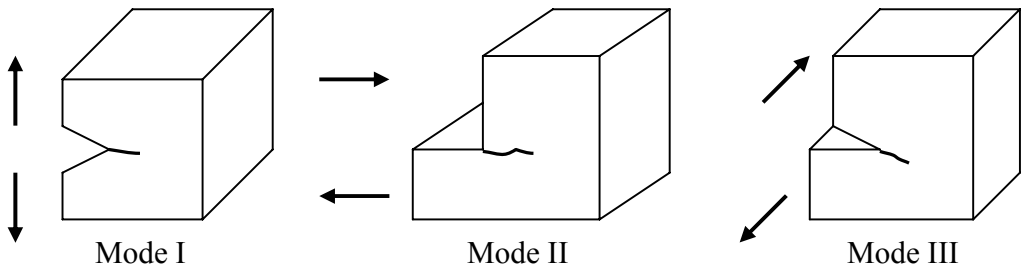

Fig. 2.1 Three basic modes of fracture

A cylindrical coordinate with the origin at the crack tip is illustrated in fig. 2.2. A singularity-dominated zone as the region where describes the ahead crack tip fields regarding to stresses and displacements, assuming linear elastic, isotropic material, is given as following [22],

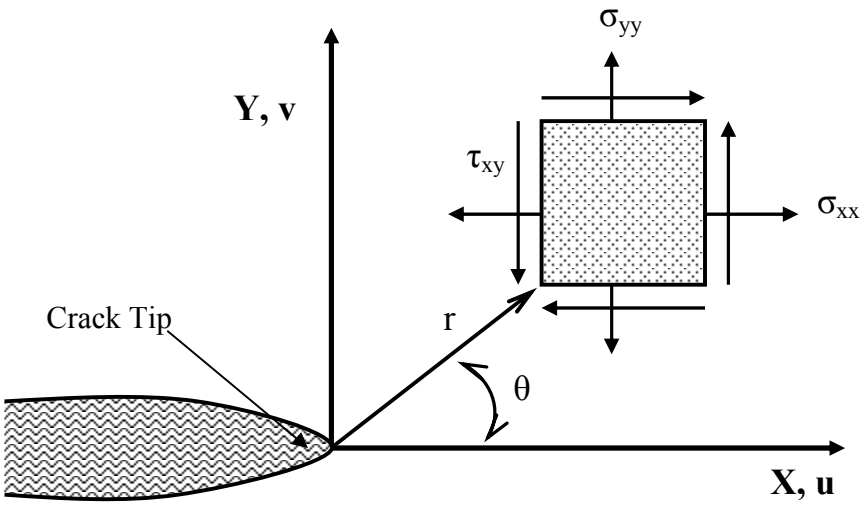

Fig. 2.2 Crack front tip stress field at a cylindrical coordinate (Z axis is normal to the page).

For Mode I,

$$\sigma_{xx} = \frac{K_I}{\sqrt{2\pi r}} cos(\frac{\theta}{2})\left[1 - sin(\frac{\theta}{2}) sin(\frac{3\theta}{2})\right]$$

$$\sigma_{yy} = \frac{K_I}{\sqrt{2\pi r}} cos(\frac{\theta}{2})\left[1 + sin(\frac{\theta}{2}) sin(\frac{3\theta}{2})\right]$$

$$\tau_{xy} = \frac{K_I}{\sqrt{2\pi r}} cos(\frac{\theta}{2}) sin(\frac{\theta}{2}) cos(\frac{3\theta}{2})$$

$$\sigma_{zz} = \begin{cases} 0, & \text{Plane Stress} \\ \nu(\sigma_{xx} + \sigma_{yy}), & \textit{Plane Strain} \end{cases} \qquad \text{2-9}$$

$$u = \frac{K_I}{2G}\sqrt{\frac{r}{2\pi}} cos(\frac{\theta}{2})\left[\eta - 1 + 2 sin^2(\frac{\theta}{2})\right]$$

$$\mathrm{v} = \frac{K_I}{2G}\sqrt{\frac{r}{2\pi}} sin(\frac{\theta}{2})\left[\eta + 1 - 2 cos^2(\frac{\theta}{2})\right]$$

For Mode II

$$\sigma_{xx} = -\frac{K_{II}}{\sqrt{2\pi r}} sin(\frac{\theta}{2})\left[2 + cos(\frac{\theta}{2}) cos(\frac{3\theta}{2})\right]$$

$$\sigma_{yy} = \frac{K_{II}}{\sqrt{2\pi r}} sin(\frac{\theta}{2}) cos(\frac{\theta}{2}) cos(\frac{3\theta}{2})$$

$$\tau_{xy} = \frac{K_{II}}{\sqrt{2\pi r}} cos(\frac{\theta}{2})\left[1 - sin(\frac{\theta}{2}) sin(\frac{3\theta}{2})\right]$$

$$\sigma_{zz} = \begin{cases} 0, & \textit{Plane Stress} \\ \nu(\sigma_{xx} + \sigma_{yy}), & \textit{Plane Strain} \end{cases} \qquad \text{2-10}$$

$$u = \frac{K_{II}}{2G}\sqrt{\frac{r}{2\pi}} sin(\frac{\theta}{2})\left[\eta + 1 + 2 cos^2(\frac{\theta}{2})\right]$$

$$v = -\frac{K_{II}}{2G}\sqrt{\frac{r}{2\pi}} cos(\frac{\theta}{2})\left[\eta - 1 - 2 sin^2(\frac{\theta}{2})\right]$$

For Mode III

$$\tau_{xz} = -\frac{K_{III}}{\sqrt{2\pi r}} sin(\frac{\theta}{2})$$
$$\tau_{yz} = \frac{K_{III}}{\sqrt{2\pi r}} cos(\frac{\theta}{2}) \qquad \text{2-11}$$
$$w = \frac{K_{III}}{G}\sqrt{\frac{r}{2\pi}} sin(\frac{\theta}{2})$$

Where:

υ is Poisson's ratio,

G is the Shear modulus,

u, v, and w are displacement in the cylindrical coordinate, and

K_I, K_{II}, and K_{III} are the stress intensity factor of mode I, II, and III respectively

$$\eta = \begin{cases} 3 - 4\nu, & \text{Plane Strain} \\ \dfrac{3 - \nu}{1 + \nu}, & \text{Plane Stress} \end{cases}$$

The stress intensity factor states the amplitude of the crack tip singularity, which means stresses near the crack tip increase in proportion to K. Furthermore, the stress factor fully defines the crack tip conditions to

determine if the length of the crack keeps propagation as the component is applied loads. It is possible to determine the stress intensity factor if the stress, strain, and displacement relationships of all components are known. For example, the displacements in equations from 2-9 to 2-11 can be simplified in following at $\theta = \pm 180^{\circ}$ by considering the mixed modes:

$$\begin{aligned} u &= \frac{K_{II}}{2G}\sqrt{\frac{r}{2\pi}}(1+\eta) \\ v &= \frac{K_{I}}{2G}\sqrt{\frac{r}{2\pi}}(1+\eta) \\ w &= \frac{2K_{III}}{G}\sqrt{\frac{r}{2\pi}} \end{aligned} \qquad 2\text{-}12$$

For models symmetric about the crack plane called half-crack model, equation 2-12 can be reorganized to give:

$$\begin{aligned} K_{I} &= \sqrt{2\pi}\frac{2G}{1+\eta}\frac{|v|}{\sqrt{r}} \\ K_{II} &= \sqrt{2\pi}\frac{2G}{1+\eta}\frac{|u|}{\sqrt{r}} \\ K_{III} &= 2G\sqrt{2\pi}\frac{|w|}{\sqrt{r}} \end{aligned} \qquad 2\text{-}13$$

Equation 2-13 states the relationships of stress intensity factors and the displacements near crack tip at a certain angle. Generally, if the stress-strain field near crack tip is known, the stress intensity factor can be calculated by solving equations 2-9, 2-10, and 2-11. The calculated valve is then compared with the toughness of the material to evaluate the fracture situation under the loading.

In this work, microbridges were formed by cracking dielectrics between adjacent metals due to the thermal stress caused by the laser power on the surface of the metal. It is understood that the cracking process will start in the corner of the metal line when the thermal stress exceeds the material toughness corresponding to the stress intense factor. Therefore, there exists a threshold laser power to crack the dielectric in order to create the connection between metal lines. But when applying too much laser energy, the microbridge will be destroyed due to the melting of the dielectrics or passivation layer around connections. Therefore, it is possible to have a laser energy window, which declare that there are some adequate laser energies to make connections in this process.

Chapter 3: Laser Process Development Formed Interconnect

3.1 Introduction

As previously mentioned, the “traditional” lateral-link or vertical-link structures do not form desirous-links in all processes offered from the worldwide semiconductor foundries. Moreover, the continuous shrinking of electronic device dimensions extremely requires metal interconnects to possess lower resistance in order to reduce the energy consumption and heat management cost. Therefore, four new structures of laterally oriented, interlayer MakeLink as a microbridge, are presented in this chapter.

The first part of this chapter shows design considerations and layout details of these structures. The metal lines of structure 1, 2, and 3, which is able to form lateral and vertical links, are laid in the lower level of second top two metallization layers. Structure 4 is a new lateral-link structure to provide the comparison with other designs in structure performance (e.g. low resistance), productivity (e.g. energy window), and reliability (e.g. lifetime).

The second portion of this chapter covers laser processing experiments to verify the design of these test structures. The experiments were performed using different laser energies at an optimal laser spot size. Link resistances, energy windows, and yields are applied as criteria of the verification. FIB (Focused Ion Beam) cross- section pictures of some structures are used to confirm the experimental results. The last section summarizes the results of the process verification.

3.2 Test Chip Design and Its Architecture

There are four types of structures fabricated on a test die, illustrated by fig. 3.1. Each structure was repeatedly laid out to form two unique chains. There are 2016 link cells in a chain. Fig. 3.2 – 3.5 present the more details of chain layout for each structure including single cell and its cross section.

Table 3.1 shows the design considerations of these structures. Structure 1 and 2 are both two-lower-metal-line design, but structure 1 has wider lines than that of structure 2 located at inside rectangular hole regarding to the same size of top metal frame and hence no lateral gap from lines to frame. Thus we

called structure1 to be the both two-lower-metal-line design w/o lateral gap, and structure 2 is the two-lower-metal-line with lateral gap design. Structure 3 is three-lower-metal-line design in order to form two side links when zapping central line. From the morphologic point of view, structure 3 would have higher probability to form lateral links. Compared to structure 1, 2, and 3, structure 4 is the new, called advanced-lateral design, to only form lateral links on the top level metal and hence no alternative vertical connection. It provides comparison with other designs in structure performance (e.g. low resistance), productivity (e.g. energy window), and reliability (e.g. lifetime).

	Frame with lines	**Forming lateral link layer**	**Forming alternative vertical link**	**Redundancy**
Structure 1	Yes	Lower level	Yes	Yes
Structure 2	Yes	Lower level	Yes	Yes
Structure 3	Yes	Lower level	Yes	Yes
Structure 4	Yes	Top level	No	Yes

Table 3.1 Design considerations

The test wafer was fabricated using a commercial 0.18 μm *CMOS* process with five metal layers. Aluminum (1% Silicon and 0.5% Copper) was

sputtered and etched to form lower level metallization (metal 4), lines, and upper level metallization (metal 5), frames. A passivation layer covered the metallization as protection. The aluminum lines were under-deposited and over-deposited with a 0.09 μm thick layer and a 0.05 μm thick layer of *TiN* respectively.

It is noted that the top-layer metallization and the one below have been defined as metal 2 and metal 1, respectively, for simplicity throughout this work, though they are actually metal N and N-1 in the multilevel metallization of this test wafer.

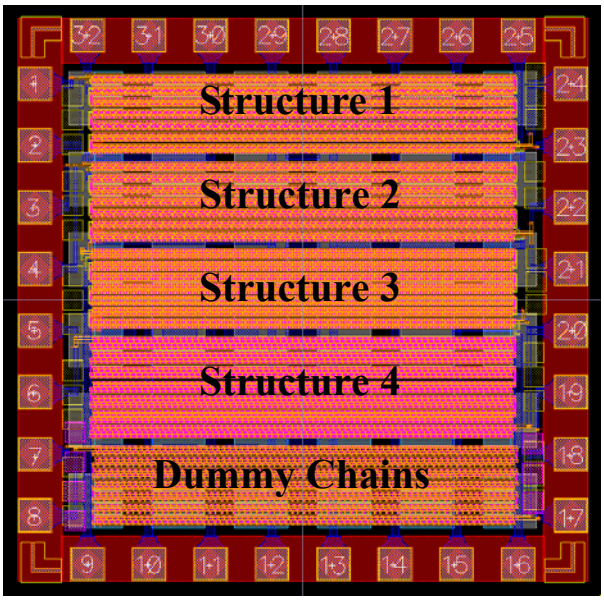

Fig. 3.1 Test chip layout

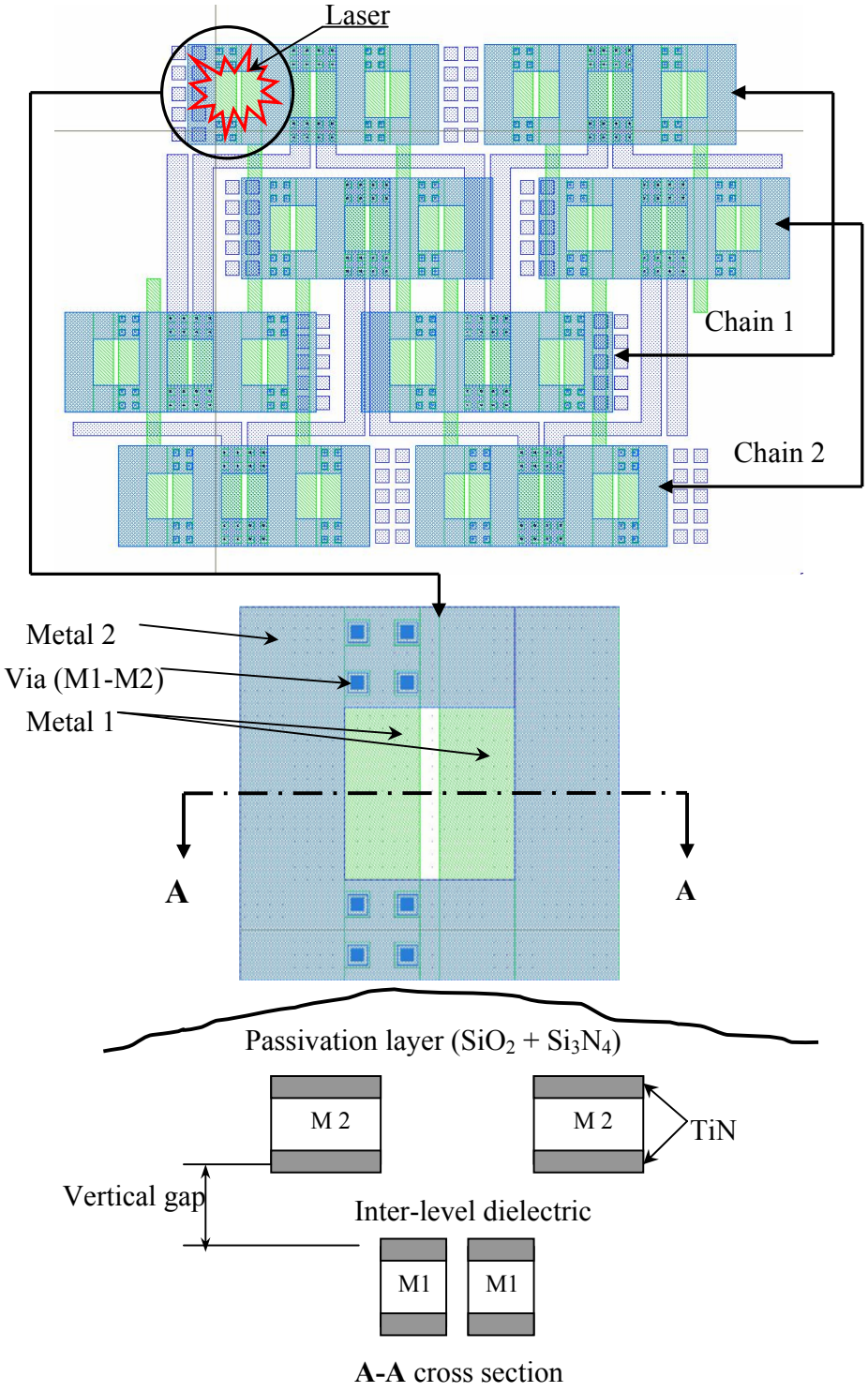

Fig. 3.2 The layout of structure 1

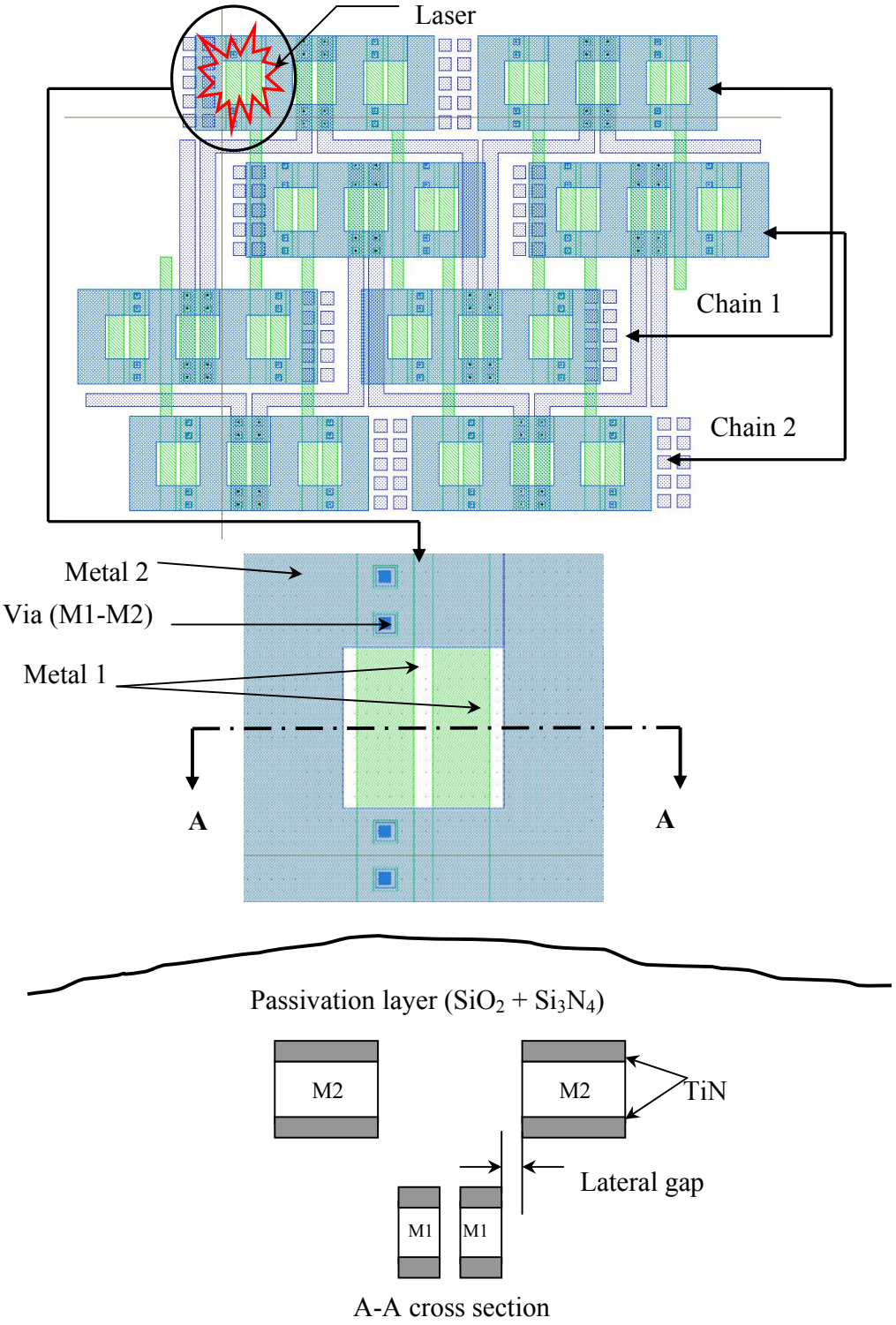

Fig. 3.3 The layout of structure 2

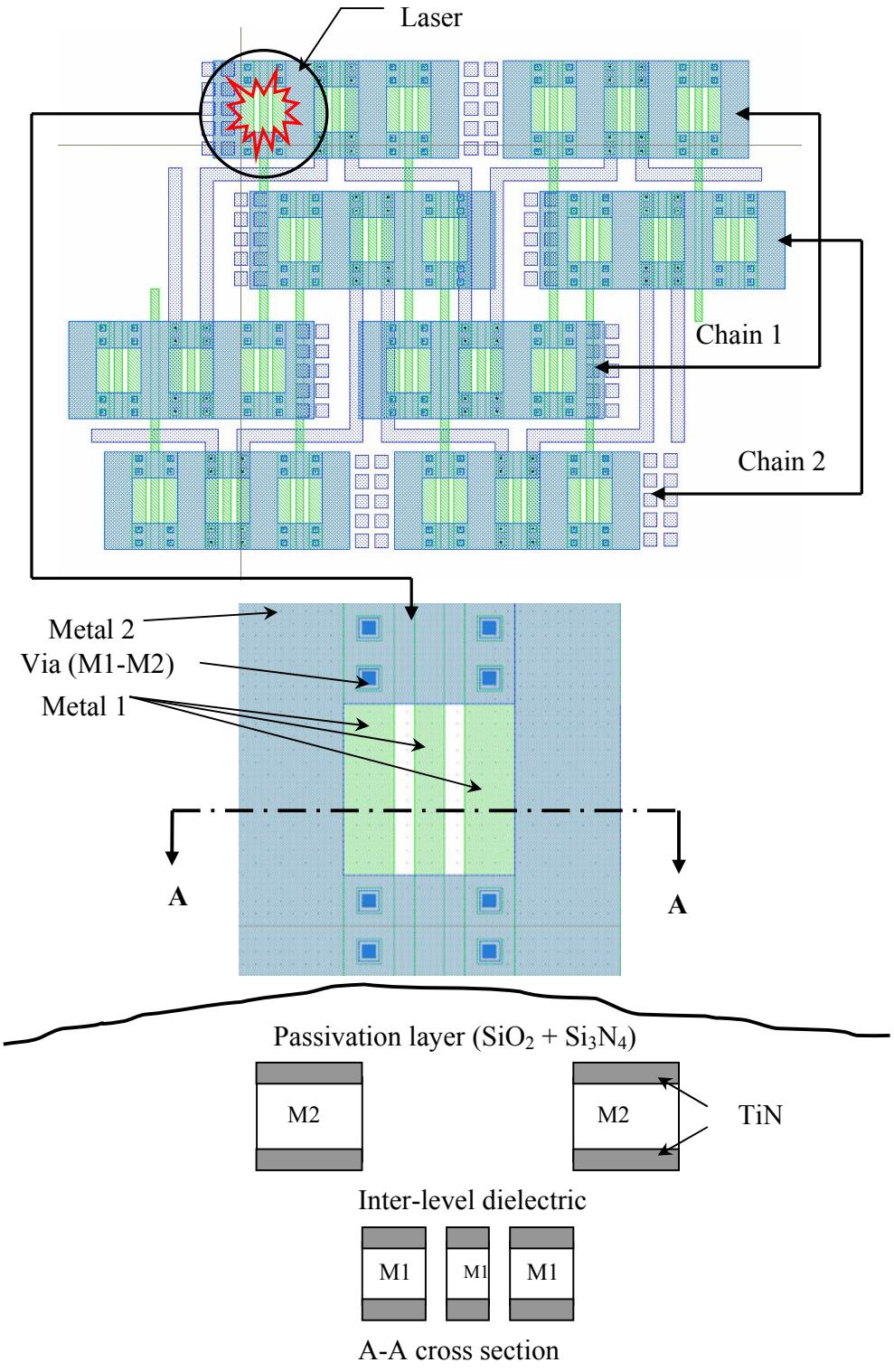

Fig. 3.4 The layout of structure 3

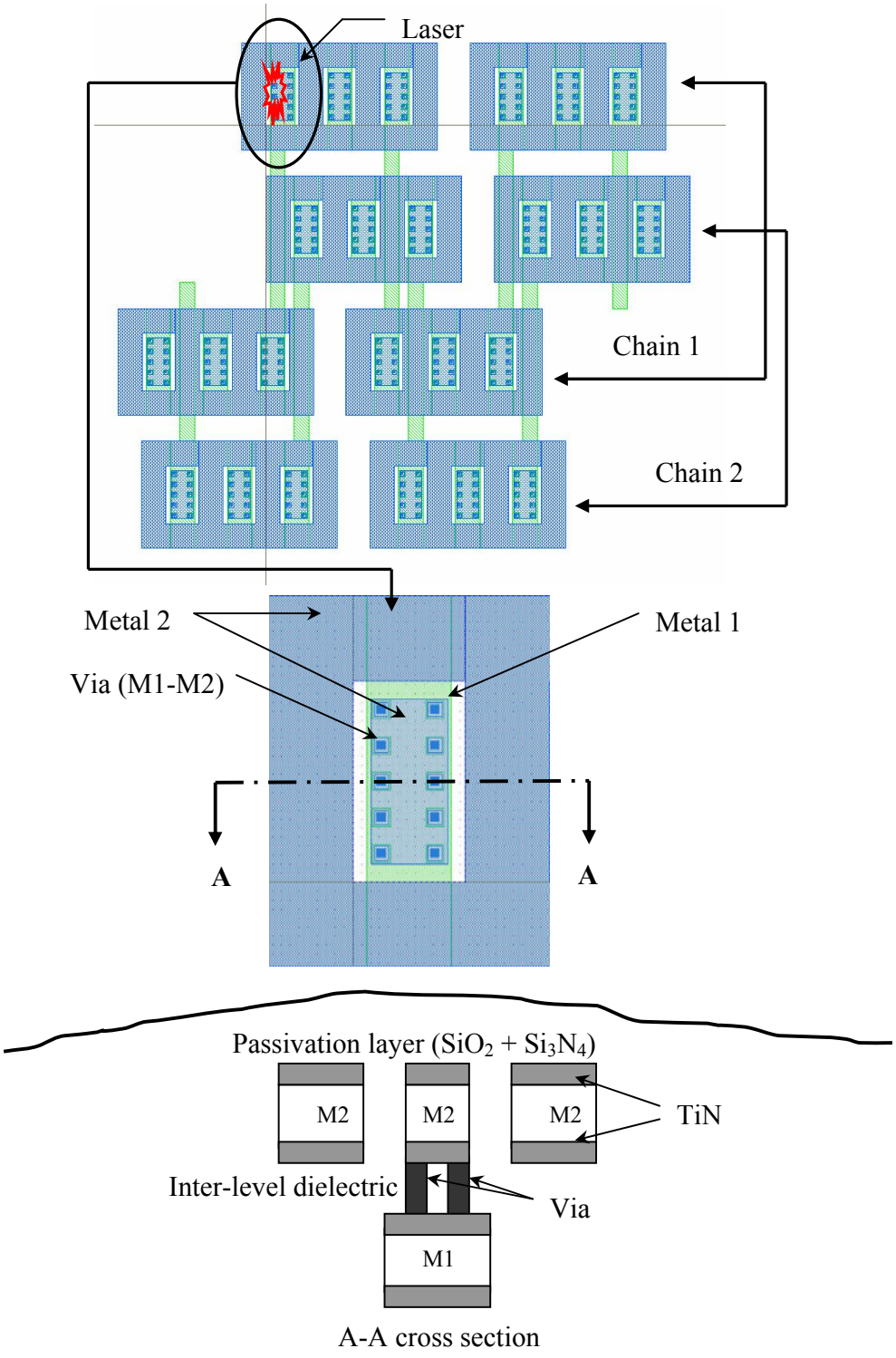

Fig. 3.5 The layout of structure 4

3.3 Experiment Equipment and Instruments

The Laser system used to perform the linking process is ESI 9200 HT PLUS, shown in the fig. 3.6a, which employs a Spectra-Physics diode-pumped, Q-switched, Nd:YLF laser (wavelength:1047 nm) operated in the saturated single-pulse mode. It features a Unix-based workstation, shown in the fig. 3.6b, robotic wafer handling for up to 200 mm wafers, and self-contained clean-room environment. It is geared for submicron devices, offering a beam positioning accuracy of ± 0.5 μm. The laser spot size setup in this experiment was a fixed value 3.5 μm.

Analysis of the processed lateral links was performed using a FEI Dual Beam 620D, Shown in fig. 3.7. It is the powerful instruments combined focused ion beam (FIB) and scanning electron microscope (SEM) to obtain cross-section images of the processed links.

A simple manual probing system, shown in fig. 3.8, was used to measure the resistances of these chains. The value of the chain resistance was divided by 2016 to obtain the average resistance of each link.

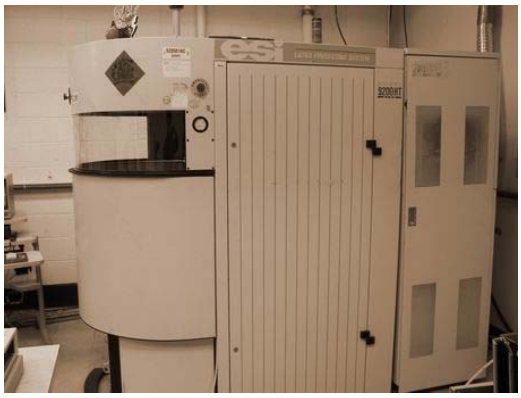

(a) Laser Machine

(b) Unix-based workstation

Fig. 3.6 ESI 9200 HT PLUS laser processing system

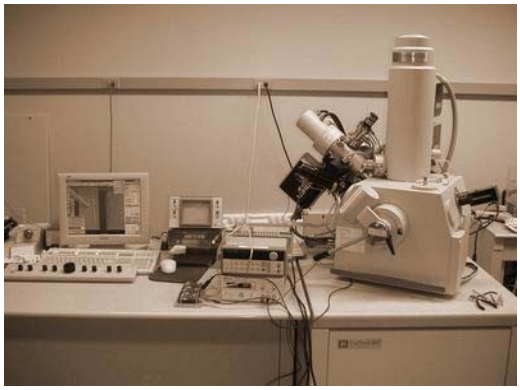

Fig. 3.7 FEI Dual Beam (FIB and SEM) 620D

Fig. 3.8 Manual probing system

3.4 Experimental Procedures

a. Energy run in large dies: thirty (shots) laser pulse were applied to one chain with gradually increased laser energy in order to obtain a potential energy window of each structure. The maximum effective value of the energy window must be lower than the laser energy by which the top passivation layer will be broken.

b. First position run in test dies: laser zapping was performed through the whole chains, and then the chain resistance was measured to obtain a more exact energy window for each structure. The laser focus on the geometric center of the square hole for structure1, 2, and 3, but for structure 4, laser focuses on the central of the gap between the left side frame and the top metal to avoid more severe passivation breaking (Fig. 3.5).

c. Second position run in test dies: a large number of laser zapping were performed for the dies on the corner as well as at the center of the test wafer, and then the chain resistances were measured. The yield and the average resistance of each link for every energy and structure were calculated to decide the optimal link structure and laser energy.

d. Third position run in large dies: laser zapping was performed for the rest of dies on the test wafer to verify the optimal energy and improve the yield.

3.5 Results and Discussion

3.5.1 Process Window

Fig. 3.9 shows the energy windows of each structure and their average resistance with standard deviation (+/-σ) per link. In general, the energy window of these structures was found between 0.15 μJ and 0.3 μJ.

Structure 4 has the lowest average resistance and standard deviation, but it also has the narrowest energy window. The FIB picture, shown in Fig. 3.10, represents the experimental results. The remaining volume of the metal inside the frame hole is adequate to decrease the overall resistance [24]. Compared to other structures' passivation layer 1.8 μm, the thickness of passivation layer of structure 4 is only 0.7 μm since it was laid out on the top layer. Therefore, only small strain energy can easily break its passivation layer to run out of energy window. The results

demonstrate the advantages and disadvantages of later-link structures indicated in chapter 2.

Structure 3, which shows the highest average resistance and standard deviation within the window, indicates that the three-lower-metal-line design characterizes high resistance with a large variation, though it is likely to increase the probability of forming links. Accordingly, this demonstrates two significant design rules based on the experimental results, though all of them were able to get links and process windows. However, for structure 2, 3 and 4, there is a smallest resistance found within the energy window. This is the same result as the early experimental work of vertical links [24], thus optimal laser energy must exist in these advanced-lateral link structures, and the overall resistance will increase with either lower or higher energy.

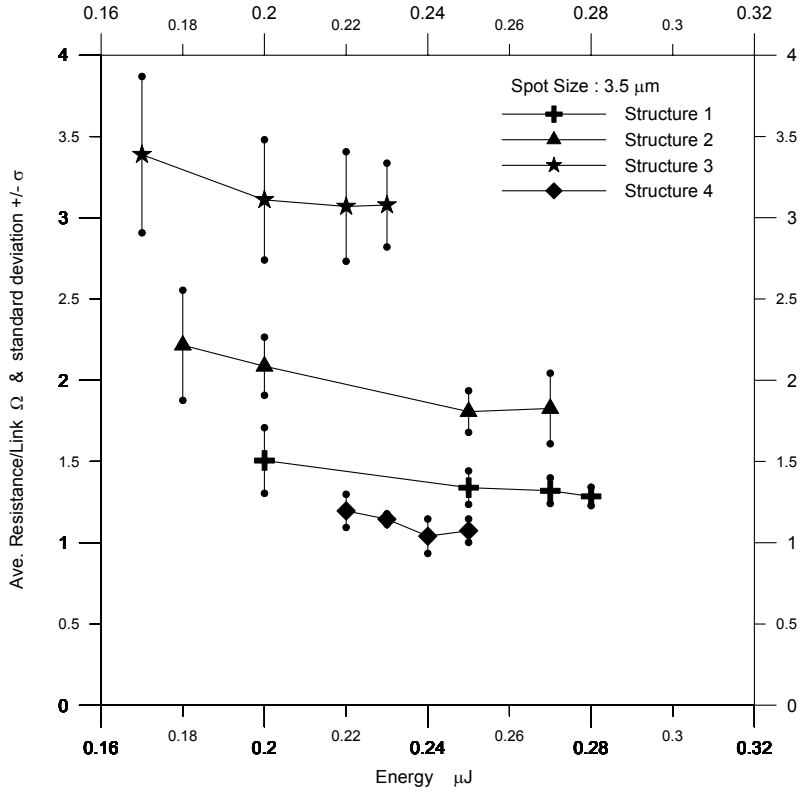

Fig. 3.9 Energy windows of each structure and their average resistance per link with standard deviation

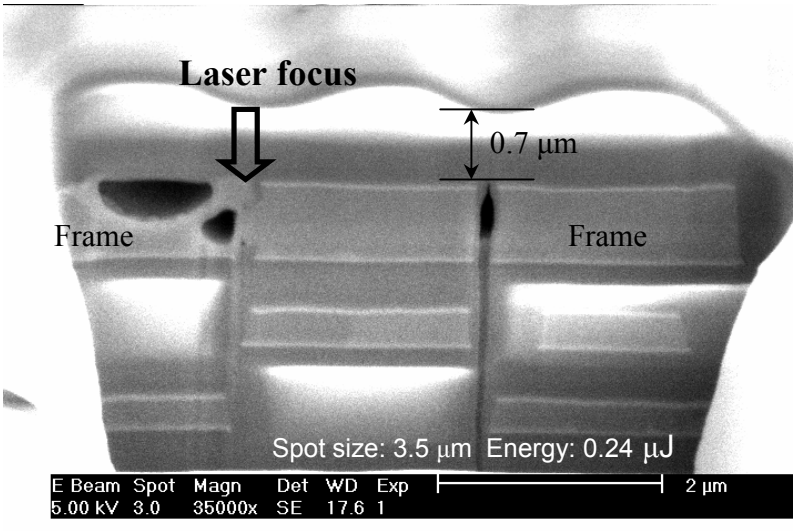

Fig. 3.10 A FIB picture of structure 4

3.5.2 Yield Analysis

Fig. 3.11 shows the chain yield of these structures using energies within their energy windows. The failure modes, chain open and chain short, are also shown in this figure. Chain open means the energy is insufficient to form all links at a chain; on the contrary, due to the use of too much energy, extended cracks between two metal lines can result in a chain short of two different chains.

Compared to other structures, structure 1 is easier to induce short chains due to its small distance between two adjacent Aluminum lines of two chains. A FIB picture, shown in Fig. 3.12, confirms the phenomena that lower corner cracks of Al lines laterally extends to outward of the structure after processing. The higher energy increases the crack length until it touches the adjacent Aluminum line of another chain. Although the line touching isn't shown in this structure, it is probably located in one of these links of two chains since the resistance measuring results show that these two chains are short. Thus, the optimal energy of structure 1 is

decided to be 0.2 μJ, because it has the highest yield and no failure (chain short) occurs.

From figures 3.9 and 3.11, it seems that Structure 2 achieves highest yield and lowest resistance per link simultaneously at the same energy (0.25 μJ). Furthermore, its energy window curve follows its yield curve. This happens in structure 3 as well. As a result, it helps us to easily decide the optimal parameters such as energy for later mass production according to the criteria of choosing the lowest resistance/link and the highest chain yield energy based on a reasonable spot size. Our experiment shows the optimal energy for the structure 2 and 3 are 0.25 μJ and 0.22 μJ respectively. In the case of structure 4, energy 0.25 μJ, at which we obtained the perfect yield (no chain open and short), was selected as an optimal energy, although the average resistance is slightly higher than the minimum value.

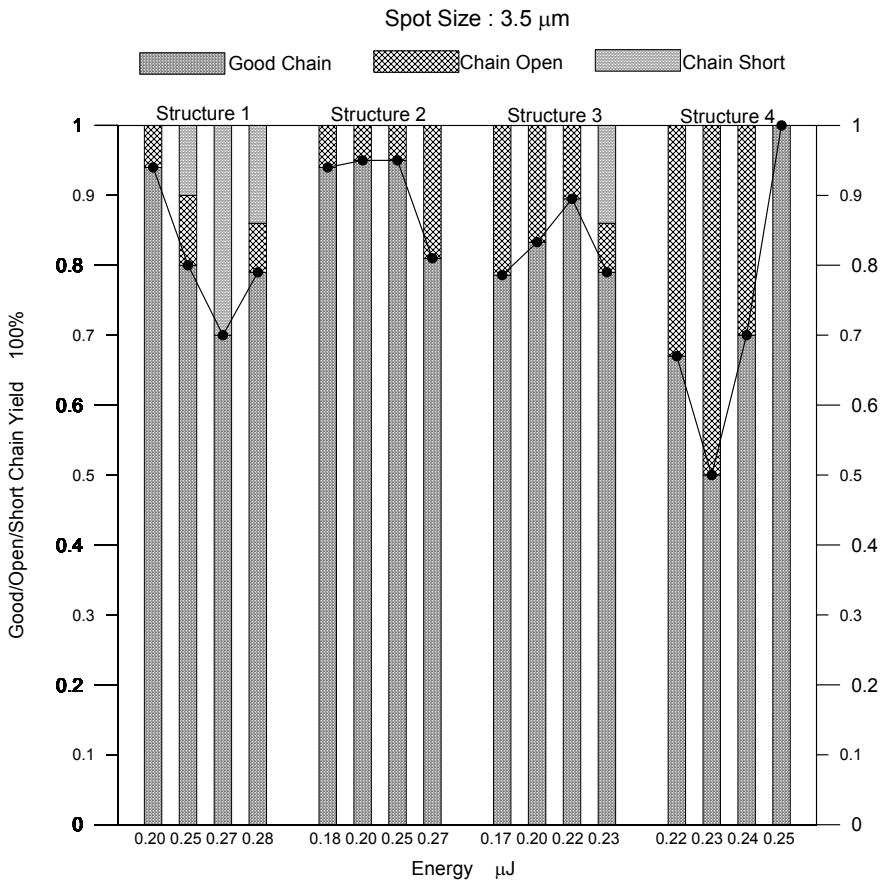

Fig. 3.11 Chain yield vs. energy window

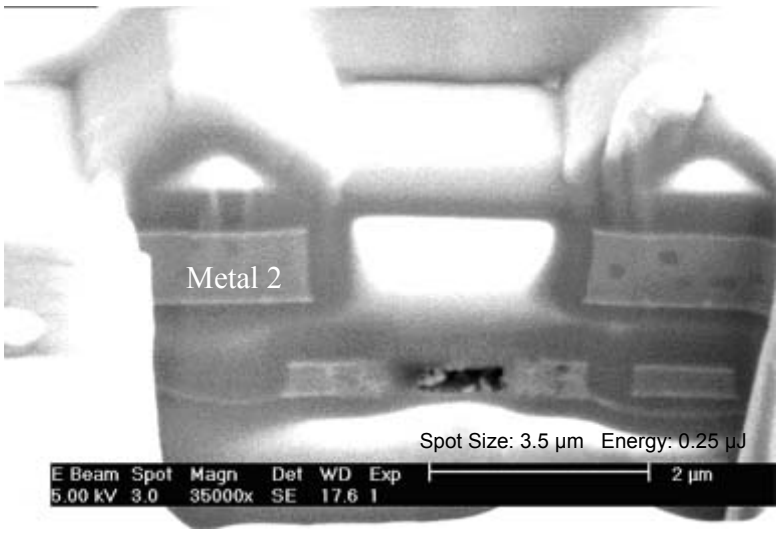

Fig. 3.12 A FIB picture of structure 1

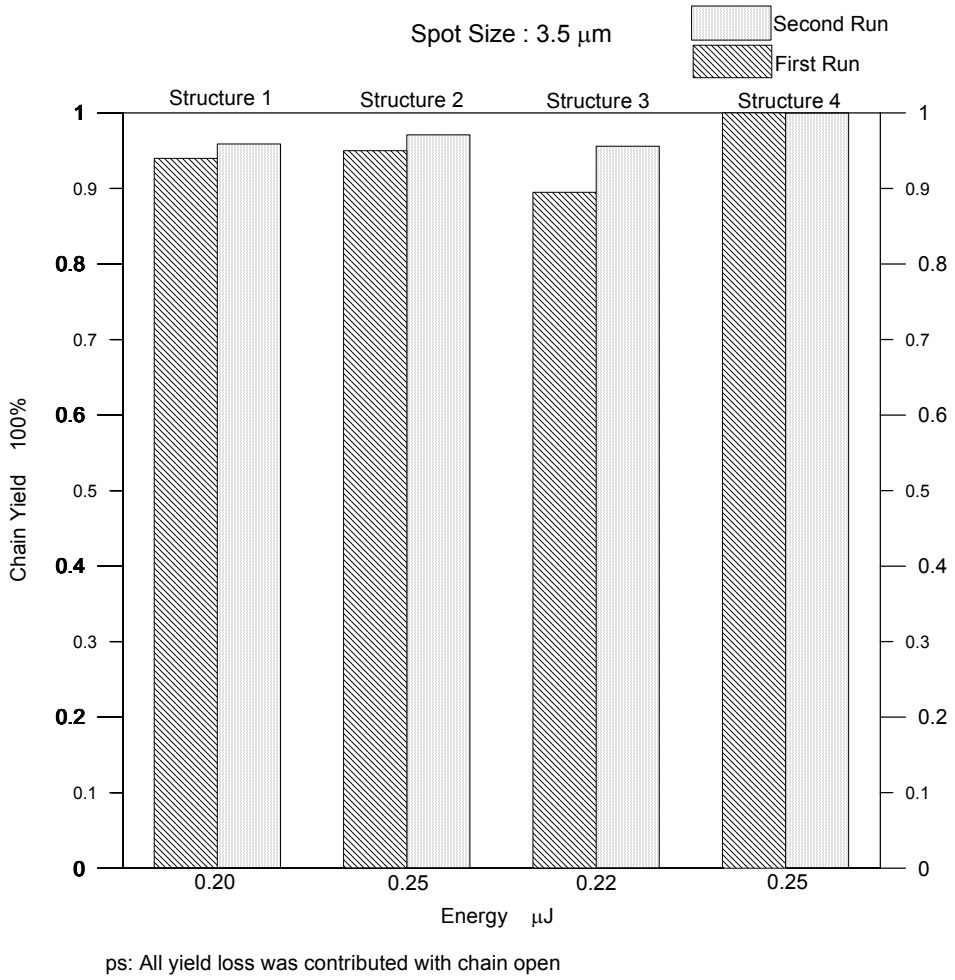

Fig. 3.13 Improved chain yield vs. energy

Fig. 3.13 shows the chain yield improvement by using the optimal energy to perform the laser processing for the rest chips on the test wafer in the second position run. Note that the chain yield of the second run, shown in the fig. 3.13, is calculated by combining the yield of the first run so that the actual yields of the second run is higher than that in the fig. 3.13.

Structure 4 maintains the perfect yield (100%) at these two position runs. Thus it is the best structure of those candidates, if we only consider the highest yield and low resistance per link as the criteria of choosing the optimal energy. However, structure 1, 2 and 3 present the yield improvement using their own optimal energy. Moreover, the structure 1 and 2 show higher yields than that of structure 3 to indicate that the two-line design is better than tree-line design.

3.6 Summary

The laser processing experiments verify the four different designs that they are able to form microbridges using different laser energies, and present the low resistance ranging from 1 Ω to 4 Ω. The optimal energy was found in each structure and the yield was improved by applied it. The experimental results also show the failure modes of each structure. Basically, the two-line design is better than the three-line design since the former presents lower resistance and higher yield. No structure is "perfectly selected" since no one presents the highest performance (the

lowest resistance), the highest productivity (the widest energy window), as well as the highest yield simultaneously, as shown in the table 3.2. However, structure 1 and 2 could be considered the optimal designs due to their low resistances, wide process windows, and high yields in processing.

	Resistance	**Energy Window**	**Yield**
Results	S1<S2<S3	S2>S1>S3	S2>S1>S3

Table 3.2 The comparisons of structure 1, 2, and 3 in laser processing

Chapter 4: Scalability Analysis

4.1 Introduction

To scale down size of the chip always gains the advantage of cost down in semiconductor industry. It is also the requirement for microbridges applying to next generation ICs. Thus, it is very significant to understand if these structures maintain their performance and productivity while their sizes are shrunken. The purpose of this chapter is to analyses the scalability of these structures. First of all, section 4.2 presents scalability experiments for these structures (pitch 1.8 μm). The experimental procedures and main criteria for these small dies are the same as the ones for large dies.

Section 4.3 shows the comparison of these structures at different scales, pitch 2.2 and 1.8 μm. In this section, the relative process window is introduced to evaluate the scalability. Moreover, a new parameter, minimum resistance and its variation, is created to estimate scalability as well. The last section 4.4 summarizes the results of scalability experiments and analysis.

4.2 Scalability Experiments

4.2.1 Process Window

The structure 3 failed in this scale, because it didn't have a wide enough process window (only one energy succeeded). The average resistance per link, shown in fig. 4.1, represents the similar trends as the case of pitch 2.2 μm ($R_{S2}>R_{S1}>R_{S4}$). But only structure 4 maintains the same type curve of the process window between these two scales. The process window curves of Structure 1 and 2 always monotonically decrease since the chain short happened before the lowest resistance was achieved. In addition, structure 4 generally shows large resistance variations within its process window than that of the structure 1 and 2. Thus, structure 4 requires more precise laser focus position when its size is scaled down.

4.2.2 Yield Analysis

Fig. 4.2 shows the chain yield of these structures versus their energy windows. It also represents the failure modes and their ratio with good chains. Structure 2 represents the best yields comparing to other

structures. Two energies, 0.15 μJ and 0.17 μJ, at which the highest yield and the lower link resistance are obtained, are picked up as an optimal parameter in the case of structure 1 and 2 respectively. It is noted that the energy 0.22 μJ is chosen for the structure 4 since it shows the less possibility of breaking passivation than the higher energy 0.24 μJ, although at 0.24 μJ the perfect yield 100% can be obtained.

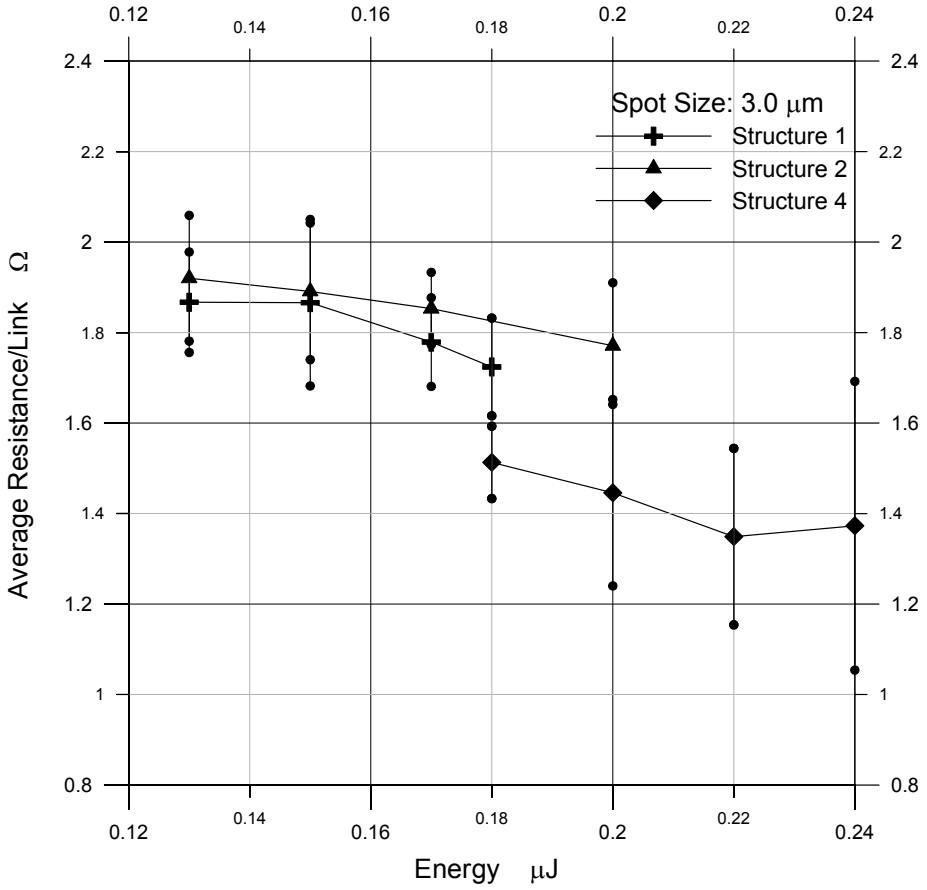

Fig. 4.1 Energy windows vs. average resistance per link (pitch 1.8 μm)

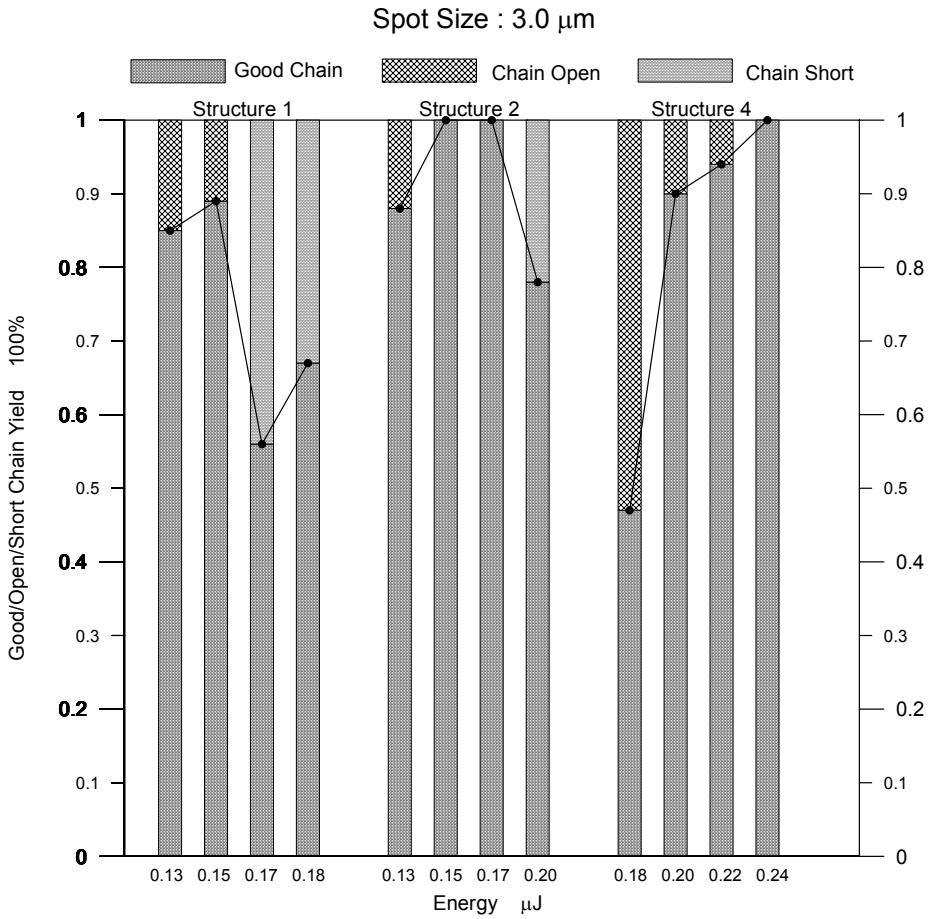

Fig. 4.2 Chain yields of these structures

Fig. 4.3 represents the chain yield improvement of these structures. Structure 2 maintains the highest yield 100% and other two structures represents the yield increase after performing the second run. The result may be confirmed in its FIB picture, shown in fig.4.4. The picture presents the possibility of forming double microbridges, vertical-link and lateral-

link, to increase the linking probability. From the point of yield analysis, structure 2 demonstrates a robust design as its size is scaled down. Therefore, structure 2 is shown to be the better design than those of other structures in the case of pitch 1.8 μm structures.

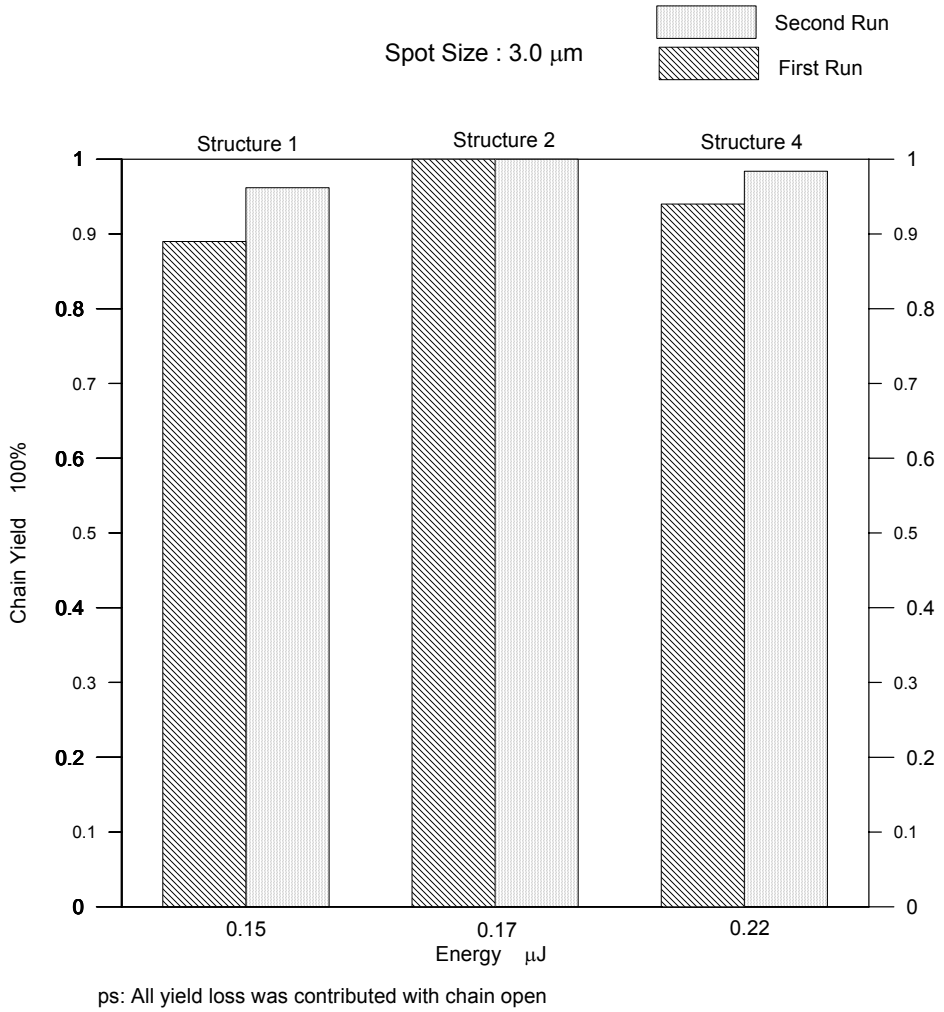

Fig. 4.3 Chain yield improvement of these structures

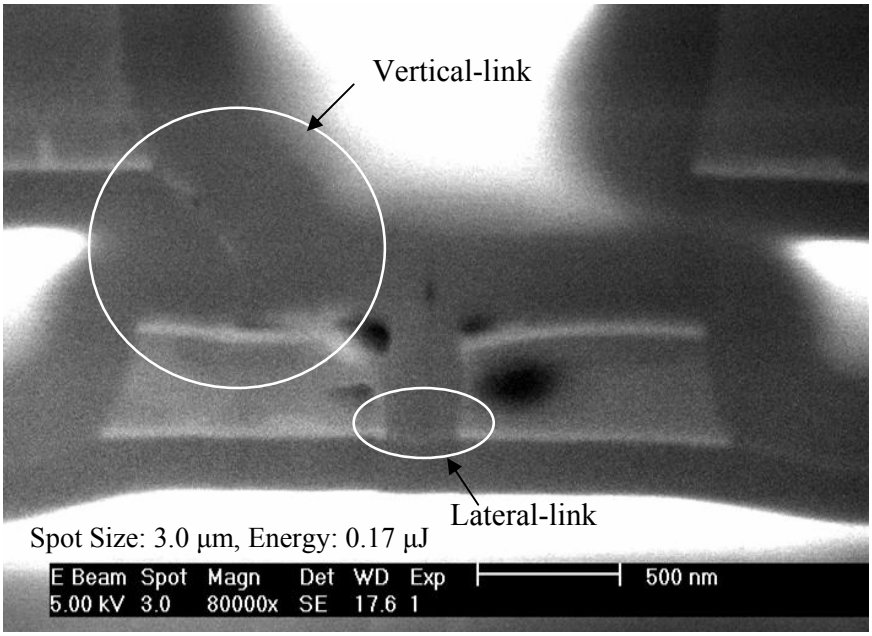

Fig. 4.4 A FIB picture of structure 2 (pitch 1.8 μm)

4.3 Scalability Analysis

4.3.1 Relative Process Window

In order to eliminate the dependence of absolute energy window on the characteristics of different structure sizes (scalability), the processing window is redefined as the ratio of the available energy range (E_h - E_l) to the average energy (E_a) as [25]

$$\text{Relative Process Window} = (E_h - E_l)/E_a \qquad 4\text{-}1$$

Where

E_h: the highest energy within the process window

E_l: the lowest energy within the process window

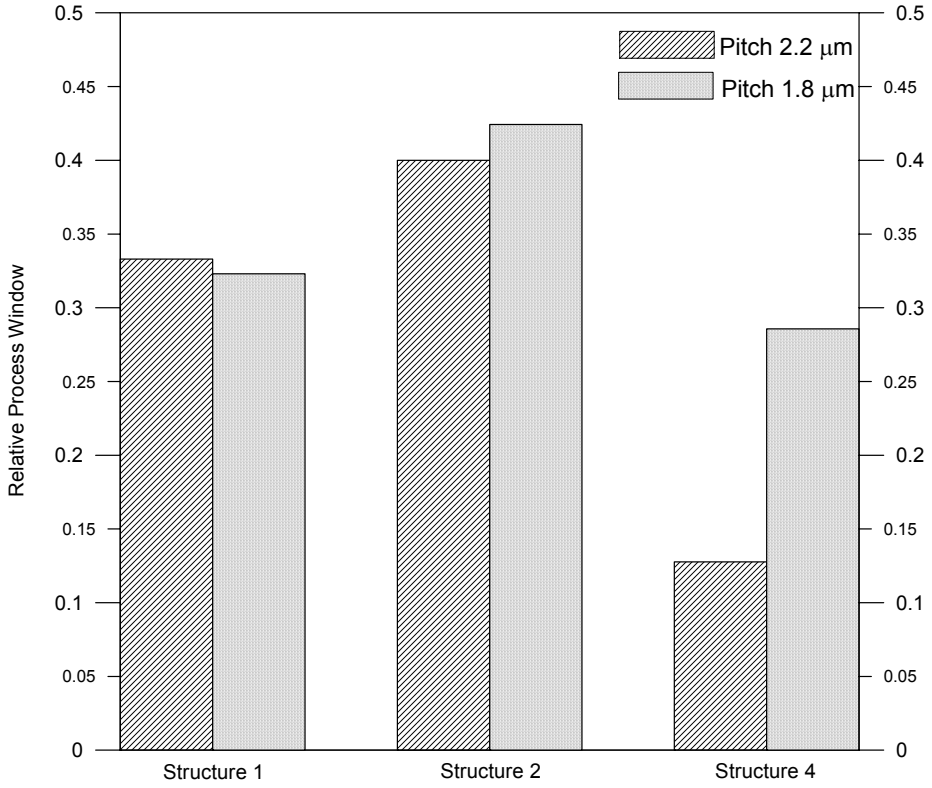

Fig. 4.5 Relative Energy window comparison of 1.8μm and 2.2μm pitch chips

Fig. 4.5 shows comparison of relative energy window of the 1.8μm and 2.2μm pitch chips. Structure 2 has the highest values of relative

process window, which shows it is able to form links over a broad energy range. The relative process window of structure 1 slightly decreases as link size shrinks but the relative process windows of structure 2 and 4 increases when their size scales down. The relative process window of structure 4 increases significantly (124%). This is because the design of the structure 4 is different from structure 2. The desired-lateral link of structure 4 is formed by metal 2 (top level) but the desirous-lateral link of structure 2 is formed by metal 1 (lower level metal). With high zapping energy within the process window, the failure mode of the structure 4 is passivation break due to its thin surface layer (passivation). The failure mode of passivation break in structure 4 is less sensitive to scalability. In other words, the highest energy within the process window for structure 4 doesn't reduce significantly, but the lowest acceptable energy decreases dramatically when scaling down. Thus, the process window of small scale is enlarged. Interestingly, this is an inverse result to the vertical link design, which has been proven in early work that the relative process window decreases as the structure is scaled down [25]. Therefore, a superior advanced-lateral

link design, structure 2, provides more compatible alternatives in chip scalability than that of the simple vertical link.

4.3.2 Minimum Resistance and Its Variation

A minimum resistance per link formed with laser energy within the process window is the best result for each structure. However, the link resistance changes as laser energy varies. Ideally we wish the resistance vs. energy curve be flat within laser energy window. Therefore the minimum resistance variation within the process window is given by the author and applies it as an alternative criterion to determine a better design when the structure size is scaled down. It yields

$$\sigma_{R_{\min}} = \sqrt{\frac{\sum_{i=1}^{n-1}(R_i - R_{\min})^2}{n-1}} \qquad 4\text{-}2$$

Where:

R_i is the measured resistance within the process window,

R_{min} is the minimum resistance within the process window, and

n is the number of the measured resistance within the process window.

Fig. 4.6 shows the minimum resistance and its variation for structure 1, 2 and 4 with different link sizes. Structure 4 has the lowest resistance and its variation doesn't change when the size scales down. Structure 2 shows the minimum resistance and its variation decrease simultaneously when the link size shrinks, although it has the highest value of minimum resistance in these structures. These results show that structure 4 is an ideal design for the high-speed applications because of its low resistance, and structure 2 is a better design of considering scalability of the chip.

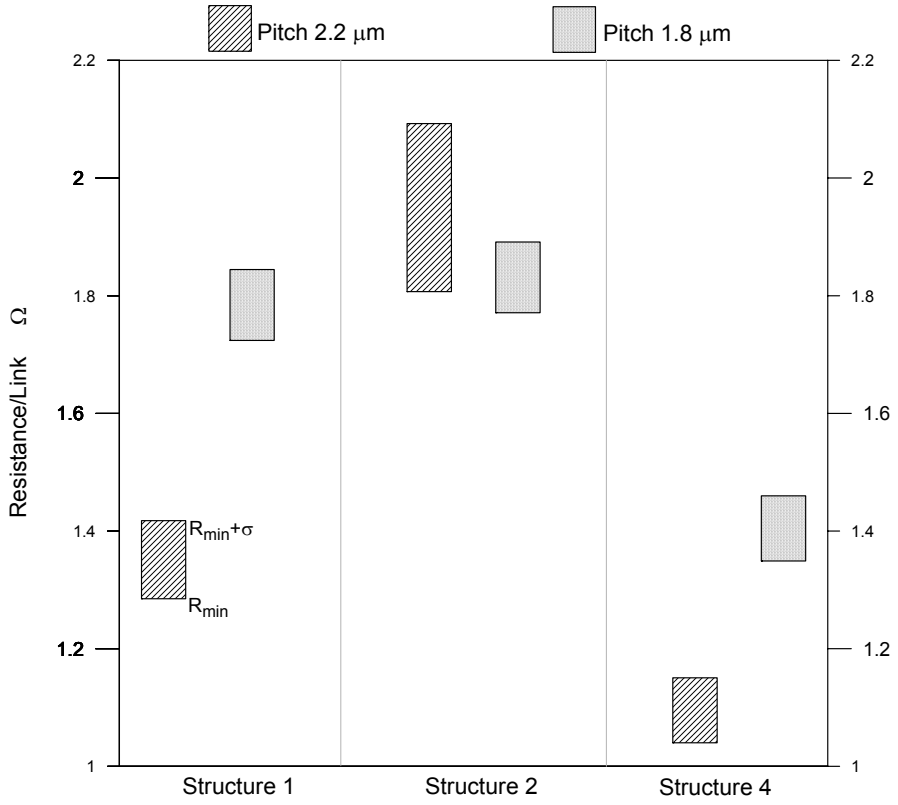

Fig. 4.6 The minimum resistances and their variations

4.4 Summary

The laser processing experiments verify the three different designs that they are able to form microbridges using different laser energies while their sizes are scaled down. Although they present narrower process windows, they provide the designer their lower resistance in terms of higher performance and lower power consumption. The optimal energy was found in each structure and the yield was improved by applied it. The experimental results also show the

same failure modes with the large ones. According to the results of scalability experiments and parameter analysis, structure 2 is undoubtedly better design to satisfy next generation ICs' requirement when the devices get smaller and circuit layout gets denser. Additionally, if the new lateral-link design can be applied, structure 4 is preferred for high-speed circuit applications due to its lowest resistance in these structures, though the laser parameters are not as robust.

Chapter 5: Reliability Test

5.1 Introduction

The reliability assessment of these microbridges is relied on Zhang and Bernstein's study in vertical linking structures [26]. Zhang indicates that the voids inherently exist at the aluminum lines and the arms of the links after processing to increase the failure rate of electromigration. In this chapter, section 5.2 presents the concepts of electromigration effect, which primary occurs in interconnects of the microelectronic devices with high current flux.

Section 5.3 describes accelerated stress tests and parameter n and E_A calculations due to Black's equation and JEDEC standards [27][28]. Section 5.4 presents Arrhenius life-temperature relationship to estimate median time to failure (t_{50}) of structure1, 2 and 4 in two conditions, corresponding to temperatures of the device in storage and operating environment. Details of experiments are shown in section 5.5. Section 5.6 covers the results and discussion of the reliability tests for these structures, and they are summarized in the section 5.7.

5.2 Electromigration Effect

Electromigration is a metallization-related phenomenon to reveal the mass transport in metal due to the momentum transfer between conducting electrons and diffusing metal atoms when it is stressed at high current densities. According to the observation by Black [29], electromigration had been recognized as the cause of two distinct wear-out failure modes for silicon device depositing aluminum as metallization materials at its upper-level layers.

One of the failure modes called “open circuit” is of void formation by the condensation of vacancies in the aluminum conductor. The second named “short circuits” is the growth of etch pits into silicon, at ohmic contacts where electrons leave the silicon and aluminum, by the solid-state dissolution of silicon into aluminum and the carry of the solute ions down the aluminum conductor away from the silicon-aluminum interface. The process continues until an etch pit develops into the silicon to a depth ample to short out an adjacent junction or conductor.

Electromigration was discovered more than one hundred years ago [30], and has been studied for several decades in both molten and solid bulk metals

[27]. Although electromigration essentially exists whenever current flows through a metal conductor, the requirement for electromigration to be a severe problem did not become of great reliability concern until the first commercial IC was made in 1966. In the early research of a bulk metal wire such as those used for home circuitry, the peak current density is to probably be 10,000 A/cm^2 due to joule heating. Any current density even not going beyond this value will generate enough heat to melt the wire. Nevertheless, the driving force from electrons colliding into diffusing metal atoms would be insufficient to make electromigration a meaningful issue. For several decades electromigration was only an interesting problem in solid-state physics until 1970s. Since then, the metal line of ICs allowed current densities of nearly 10^6 A/cm^2 with minimal joule heating. And most conductors of ICs were made of pure aluminum or tiny amount of copper alloyed (Al 99.5%, Cu 0.5%), the material with a low resistance and melting temperature implying fast diffusion at low temperature. This combination of high current density and fast diffusion at low temperature in thin film metal lines of ICs propels electromigration to become a significant reliability problem. Until now, even

copper is gradually instead of aluminum to be the new conductor materials due to the request of more condense circuit development. Electromigration is still of great concern, especially for the reliability assessment of ultra large scale integrated (ULSI) microelectronics.

5.3 Accelerated Stress Test

The objective of the accelerated stress test is to reduce the length of the test period by accelerating failures at more strict circumstance. For thin-film metal interconnect test structures, the accelerated stress tests were performed to assess the eletromigration effects of these structures at the environment of both high temperatures and current densities, and to extrapolate the results to use conditions.

In this work, the failure times of these structures are assumed to follow lognormal distributions since it is widely applied for life data, including metal and solid state components used in semiconductor industry [31]. According to the Black's equation,

$$t_{50} = \frac{A}{J^n} \times exp\left(\frac{E_A}{k_B T}\right) \quad \text{5-1}$$

Where:

J is current density (A/cm^2),

n is model parameter for current density,

E_A is model parameter for temperature, i.e. activation energy (eV),

T is Temperature (K),

k_B is Boltzmann's constant (8.617*10^{-5} eV/K), and

A isconstant.

The estimation of n or E_A is obtained from a linear regression for one independent variable. It will be presented in the following sections. However, when both current density and temperature are varied, the estimation of n and E_A are obtained from a multiple linear regression for two independent variables [28].

5.3.1 *n* Calculation

If the current density is varied while the stress temperature is maintained constant in these electromigration stress tests, then t_{50} will be proportional to $1/J^n$, and hence

$$\ln t_{50} = -n \ln J + B \qquad 5\text{-}2$$

Where B is a constant involving A and E_A. Assuming the $\ln t_{50}$ and $\ln J$ are linearly dependent so that the $-n$ is the slope if plotting $\ln t_{50}$ and $\ln J$ data pairs.

5.3.2 E_A Calculation

If the temperature of the test is changed while the current density stress is maintained constant in the electromigration stress tests, t_{50} will be proportional to $\exp(E_A/k_BT)$ and hence,

$$\ln t_{50} = \frac{E_A}{k_B} \times \frac{1}{T} + C \qquad 5\text{-}3$$

where C is a constant involving A and n. Similarly, the E_A/k_B is the slope if plotting lnt_{50} and $1/T$ data pairs based on the assumption of lnt_{50} and $1/T$ linearly dependent.

5.4 Arrhenius Life-Temperature Relationship

The Arrhenius life relationship is widely applied to the situation while failures are accelerated primarily as a result of an increase in temperature [31]. It yields

$$R_A = A_1 \times exp\left(\frac{-E_A}{k_B T}\right) \qquad 5\text{-}4$$

Where:

R_A is the reaction or process rate,

E_A is model parameter for temperature, i.e. activation energy (eV),

T: is temperature (K),

k_B is Boltzmann's constant ($8.617*10^{-5}$ eV/K), and

A_1 is constant.

For solid-state thin metal film, the reaction rate is equivalent with the rate of metal diffusion. The structure is assumed to fail when some critical amount of metal has diffused (eletromigration effect); recalling the equation 5-4, and it yields

$$t_f = A_1 \times exp\left(\frac{-E_A}{k_B T}\right) \qquad 5\text{-}5$$

Where t_f is the nominal time to failure. The Arrhenius acceleration factor between life t_{f1} at temperature T_1 and life t_{f2} at temperature T_2 yields

$$K_A = \frac{t_{f1}}{t_{f2}} = exp\left\{\left(\frac{E_A}{k_B}\right)\left[\left(\frac{1}{T_1}\right) - \left(\frac{1}{T_2}\right)\right]\right\} \qquad 5\text{-}6$$

The Arrhenius accelerated factor K_A and activation energy E_A can be obtained by performing the accelerated tests at higher temperatures. And thus the lifetime of the test structure in use condition is given by

$$t_f^{use} = t_f^{accele.} \times exp\left\{\left(\frac{E_A}{k_B}\right)\left[\left(\frac{1}{T_{use}}\right)-\left(\frac{1}{T_{accele.}}\right)\right]\right\} \quad 5\text{-}7$$

Equation 5-7 can be plotted using log t_f and 1/T as two axis variables. The slope of the two variables is E_A/k_B. A curve fitting is performed using linear regression to obtain the function of the curve. Then lifetime of the structure at use condition can be estimated using the curve function.

5.5 Experimental Setup

The test system used to perform Electromigration tests is SIENNA ITS8000, shown in the fig. 5.1, involving test modules, a pc-based computer, and three programmable temperature ovens.

In order to ensure the failure modes only caused by the microbridges, the test chips were packaged to be the type 20- pin-PDIP (Plastic Dual In-line Package). The Dual-In-line packages have been an industry standard for a long time. The applications are common in consumer products, automotive devices, memory, analog ICs, and microcontrollers. These packages have evolved into a state-of-the-art technology due to their robust reliability and great

improvement on performance. Additionally, the extended pins were carefully welded by the high temperature solders, whose physical properties are durable and stable even in the environment of 350 ^{o}C. As the results, the failure modes for microbridges are assumed not to relate to the packages and solder joints. Therefore, the package-level accelerated tests in this work are able to estimate the reliability of microbridges. There are 2016 series links simultaneously operating in an IC.

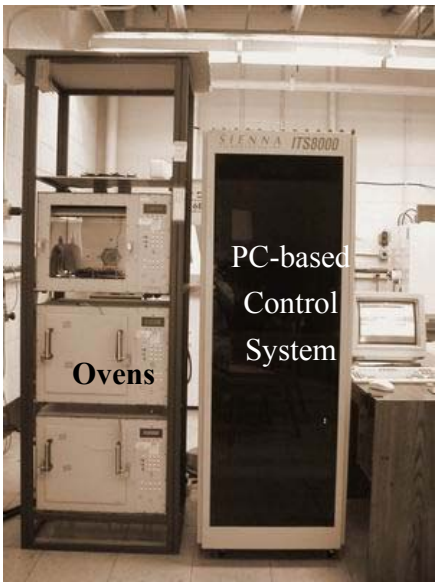

Fig. 5.1Electromigration test system

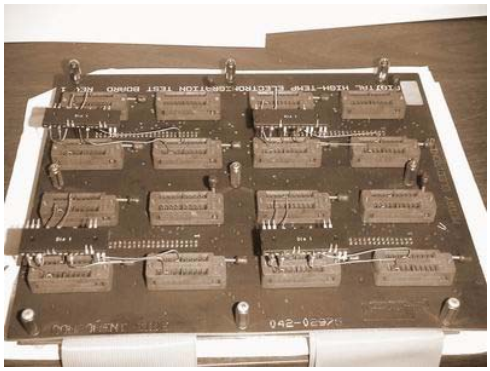

Fig. 5.2 Test boards and packages

The packages were plugged into the test board, shown in the fig. 5.2. Note that the structure 3 was disqualified in reliability tests since its performance (resistance/link) and scalability are much worse than that of structure1, 2 and 4. The test parameters setup is illustrated in the table 5.1.

Test Structure	Structure 1, 2, and 4
Temperature	150°C (423 K), 200°C (473 K), and 250 °C (523 K)
Current density	$5.44*10^5$ A/cm^2 (all temperatures), $3.26*10^5$ A/cm^2 (200 °C)
Failure Criteria	Resistance per link increasing rate great than 10 %

Table 5.1 Parameters setup

5.6 Results and Discussion

Fig. 5.3 (a) and (b) shows the cumulative distribution function F(t) of structure 1 at different temperatures and current densities respectively. There is not obviously dissimilarity with the standard deviations for various temperatures and current densities to indicate that only a specific failure mechanism occurs at all conditions. The similar situation can be found in structure 2 and structure 4, as shown in fig. 5.4 and fig. 5.5 respectively. The failure data and median times to failure of all conditions are shown in Annex A

as input data of calculating parameters n and E_A. Comparing to the data of t_{50}, the structure 4 has the largest values in 473 K and 423 K to imply that it may have a longer lifetime in the environment when the structure is in storage and operating status.

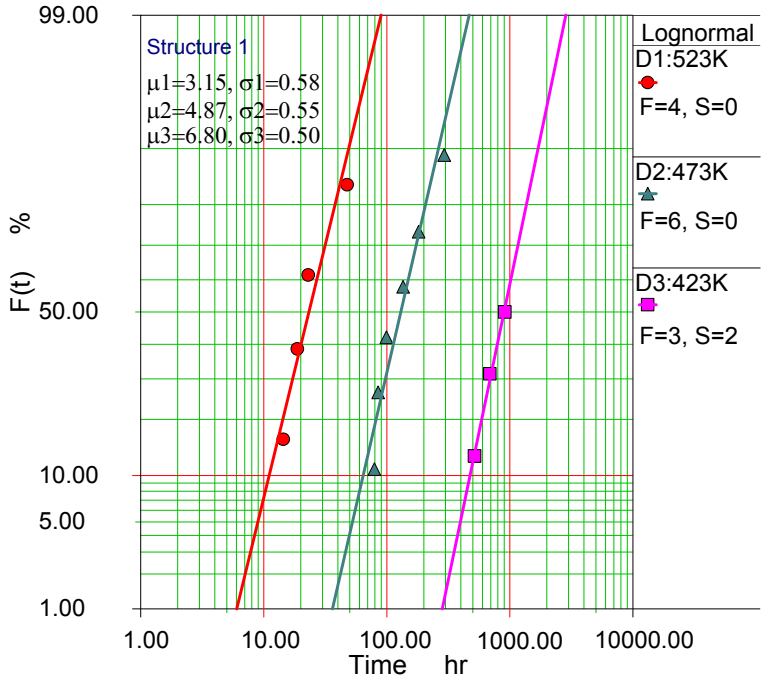

(a). Various temperatures

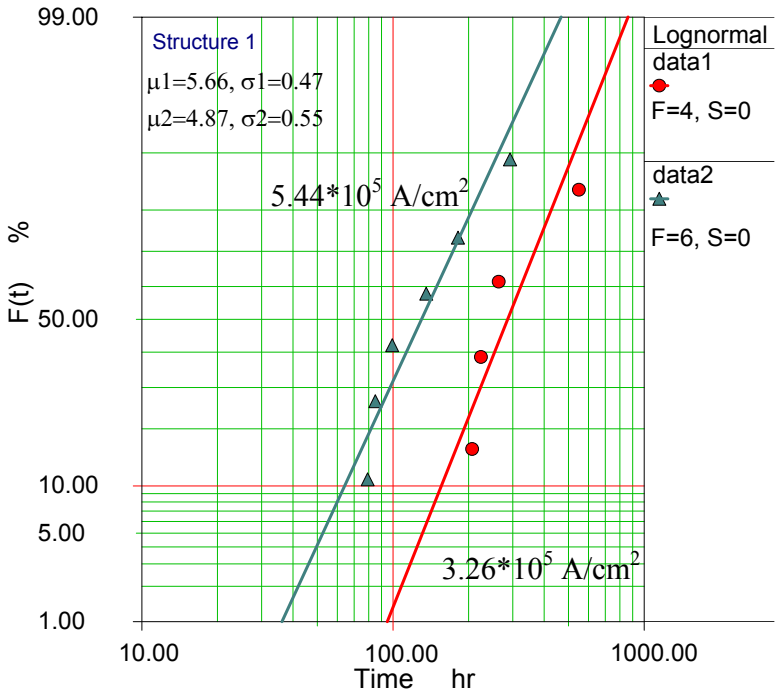

(b) Various current densities

Fig. 5.3 Cumulative distribution function, F(t) of structure 1

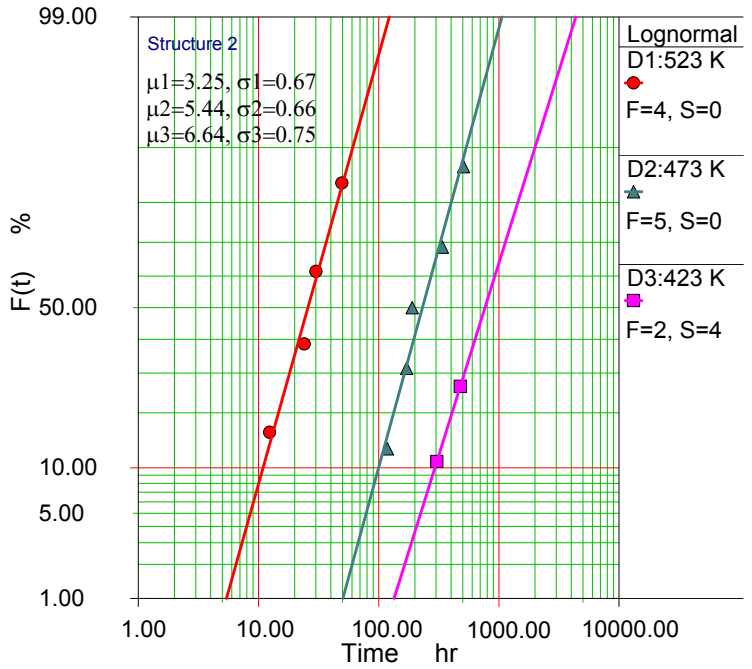

(a) Various temperatures

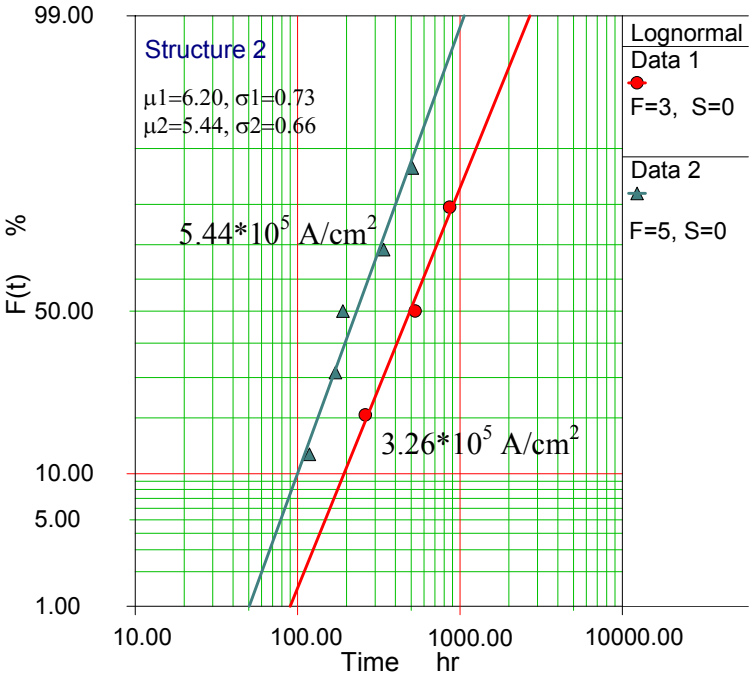

(b) Various current densities

Fig. 5.4 Cumulative distribution function, F(t) of structure 2

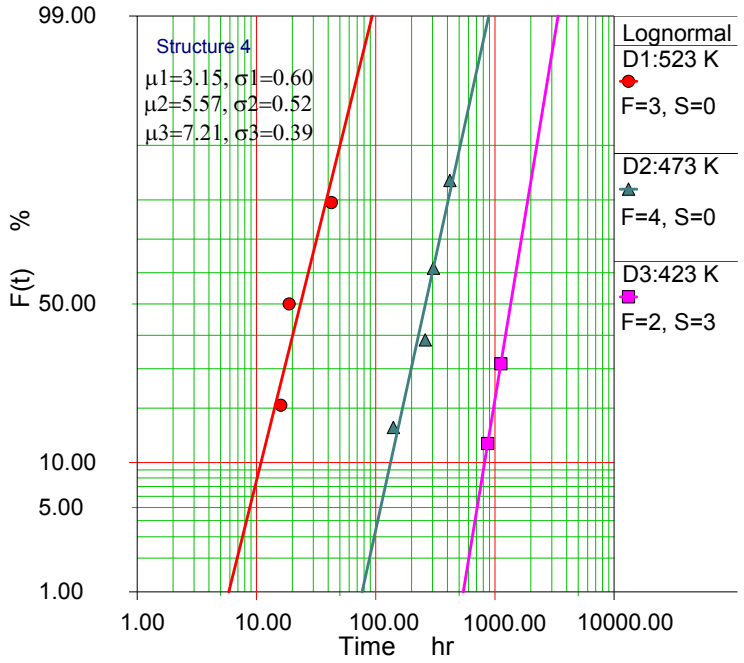

(a) Various temperatures

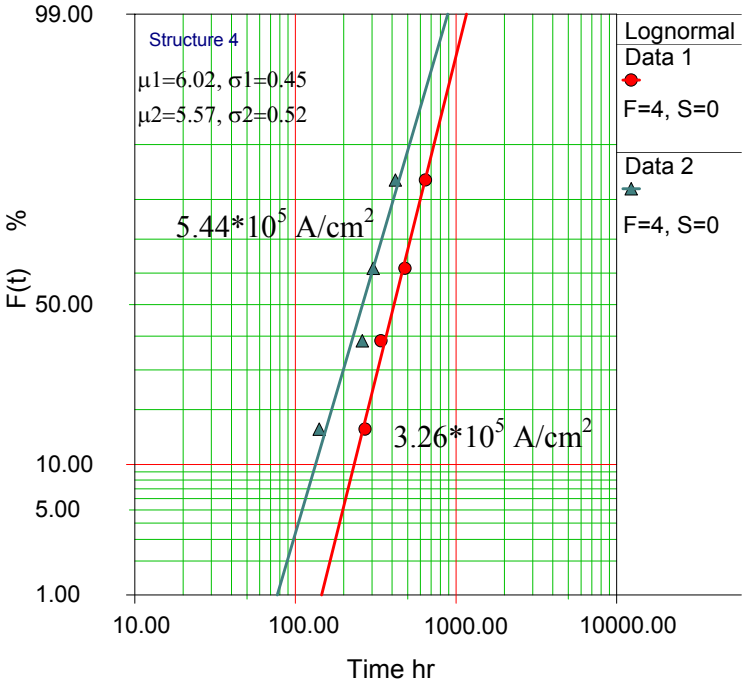

b) Various current densities

Fig. 5.5 Cumulative distribution function, F(t) of structure 4

	Structure 1	Structure 2	Structure 4
n	1.52	1.46	0.87
Confidence Coefficient 1-α	0.8	0.8	0.8
E_A (eV/K)	0.696 ± 0.074	0.622 ± 0.463	0.748 ± 0.412
Median Time to Failure at storage temp. 298 K (years)	321.7	166.4	1254.2
Median Time to Failure at working temp. 338 K (years)	12.8	9.2	36.7

Table 5.2 The results of the electromigration tests

Table 5.2 presents the results of calculations. The input data and details of the calculations are shown in appendix B and C respectively. The two-sided confidence intervals with the confidence of coefficient 80% are applied to the calculation of activation energy (E_A) for all structures, but they are not available to the estimation of n due to the limitation of experiment samples (only two current densities were done). The storage and working temperatures of these structures are assumed to be 298 K (25 ^{o}C) and 338 K (65 ^{o}C) referred to the general design rules of microelectronic device, 20-30 ^{o}C as well as 55-75 ^{o}C.

Structure 1 and 2 present the similar n values. But the n value of the structure 4 is apparently lower than that of the other two structures. This means the metal diffusion by increasing current density doesn't obviously occur in structure 4. This is because the difference of the microbridge shape regarding with the structure design. The similar structure design of structure 1 and 2 results in the similar link appearances with the slender interconnect, as shown in fig. 5.6. Oppositely, structure 4 presents different bulk interconnect regarding with its large metal design, as shown in fig. 5.7. The same results can be found in the Jone's study for aluminum electromigration [32]. Jone indicates that the diffusion effect would be dominated by surface and grain-boundary, which are subjected to the structural design and processing differences of the test lines while the temperature is lower than 275 ^{o}C. Further note, we predict that lifetimes of structure 1 and 2 will be limited by the large current gradient in the sheet-type microbridge according to the Zhang and Bernstein's simulation results [26] for their link structures.

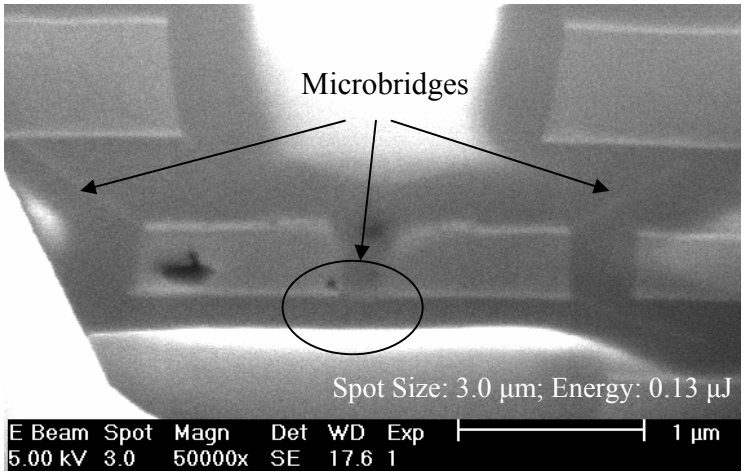

Fig. 5.6 The shape of microbridge in Structure 1 (FIB)

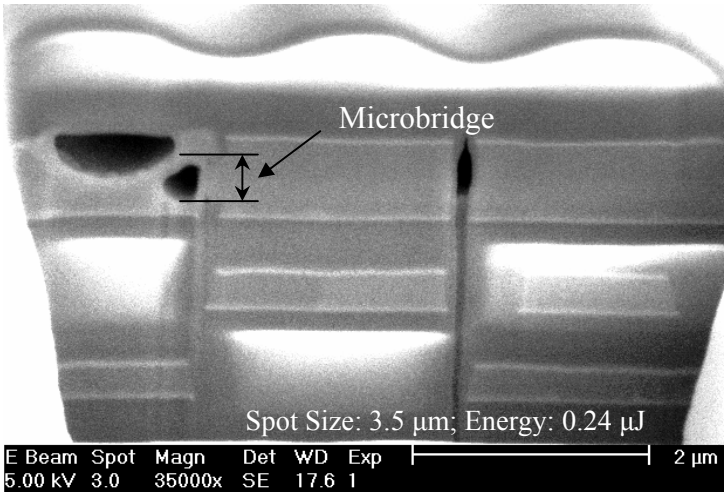

Fig. 5.7 The shape of microbridge in Structure 4 (FIB)

In Buerke's study [33], the activation energy values can be found between 0.5 and 0.9 eV for different aluminum interconnect-design and production. In our work, the activation energies of these test structures were obtained between 0.6 – 0.8 eV within Buerke's estimation. The variances of E_A of the structure 2

and 4 are large. This is because only fewer samples can be obtained in the pilot run. This situation frequently occurs in the period of new product development. It can be improved at the later mass production.

Fig 5.8 (a), (b), and (c) shows Arrhenius diagrams of structure 1, 2 and 4. The lifetimes of structure 1 and 2 at operating temperature are 12.8 and 9.2 years respectively. That is reasonable for the cycle time of ICs using in the market. Structure 4 presents premium lifetimes at operating and storage conditions. It is form 3 to 4 times lifetimes of the structure 1 and 2 at operating temperature, and from 4 to 8 times at storage temperature. The result demonstrates the previous prediction from current gradient point of view. The structure 1 and 2 present the large geometric change (thickness) between aluminum lines and the microbridge, where the large current gradient is found to lead elctromigration effect easily. Further note, the slim sheet-type microbridge has less grain boundary to scatter the current flux resulting in void formation in there. In a word, the reliability test shows that structure 4 has a better lifetime with its robust arm of microbridge. However, the lifetimes of

structure 1 and 2 satisfy with the minimum lifetime requirement of integrated circuits operated in the market.

5.7 Summary

The results of electromigration tests show that the lifetimes of these structures are reasonable for the cycle time of semiconductor device using in the market. Structure 1 possesses better lifetimes at operating and storage conditions than those of structure 2. Additionally, the sample lateral-design, structure 4, shows its premium lifetimes due to its strong arm of microbridge to resist the degradation.

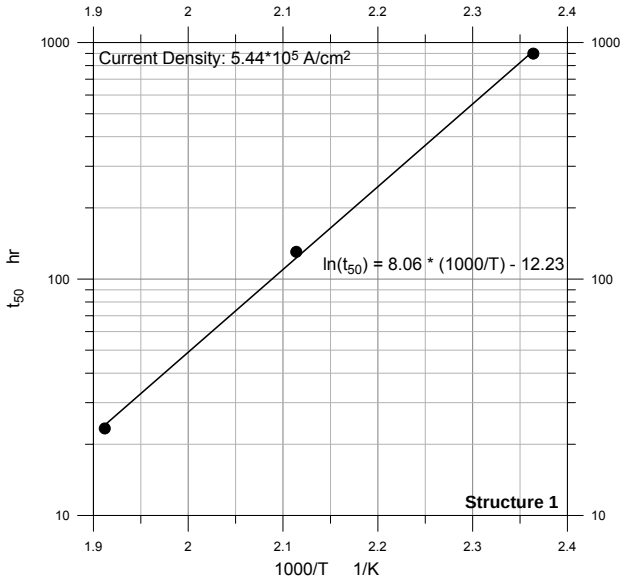

(a) structure 1

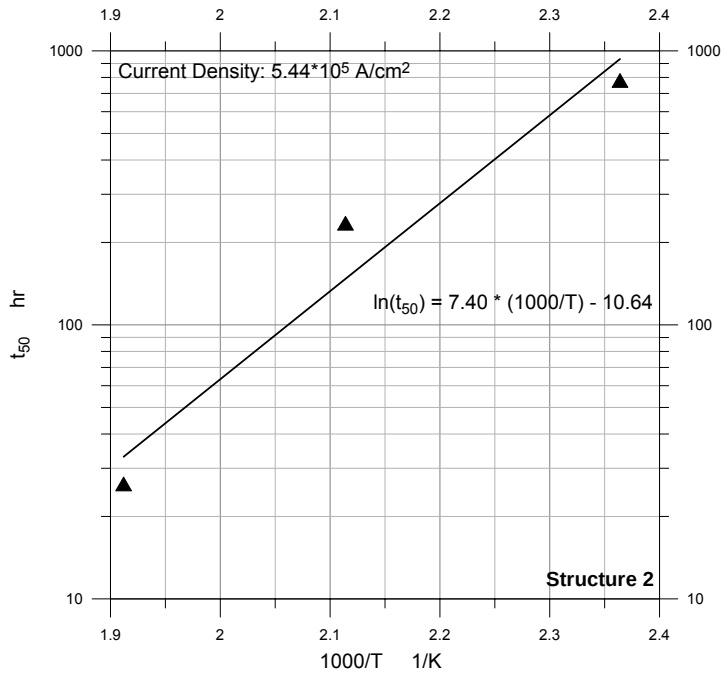

(b) structure 2

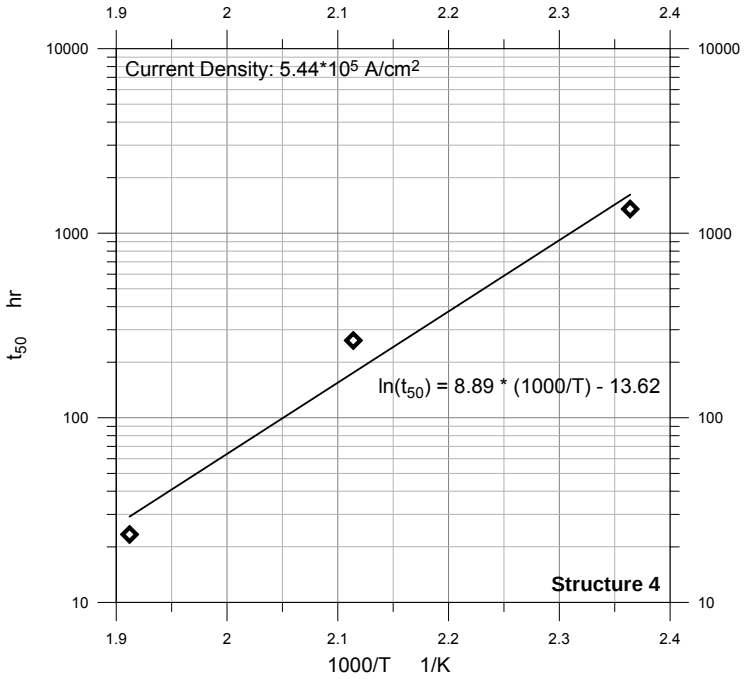

(c) structure 4

Fig. 5.8 The Arrhenius diagrams of structure 1, 2 and 4

Chapter 6: Finite Element Analysis

6.1 Introduction

This chapter presents the finite element method to simulate the process of forming microbridge. The first section simply illustrates the concepts of the finite element analysis and how does it apply to this work. It also presents the material properties using in this work and displays the element models for all structures.

The second part of the chapter shows the thermal analysis in these models. How to apply laser intensity function being the heat flux of the two-dimensional heat conduction equations? And then solve the equations based on some assumptions including boundary and initial conditions. The results for all structure in this work present the similar temperature field so that we only show one of the cases (structure 2) in this chapter.

The third section presents the structural analysis to obtain the stress and strain field in the model. The failure criteria are well defined and the crack analysis is performed in order to obtain the performance of the process, laser

energy window. The last section is the comparison of the energy windows between the experiments and simulation.

6.2 Finite Element Modeling

As mentioned in the chapter 2, it exists difficulty to obtain closed-form solutions such as temperature distribution, thermal stress, and cracking situations in this complex problem. A numerical method is used to obtain approximate solution. To simulate microbridge formation, the finite element method (FEM) is applied in this work since it is able to find the solution of this complicated problem by replacing it by a simpler one. Moreover, it is possible to improve or refine the approximate solution by spending more computational effort [15].

Using the finite element method, the solution region is divided into an assembly of many small, interconnected subregions called finite elements. In this work, a general-purpose finite element software code, called ANSYS®, is applied to solve the thermomechanical and fracture coupled problem by following steps:

Step 1: Generate the geometric model.

Step 2: Solve the nonlinear and non-homogeneous second order partial differential equation with a non-uniformed pulse laser heat source mentioned in the section 2.2 of the chapter 2 in order to obtain the transient temperature field.

Step 3: Solve the thermoelastic stress-strain-displacement equations mentioned in the section 2.3 of the chapter 2, using the result generated by step 1 as a thermal loading to obtain the thermal stress and strain field, especially the maximum principal stress at the pre-crack region.

Step 4: Perform crack analysis mentioned in the section 2.4 of the chapter 2 to obtain stress intensity factor at the tip of pre-crack.

Step 5: Repeat step 2 to step 4 by gradually increasing the hest source (laser energies) to find the threshold and maximum energies due to the criteria.

6.2.1 Model Generation

As shown in Fig.6.1, dense mesh FEM plane models are generated around the target of laser processing for structure 1, 2, 3, and 4 respectively. Because of the geometric symmetry, only a half of these structures are generated, with the side **AB** being the symmetry axis. The dimensions of the aluminum lines and the pitch between them are the same as the samples for experiments. Moreover, a focus point is considered in each corner of the aluminum line for possible crack analysis. At least 2400 quadrialateral elements for structure 1, 2, 3 and 4000 quadrialateral ones for structure 4 are applied in all calculations. Mesh tests are conducted by increasing the number of elements until the calculation result is independent of mesh density and all reported calculations represent convergent results. All materials are characterized as an isotropical elastic-plastic solid, and their properties for this work are shown in the table 6.1

		Property	Value	Reference
Al	**Thermal Analysis**	Thermal conductivity (W/mK)	$83+2.56*10^4/T$ T: temperature	[12]
		Specific heat (J/kgK)	938	[38]
		Mass density (kg/m^3)	2,700	[38]
		Melting Point (K)	923	[37]
	Structural Analysis	Young's modules (GPa)	70	[34]
		Poisson ratio	0.33	[34]
		Thermal expansion Coefficient (1/K)	$23*10^{-6}$	[34]
SiO_2	**Thermal Analysis**	Thermal conductivity (W/mK)	1.4	[35]
		Specific heat (J/kgK)	1,000	[35]
		Mass density (kg/m^3)	2,200	[36]
		Melting Point (K)	1973	[37]
	Structural Analysis	Young's modules (GPa)	72	[34]
		Poisson ratio	0.16	[34]
		Thermal expansion Coefficient (1/K)	$0.75*10^{-6}$	[34]
		Yield Strength (GPa)	8.4	[37]

Table 6.1 The properties of the Materials

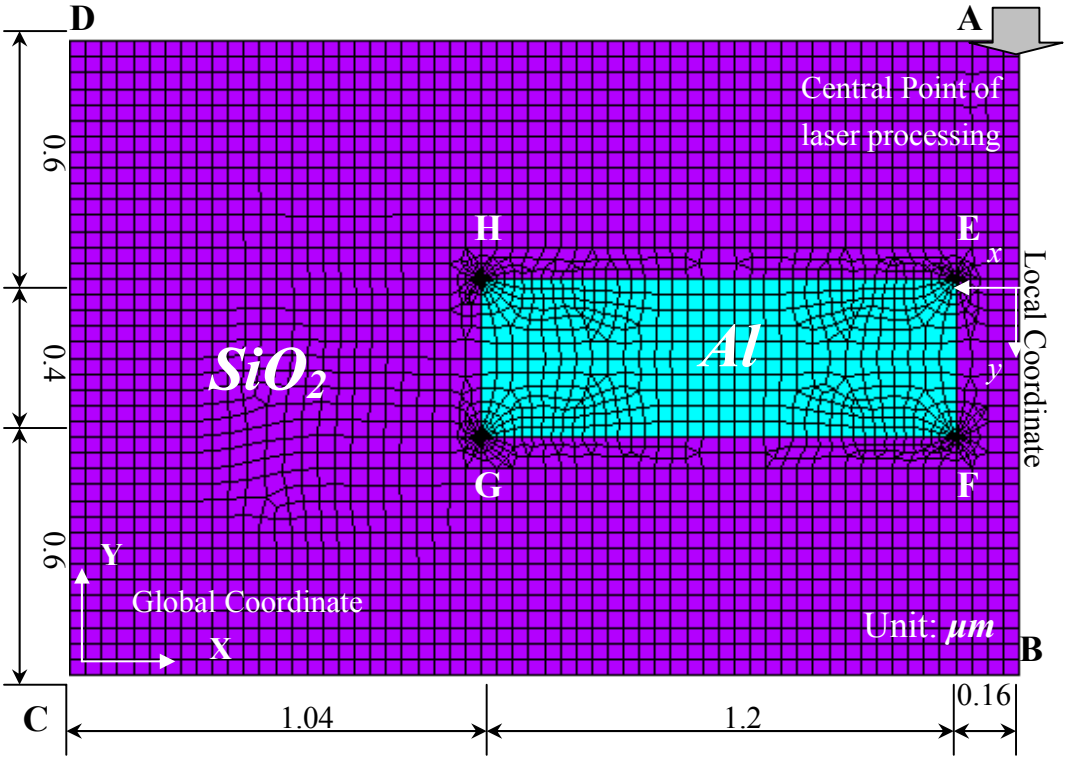

(a) Structure 1

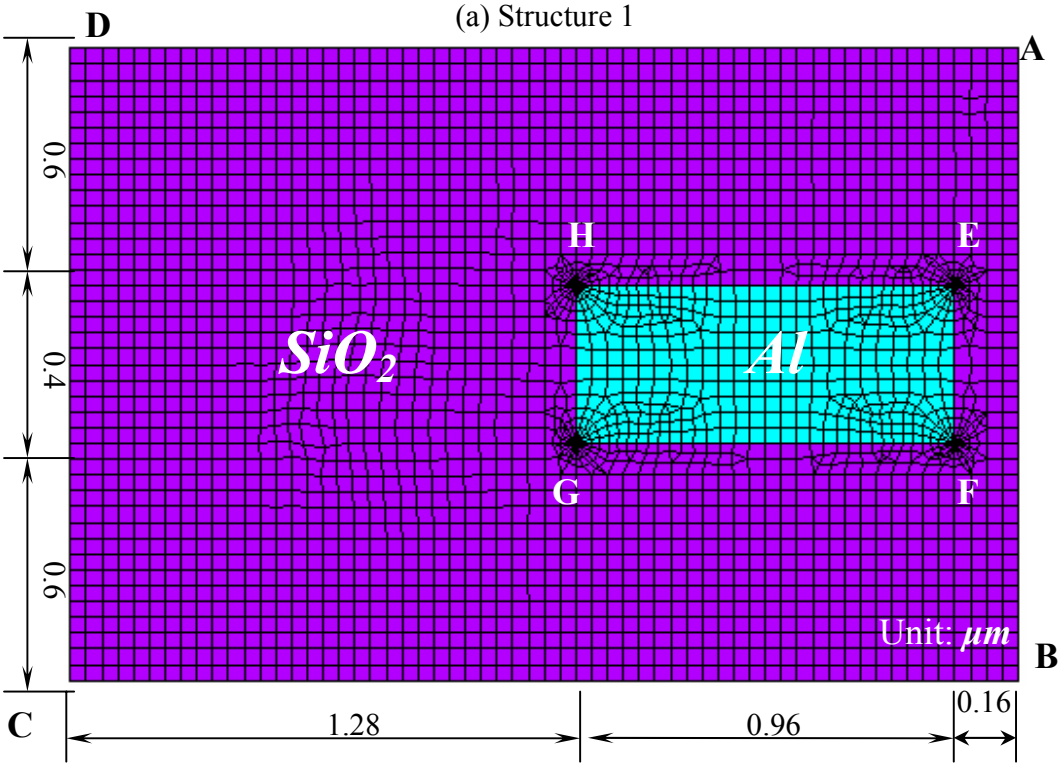

(b) Structure 2

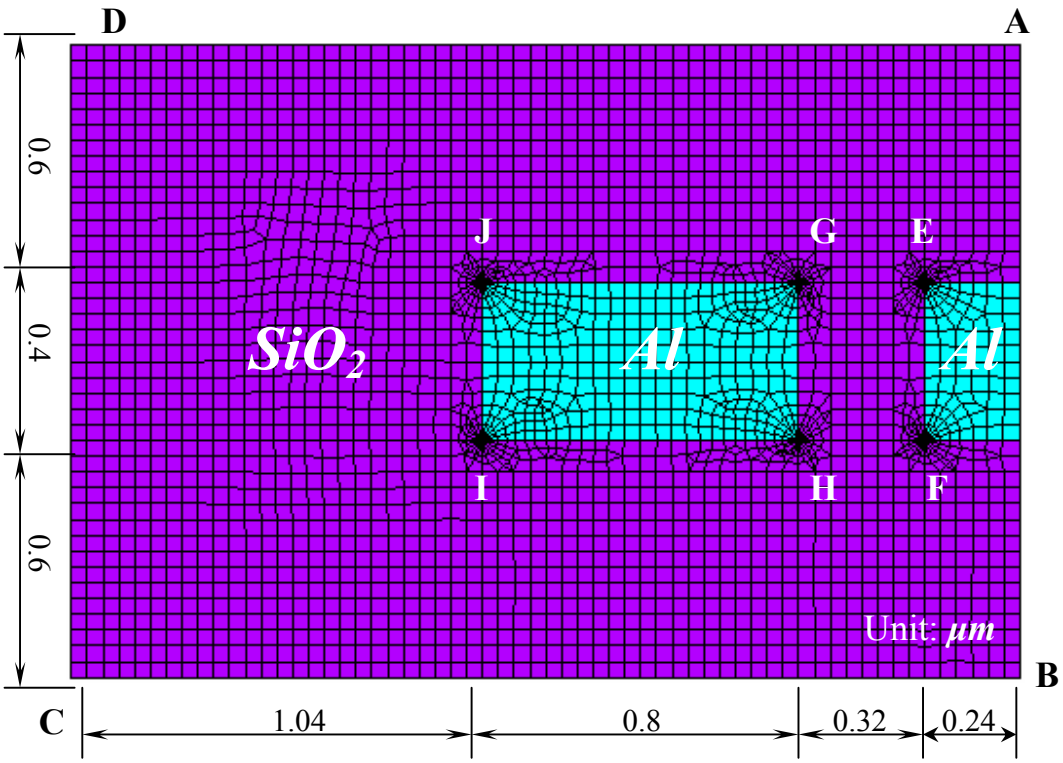

(c) Structure 3

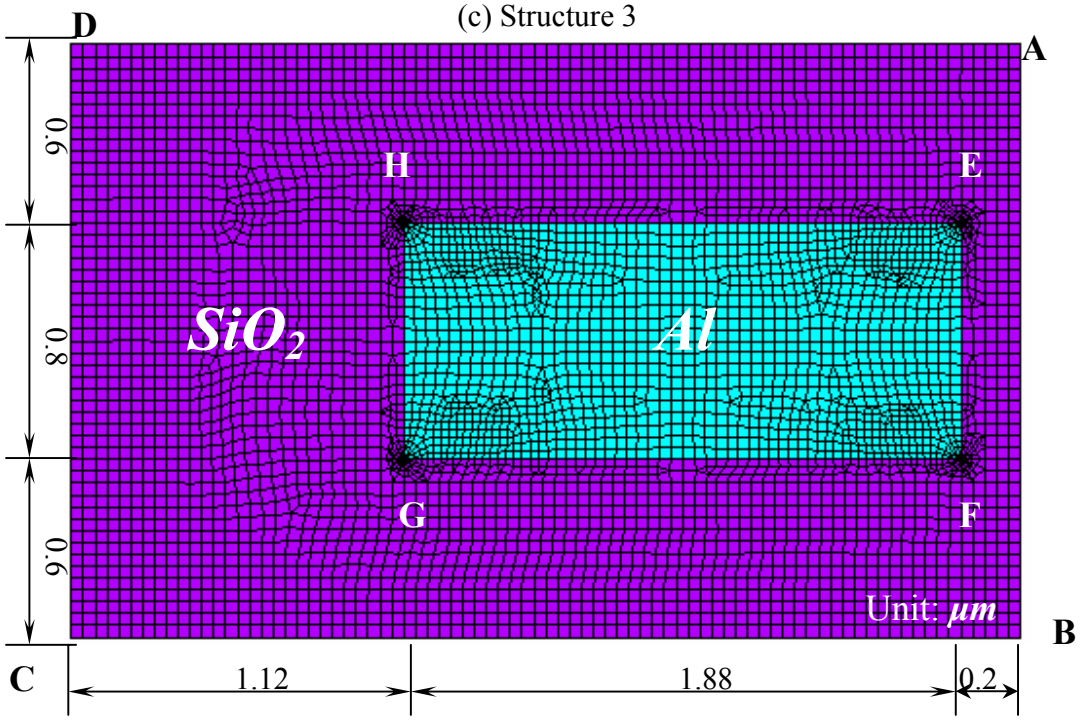

(d) Structure 4

Fig. 6.1 The FEM models of structure1, 2, 3, and 4

6.2.2 Thermal Analysis

The FEM thermal analysis is accomplished by solving the two-dimensional heat conduction equation. Recall equation 2-1 and simplified it to be

$$\frac{\partial}{\partial x}\left(k\frac{\partial T}{\partial x}\right)+\frac{\partial}{\partial y}\left(k\frac{\partial T}{\partial y}\right)+\dot{q}=\rho c\frac{\partial T}{\partial t} \qquad 6\text{-}1$$

Laser processing is a phenomenon in which energy is large enough to melt (or even vaporize) condensed substances in a very short time, leading a superheating effect, which means the heating of a liquid to a temperature above its normal boiling point. Assuming the superheating effect occurs in the period of laser heating aluminum line so that solid and liquid states are treated as one continues region and the phase boundary doesn't have to be calculated explicitly [39]. The pulsed-laser intensity function for the plane FEM model modified from equation 2-4 is given by

$$\dot{q}(x,y;t)=\frac{\alpha(1-R_f)I_0(t)}{x_e}exp\left(-\frac{x^2}{x_e^2}\right)exp(-\alpha y) \qquad 6\text{-}2$$

The optical reflectivity R_f is measured to be 0.89 for aluminum. The absorb coefficient α is given by 8.5 at the laser wavelength 1.064 μm [40]. The radius of the beam is set up to be 3.5 μm. The process begins in the room temperature (20ºC/293K) environment. Because the left and bottom boundaries as well as the top surface are remote from the laser focus heating region, the boundary condition at these borderlines are determined to be the room temperature (293K). As pulsed laser processing involves very rapid melting and solidification, convective flow of heat and radiative absorption of the metal are not as significant as they are in other processes where a liquid state is permanent in a long processing time. Therefore, convection and radiation effects are neglected.

Although it is difficult to understand the detailed bonding situation of dielectric and metal, it is understood that micro-flaws always exist in the interface of them due to the difference of material properties such as thermal diffusibility and surface roughness as performing the deposition process. These defects are one of the primary factors causing link failures, but they sometimes help the formation of microbridges, particularly when

they are located in the corners of the metal lines. As the results, a micro-flaw is generated into the FEM model at the lower right corner. Experimental observation shows that a microbridge is formed from one corner to another corner of the adjacent aluminum line when these defects are correctly placed.

Fig. 6.2 shows the transient temperature distribution at different processing time in case of the structure 2. The laser energy is 0.18 μJ, the minimum energy to form the microbridges for the structure due to the results of the experiments. The nonlinear heat wave was immediately conducted by the aluminum from the surface to the bottom due to its excellent thermal conductivity, corresponding to the rapid increase of temperature within the target. The heat flux was continuously conducted to across the interface to the insulated dielectric, SiO_2, but the heat diffusion rate decreases due to the poor thermal conductivity of SiO_2. Thus, the heat flux wasn't transmitted too far from the aluminum line in the end of laser processing. The heat affected zone (HAZ) at the right side of the aluminum in that time exceeds 0.16 μm wide, which is great than that of other three

sides (about 0.10 μm). It can be inferred that the interconnect probably occurs in that area.

The model demonstrates the aluminum started melting at the center of the aluminum surface when the laser has been processing at 4.0 ns, and then developed the melting-area radially with a bowl-like shape, until all cross section area was melted at 7.0 ns. At the end of laser heating it was found that the skinny red strip ($\geq$ 1973 K, melting point of SiO_2) existed at the upper central of the Al and SiO_2 interface. When increasing the laser energies, the region will be enlarged along the interface to lead the melting of the SiO_2 around the aluminum, shown in the fig. 6.3. However, it has seen that the formation of the microbridges is to undergo the phase change (melting and solidification) processes. When the corner flaw is propagated by the thermal stress, the melting aluminum liquid is drawn into the crack and then solidified to be the interconnect. The result is the same as J. Lee's ones [41], and it is also consistent with the experiment observation in this work.

Finally, this model represents the similar transient temperature

distribution for all structures and energies to indicate that it possesses the ability to obtain deserved solutions with convergency due to the correct heat source input and reasonable assumptions. Moreover, the series of convergent solutions using different energies for each structure provide stable environment for further thermal stress and crack analysis. As the result, it increases the accuracy of predicting the energy window.

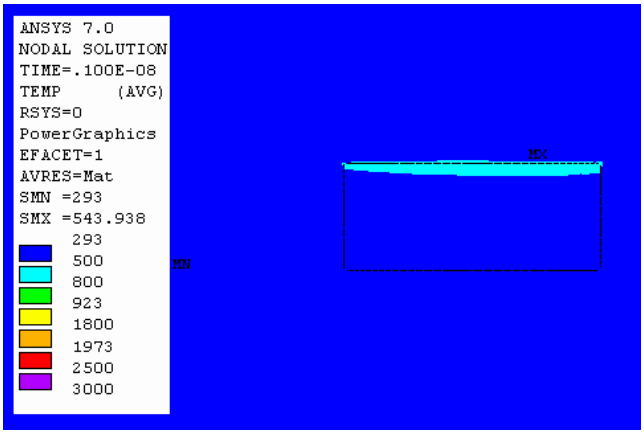

(a) 1 ns

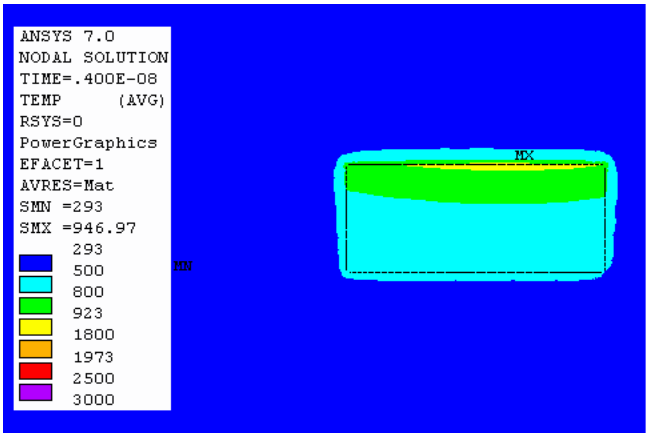

(b) 4 ns

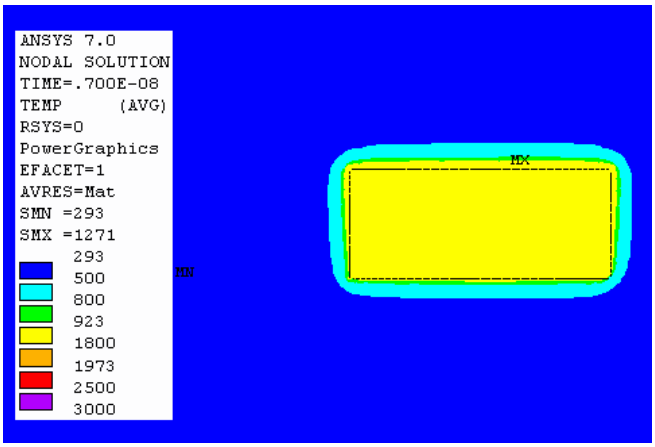

(c) 7 ns

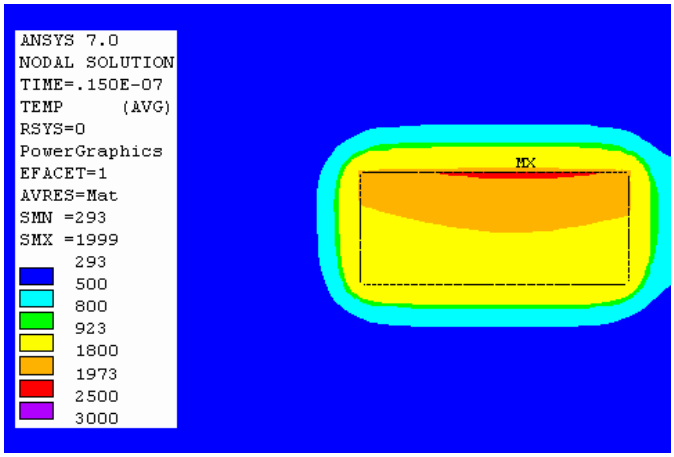

(d) 15 ns

Fig. 6.2 Temperature distribution at various time in case of structure 2 and energy 0.18 μJ

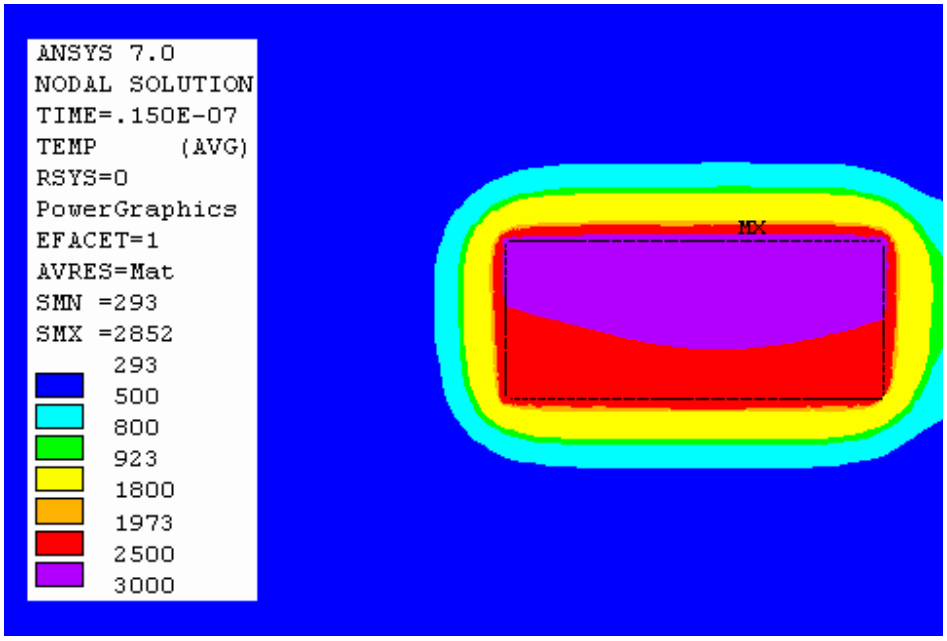

Fig. 6.3 Temperature distribution at various time in case of structure 2 and energy 0.27 μJ

Fig 6.4 presents the temperature distribution at various processing times and laser energies. Section (a) shows the temperature distribution along the *x*-direction on the top surface of aluminum. The maximal temperatures are 2852.04 K and 1999.02 K for the energy 0.27 μJ and 0.18 μJ respectively, occurred at the central segment of the surface of the aluminum at the laser processing time 15 ns, and decreased 156.82 K as well as 104.52 K at the left corner. It can be seen that the temperature

slightly drops along the lateral surface since the left corner of the aluminum is still in the range of the laser spot (1.12/1.75), and the aluminum is surrounded the excellent heat insulator SiO_2.

Section (b) displays along the *y*-direction at the right corner of aluminum line (x = 0.16 μm, local coordinate), beginning from the upper surface. Note that the temperature gradients at the beginning and the end of laser heating (1 ns and 15 ns) for the laser energy 0.18 μJ are 434.02 K/μm and 707.88 K/μm respectively. Similarly, they are 681.53 K/μm and 1062.01 K/μm for the laser energy 0.27 μJ. It can be seen that the vertical temperature gradient increases when the laser power density increases, resulting in higher principal thermal stresses generation.

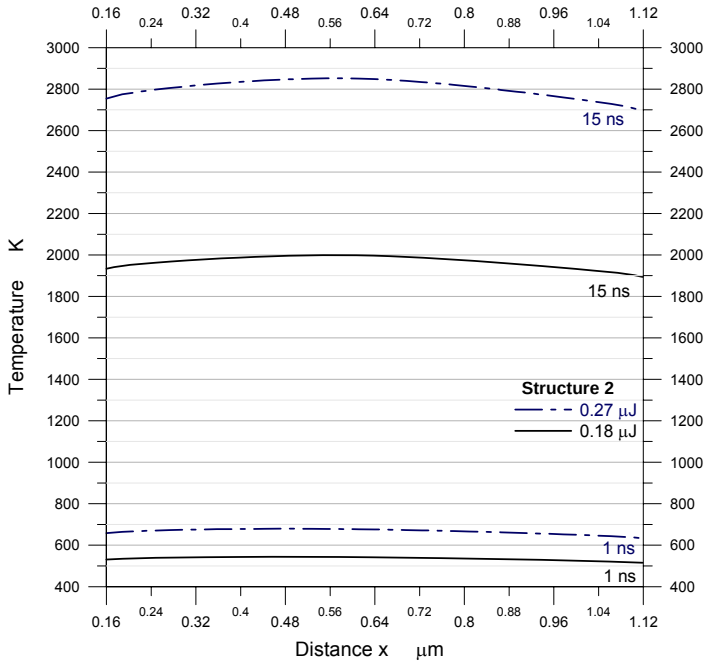

(a).

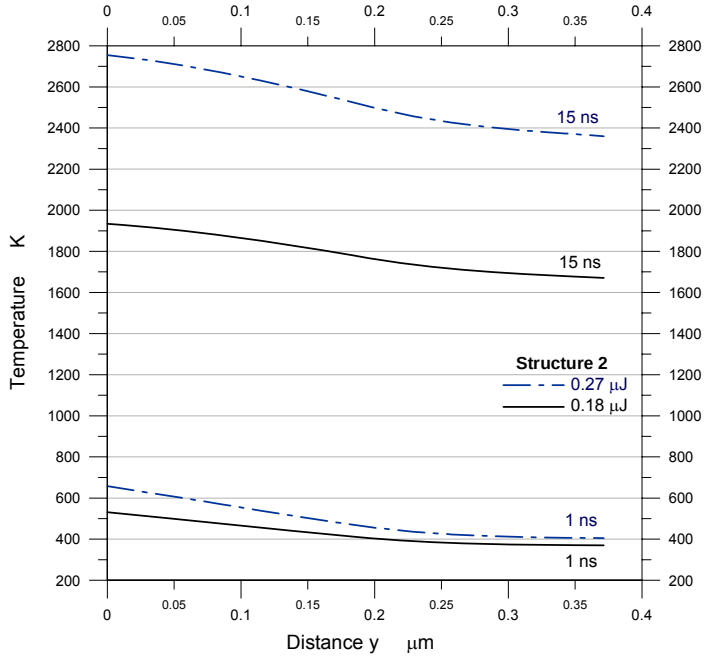

(b).

Fig 6.4 Temperature distribution at various processing time and laser energies: (a). along the *x*-direction on the top surface of aluminum, (b). along the *y*-direction at the right corner of aluminum line

According to the observation of the experiments, the interconnects of the structure 2 were formed from the lower right corner of the aluminum target, where is assumed to be the front tip of pre-crack, to the neighboring line. Fig. 6.5 shows the temperature variation of the point at different processing times, using the lowest and the highest laser energy in the energy window. The temperatures of the point gradually increase during the laser heating period to imply that the thermal stress is generated steadily to induce crack propagation corresponding to microbridge formation.

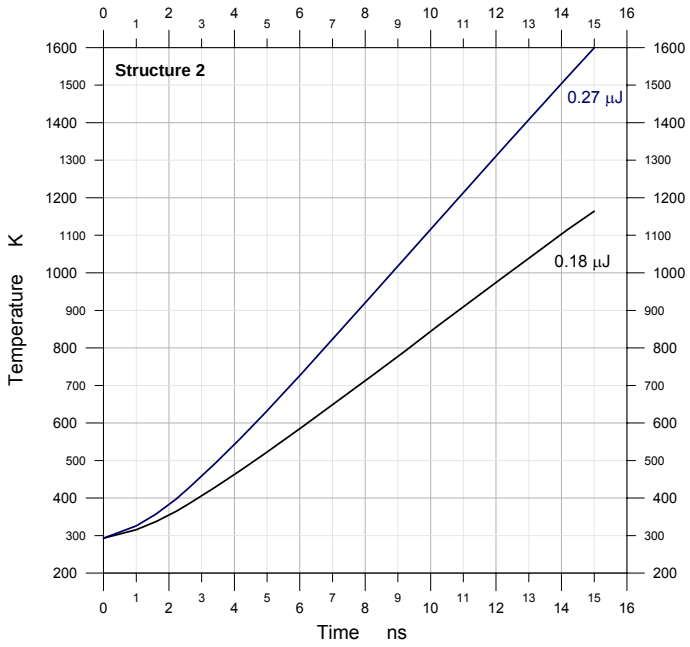

Fig. 6.5 Temperature variation of different processing time at the critical location

6.2.3 Stress Analysis

The structural analysis is to solve the thermoelastic stress–strain-displacement equations using the temperature distribution obtained from the results of thermal analysis as the thermal loading in order to determine the maximum principal thermal stress and strain field in the model where is the critical region of developing cracks to form microbridges. Because the linking process occurs within nano-seconds, the failure pattern of the brittle dielectric (SiO_2) is essentially determined by the initiation, rather than propagation, of the crack.

Fig. 6.6 presents the principal stress field of the structure 3 using the laser energy 0.22 μJ. It can be seen that high tensile principal stresses occur near the corners of the aluminum lines. Because the pre-crack is generated in the left lower corner of the right side aluminum line due to the observation of the experiments, as shown in the figure 6.7, the principal stress between the corner is found slightly higher than that of the other corners. As the result, the potential microbridge is expected to be initiated

from the left lower corner of the right side aluminum line to the right lower corner area of the left side aluminum line.

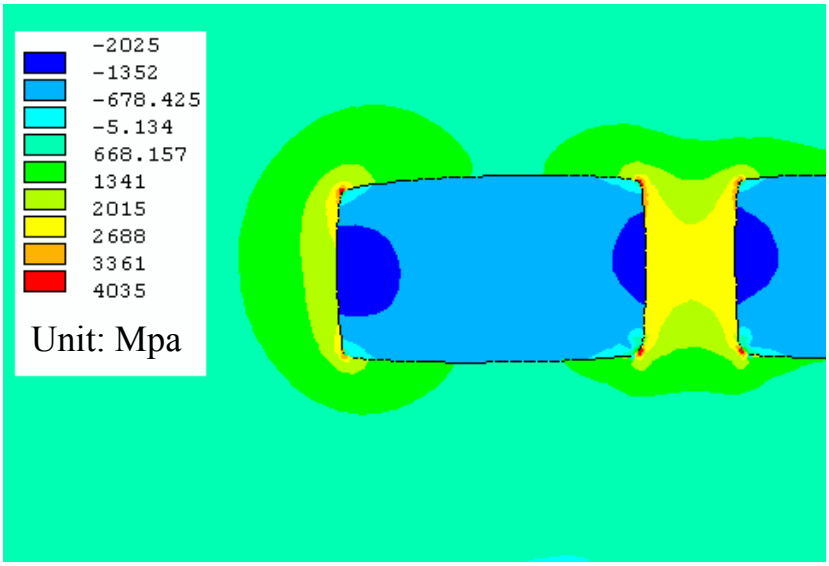

Fig. 6.6 The principal stress field of the structure 3 using the laser energy 0.22 μJ

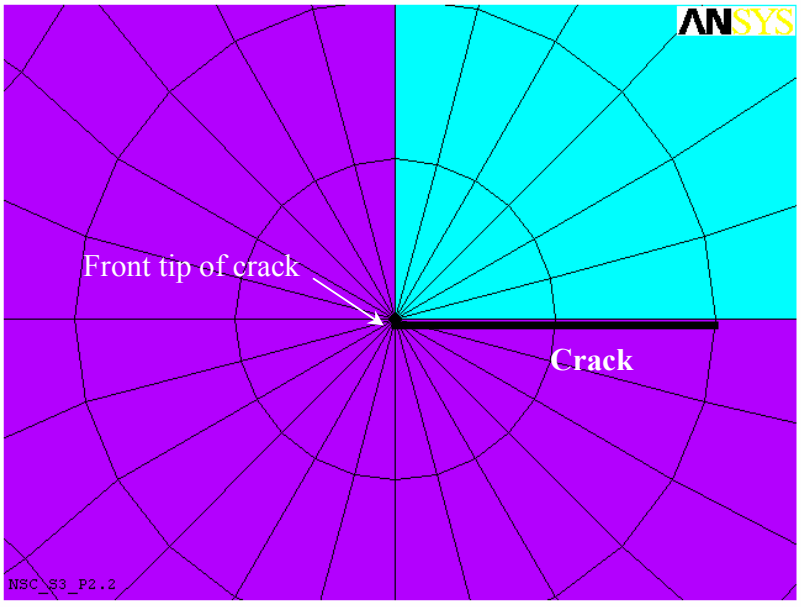

Fig. 6.7 The crack layout of this work

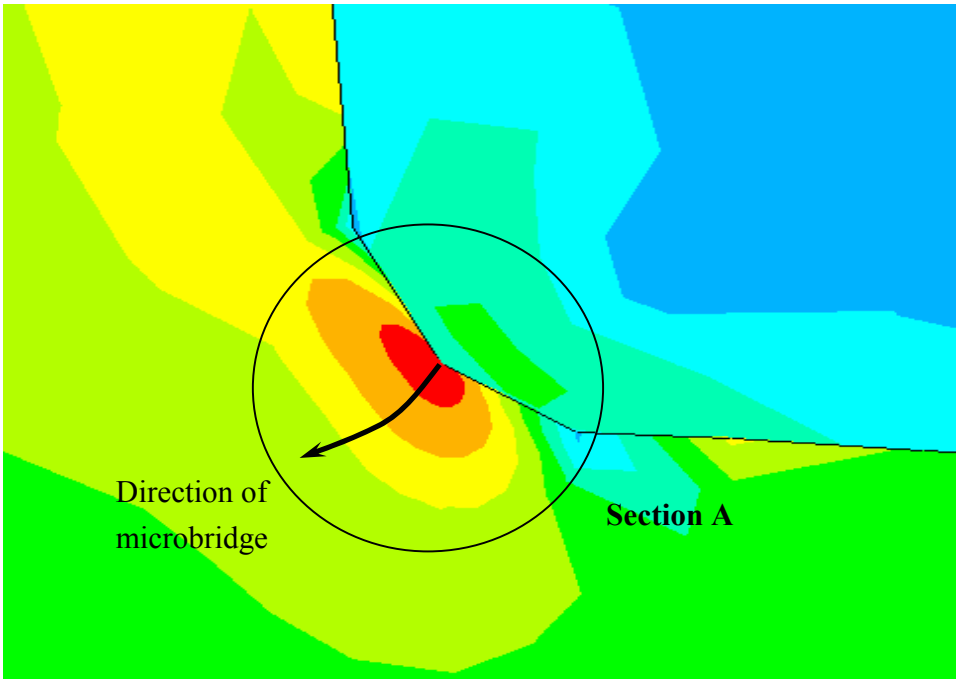

(a) Simulation

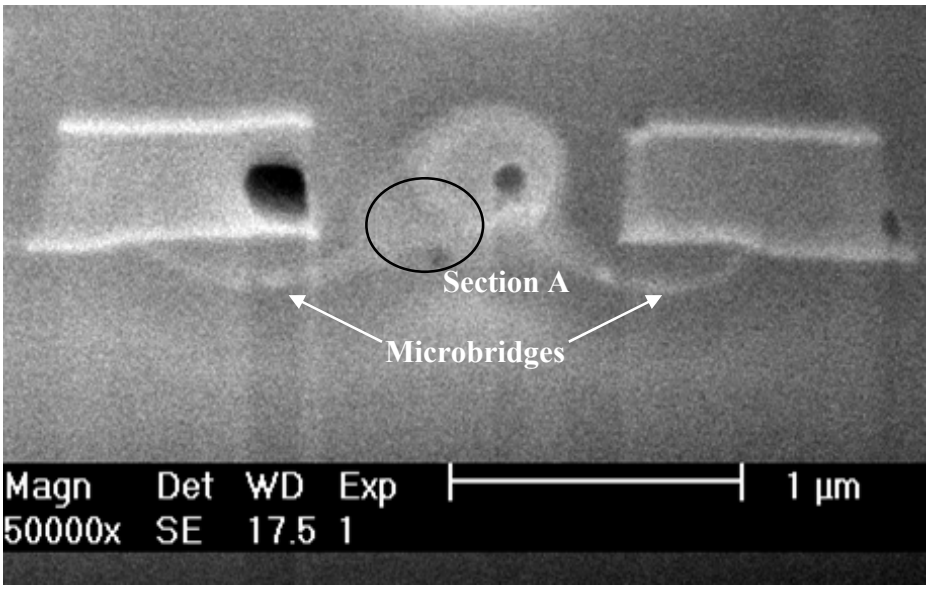

(b) Experimental

Fig. 6.8 The comparison of the simulation and experimental results

Figure 6.8 shows the comparison of the simulation and experimental results. Section (a) displays the magnification of the left lower corner of the right side aluminum in figure 6.6. The possible microbridge path modeled perpendicular the various contour of the principal stress (the direction along with the maximum principal stress is oriented) is consistent with the observation of the experiments, as shown in the FIB picture of the section (b).

6.2.4 Crack Analysis

Figure 6.9 presents a comparison among a pure LEFM (Linear Elastic Fracture Mechanics) analysis, the Irwin correction, the strip yield correction [22], and FEM correction for each structure. The effective stress intensity K_{eff} and stress σ are nondimensionalized by $\sigma_{YS}\sqrt{\pi a}$ and σ_{YS} respectively. The LEFM analysis predicts a linear relationship between stress intensity and stress. The Irwin and strip yield corrections derived from LEFM theory at stresses greater than 0.5 σ_{YS} [22] to predict the more realistic fracture behavior (the plastic zone

development at the crack tip) for different materials such as steels, ceramics and polymers. Most of the FEM models presents the relationship of the stress intensity and stresses between the LEFM analysis and Irwin/strip yield corrections but near the later. It can be concluded that these FEM models predict more realistic crack initiations in order to form the microbridges since the crack tip plastic zones at the corner of the aluminum line are closer the realistic corrections than the ideal LEFM.

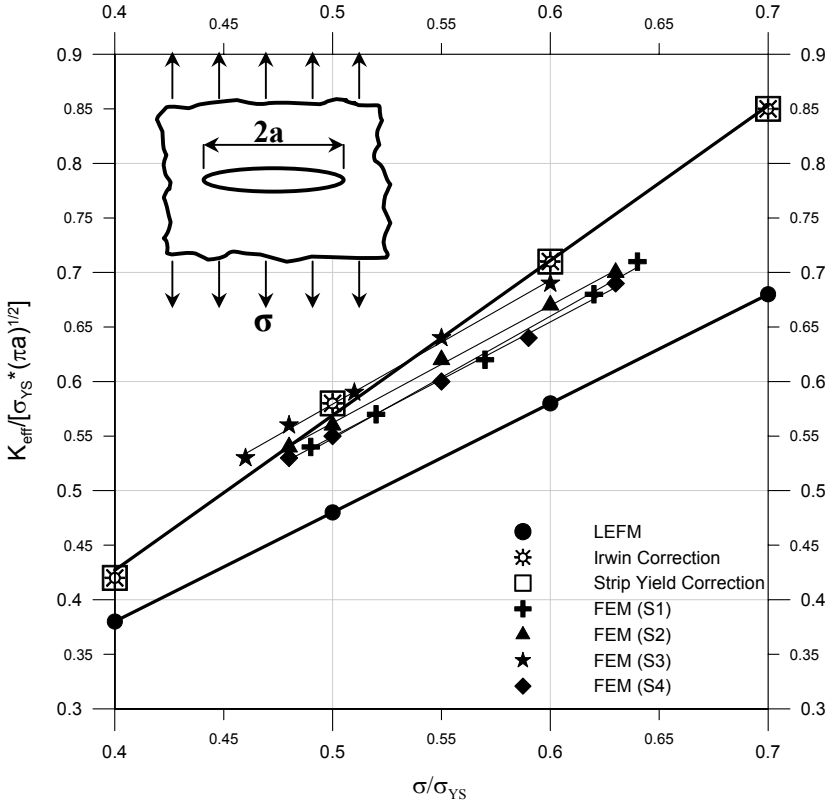

Fig. 6.9 The comparison of the plastic zone corrections in plain strain situation

The crack analysis is accomplished in the FEM model by calculating the value of the stress intensity K at the critical region (pre-crack tip). Assuming the microbridge is formed when the fracture toughness in the front tip of pre-crack (K) is greater than that of the dielectric (e.g. SiO_2 is 0.79 Mpa*$m^{1/2}$). It can be one of the failure criteria to state the threshold energy of forming microbridge corresponding to the lower bond of energy window. When applying a laser energy higher than the threshold energy, the principal stresses at the pre-crack region increase as well. According to the observation of experiments, the increased stresses at the critical area can't inhibit the formation of the microbridge until they exceed the yield strength of the dielectric (SiO_2), resulting in the permanent deformation in the region. Fig.6-10 presents the FIB picture of structure 2 imposed by high energy to fail the formation of microbridge due to the severe distortion between aluminum lines. The right corner of the picture shows magnification of the critical region, which demonstrates the permanent deformation of the Al lines.

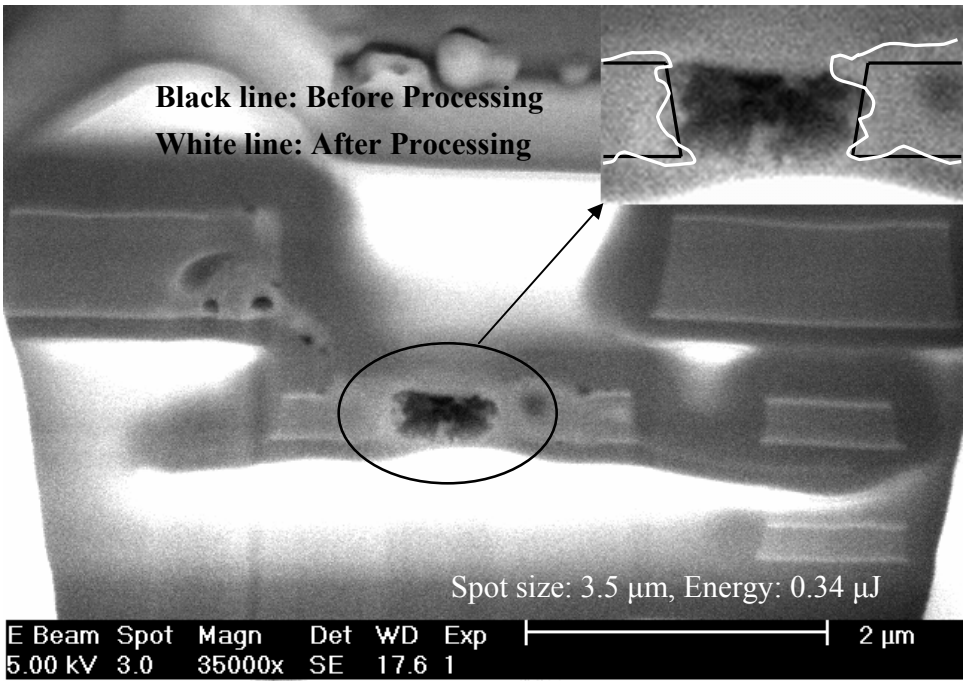

Fig. 6-10 The FIB picture of structure 2 imposed by high energy

As the result, another failure criterion called Von Mises-Hencky theory is assumed to be the upper bond of the energy window. The Von Mises-Hencky stress σ_v is calculated according to the equation [42]

$$\sigma_v = \sqrt{\sigma_1^2 - \sigma_1\sigma_2 + \sigma_2^2} \qquad 6\text{-}3$$

$$\sigma_{1,2} = \frac{\sigma_x + \sigma_y}{2} \pm \sqrt{(\frac{\sigma_x - \sigma_y}{2}) + \tau_{xy}^2}$$

Where σ_1 and σ_2 are the principal stresses

If the Von-Mises-Hencky stress σ_v at the critical pre-crack region is great than the yield strength of the SiO_2 (8.4 GPa), the microbridge is destroyed by the distortion of the dielectric. Fig. 6.11 Shows the variation of the Von-Mises stresses against the laser energies within the energy window for each structure. The Von-Mises stress is nondimensionalized by σ_{YS}, the yield strength of SiO_2. The Normalized Von-Mises stress linearly increases for all structures when applying those laser energies within the energy windows. The increase rates for structure 1, 2, 3, and 4 are not obviously different, which are 4.13/μJ, 4.03/μJ, 4.02/μJ, and 3.51/μJ respectively. This is because geometric parameter, the interspacing of aluminum lines, is similar for these structures.

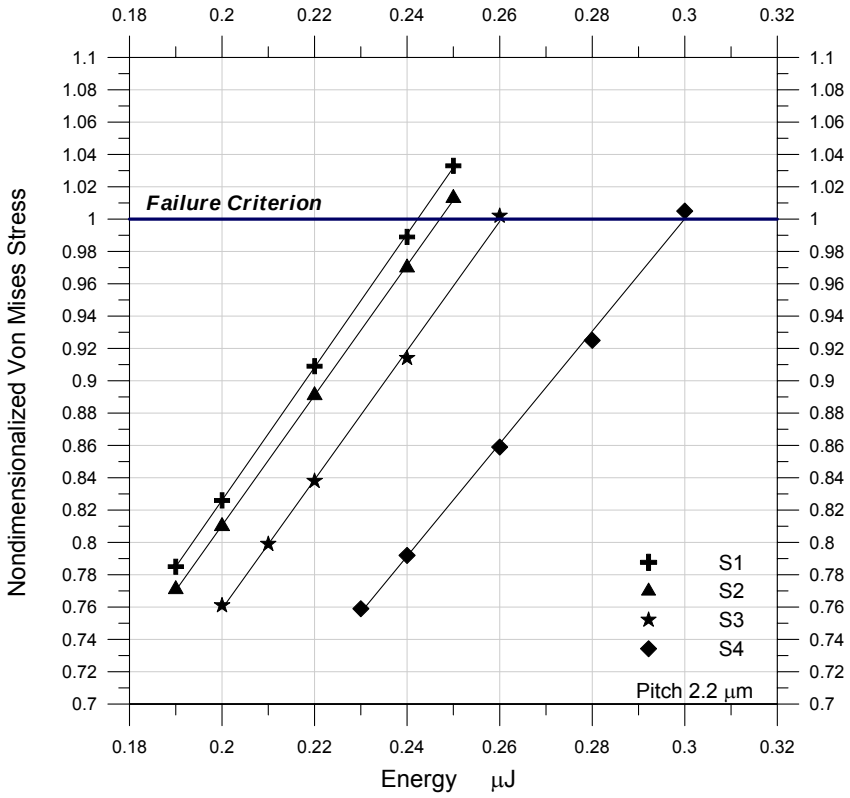

Fig. 6.11 The variation of normalized Von-Mises stress vs. laser energies

6.3 Comparison with Experiments

Laser processing experiments were performed to compare with the FE modeling. Fig. 6.12 shows the energy window (relative and absolute) comparison of the experimental and simulation. According to the failure criteria mentioned in the previous paragraph, the FE simulation presents an energy window for each structure. It can be seen that the simulative energy window of the structure 1 and 2, and 3 are more conservative than the experimental energy window since the assumptions of the LEFM in these FE

models simplifies the realistic situations such as laser position accuracy as well as temperature-dependent material properties. But the simulation of structure 4 displays more optimistic process window than the experimental ones since it didn't consider other potential failure criteria such as passivation breaking. Further note, the results of the FE analysis for microbridge formation are consistent with the experimental results. This demonstrates the model's ability to predict the success of more complex processes and patterns.

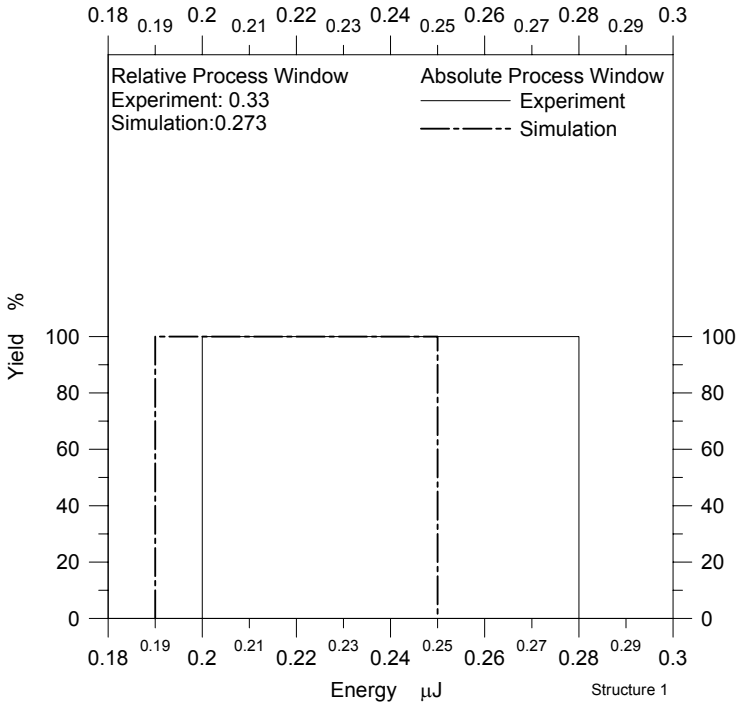

(a) Structure 1

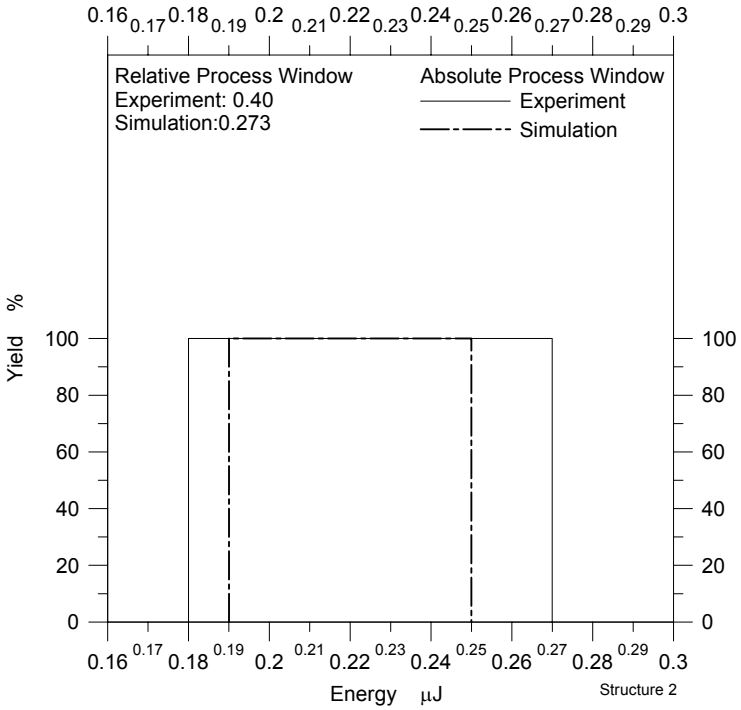

(b) Structure 2

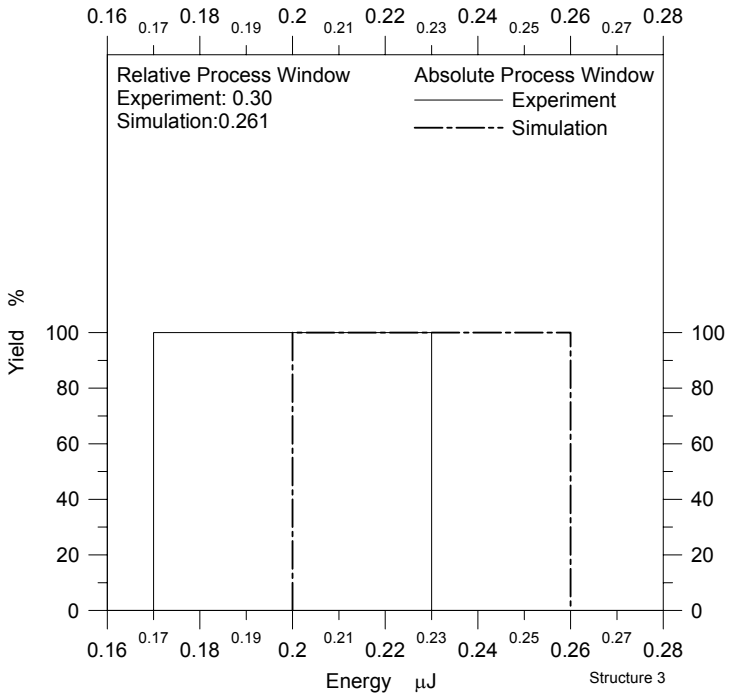

(c)Structure 3

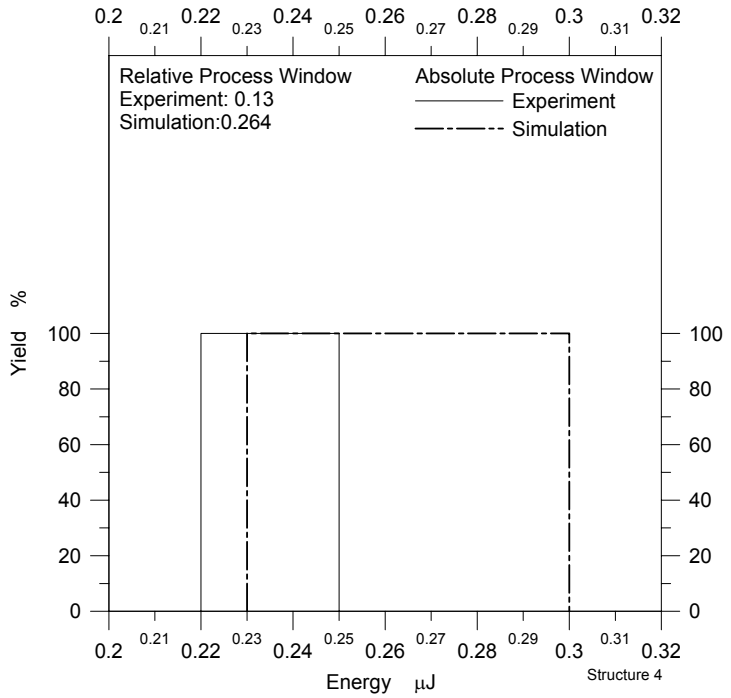

(d) Structure 4

Fig. 6.12 The comparison of experiment and simulation in energy windows

Chapter 7: Design Optimization

7.1 Introduction

It is one of the major advantages using the FEM analysis to study geometric effects since the model can be quickly modified. To optimize the geometry of the metal interconnect by FEM simulation is significant in the design of the microbridges in order to obtain the trade-off of the structure performance and the production yield.

The design variables affecting MakeLink resistance and yield are interline spacing (**D=2d**) and the width-to-height ratio of metal lines (Width: **W**; Height: **H**). The objective is to design the structure for the broadest process window in a given design space, regarding to the semiconductor manufacturing processes. We setup the laser spot size to be 3.5 μm, which is general used in the 0.11 - 0.18 μm IC manufacturing processes. The design space is

$$\begin{aligned} &\text{Design Space} \le 0.8 \times \text{Spot Size} \\ &\Rightarrow d + W \le 1.4 \end{aligned} \qquad \text{7-1}$$

And the design constraints are

$$0.4 \le H \le 0.8$$
$$0.08 \le d \le 0.4 \qquad \text{7-2}$$
$$W \ge 0.4\,(\text{Max. d})$$

Our study here shows the results of processes performed on two material systems, Al/SiO_2 and Cu/Low-k dielectric. Al/SiO_2 is the most common combination used in mature integrated circuits (IC) manufacturing (above 0.11 μm). Cu/Low-k has surfaced to replace Al/SiO_2 in ultra-large-scale integration (ULSI) in order to solve the issues of RC delay, cross-talk noise, and power dissipation. To obtain optimal combination of geometric factors in each interconnect system, the FE model was performed using different values of these parameters to find process windows for each one. The yield strength of low-k materials is unpublished, and thus, only threshold energies can be obtained in Cu/Low-k analysis. In fact, the low-k material properties vary from manufacturer to manufacturer. No superior low-k dielectric has been universally accepted. The values applied in the analysis are general so that the results of the modeling of Cu/low-k are guidelines only.

7.2. Aluminum/Silicon Dioxide (Al/SiO_2)

7.2.1 The Impact of Interline Spacing

Fig. 7.1 displays the variation of the related process windows using different half-distances (**d**) between two aluminum lines from 0.08 μm to 0.32 μm. Note that the interline spacing (**D**) of the two aluminum lines is equivalent to the twice the half-distance (**D = 2d)**, and the size of the aluminum lines stays the same when doing the interline spacing comparison. The relative energy windows tend to increase with increased interline spacing of the aluminum lines. The slope of the curve (increasing rate) rapidly increases with the half-distance from 0.12 μm to 0.16 μm, but the slope lowers after 0.16 μm. This means the absolute process windows are not obviously different when the interline spacing is larger than 0.32 μm.

Computer modeling experiments on the structure with **d**=0.16 μm and **d**=0.13 μm demonstrate a relative process window decreases (0.333 – 0.322) when the spacing between the two aluminum lines is scaled down. In general, the simulation results show that the process window becomes

more narrow as the interline spacing decreases making it more difficult obtain a successful microbridge with 100% yield. Abnormal factors, such as material property variation and equipment stability, further impact the process negatively. Thus, it is easier to obtain high yield with large interline spacing from a process window point of view.

Fig. 7.2 shows the variation of the temperature at the crack tip with different interline spacing using the laser energies of 0.20 μJ and 0.24 μJ respectively. Higher temperature occurs in the critical region when the spacing decreases, corresponding to higher thermal stresses to form the microbridge. The model indicates that the interline spacing between the two aluminum lines can't be narrowed to less than 0.16 μm since the temperature of the crack tip increase rapidly when the half-distance is less than 0.08 μm. This results in the plastic instability around the region of the crack tip due to the very high temperature. Further note, the crack tip temperature does not increase conspicuously when the half-distance is reduced from 0.32 μm to 0.16 μm. Thus, there is no advantage to larger spacing. The molten aluminum has to flow a longer distance along the

empty crack in order to form a good “electric” connection. Assuming the cooling rate and flow-speed of the molten metal are same for each spacing, it needs more time to “travel” to the destination with larger spacing. It could stop (re-solidification) before it reaches the corner of the other metal. Based on the simulation results, an optimal interline spacing between the two aluminum lines exists from a yield point of view.

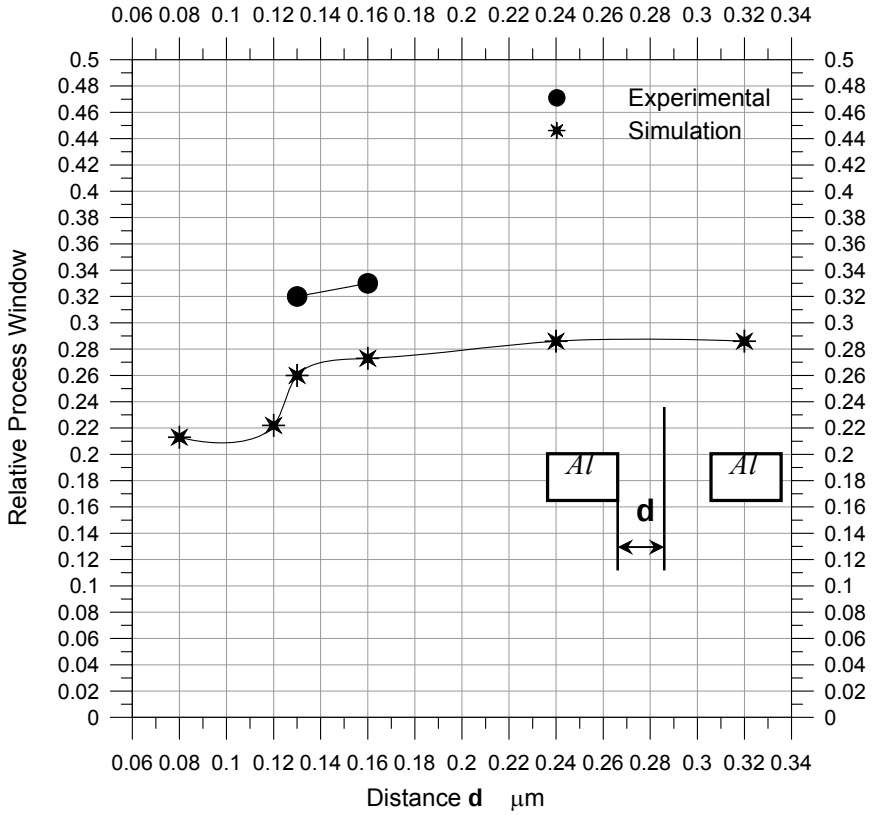

Fig. 7.1 The variation of the related process windows with different interspacing of two aluminum lines

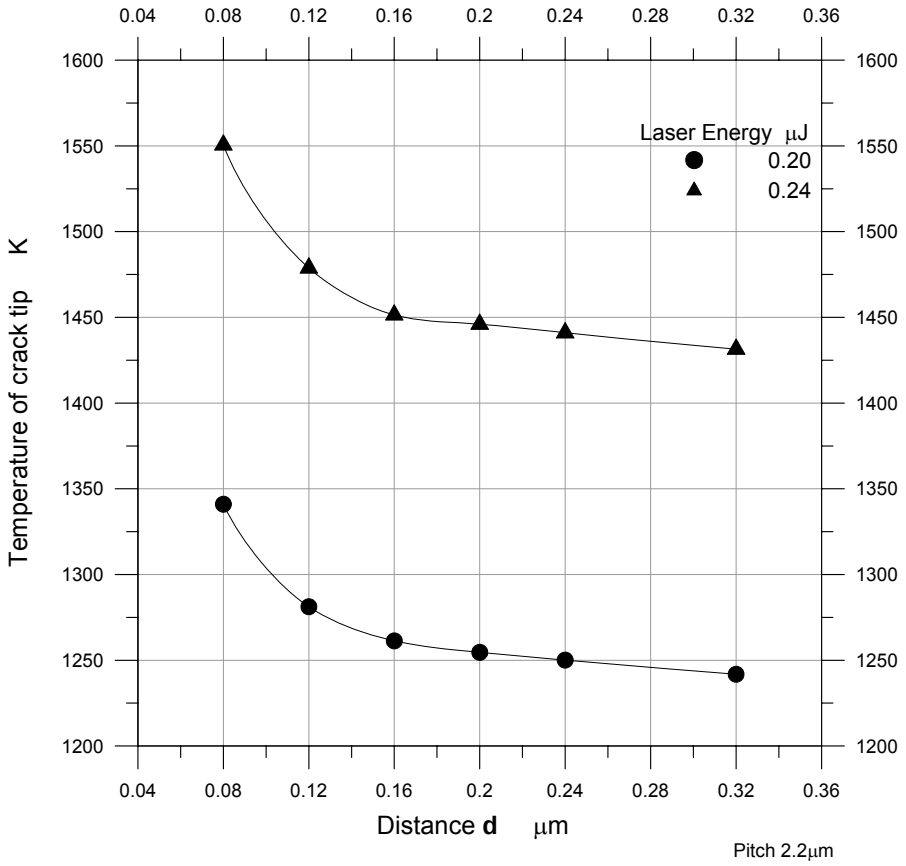

Fig. 7.2 The variation of the temperature at the crack tip with different interspacing using the laser energies 0.20 μJ and 0.24 μJ

7.2.2 The Impact of the Width-to-Height Ratio of the Aluminum Line

Fig. 7.3 presents the variation of the related process windows by changing width-to-height ratios of the targeted aluminum line (Remember: process window refers to the range of parameter variation over which near-100% yield is accomplished). The height of the aluminum line is fixed to be 0.4 μm, but the width is changed from 0.4 μm to 1.6 μm, shown as a

ratio change from 1 to 4. The relative process window increases when the ratio increases from 1 to 2.5. But it decreases when the ratio is great than 2.4. Our model shows that the microbridge reaches the Von-Mises failure stresses at smaller laser energy when the width-to-height ratio is great than 2.4.

Apparently, a negative mass effect exists as the ratio is great than 2.4, leading to much more heat flux through the crack tip to produce higher thermal stress due to the mismatch of thermal expansion between the Al and SiO_2. The high width-to-height ratio of the aluminum line along with the narrow process window makes it difficult to obtain high yield in the face of process variations. Based on the simulation results, an optimal width-to-height exists from a process point of view. Our experiments agree with simulations, and both exhibit the same maximum. Hence, the model is validated with experiment and predicts that the best width-to-height ratio for high yield, 2.4.

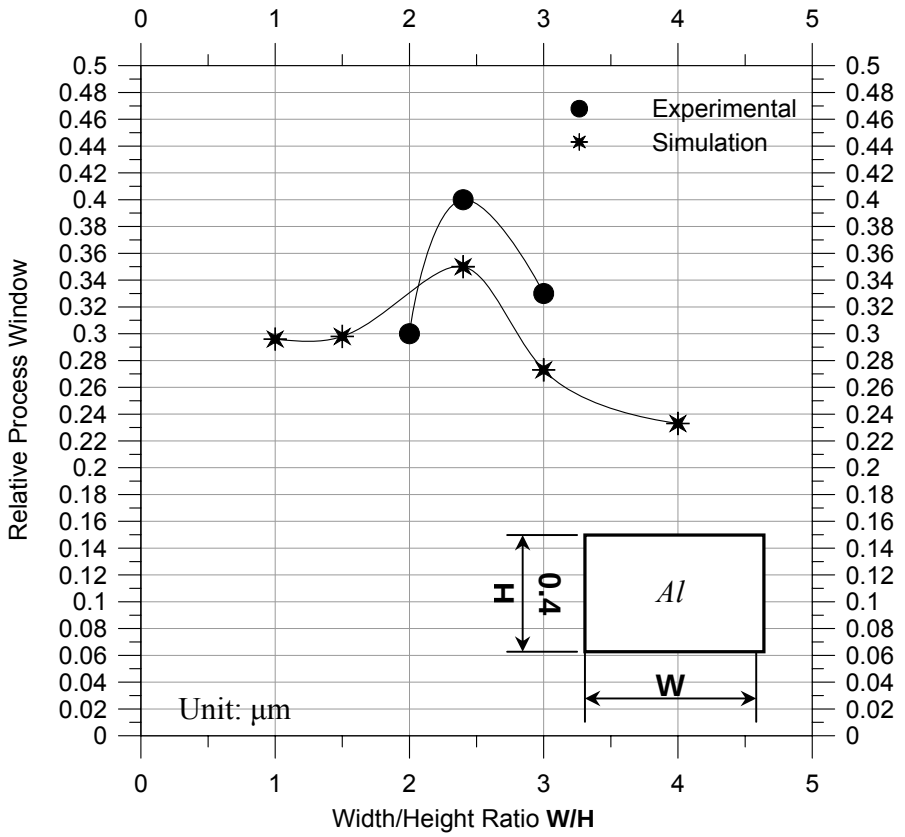

Fig. 7.3 The variation of the related process windows with different width/height ratio of the targeted aluminum line

Fig. 7.4 provides the optimal design diagram for Al-SiO_2 interconnections, based on the results of our FE modeling. Line **AB** and **CD** are the side constraints of the structure design. The bounding point was obtained by FE modeling of different widths of the Al lines at a fixed interline spacing to find the optimal width yielding the broadest process window. For instance, the simulations shown in the fig. 7.3 is an example

of the optimal design shown in fig. 7.4. The highest point of simulation in the fig. 7.3 (W=0.96 μm, d=0.16 μm, and H=0.4 μm) is selected to be the bounding point **P 1** in fig. 7.4.

It needs larger width when the half interline spacing is 0.16 μm, but it is opposite when the interline spacing smaller or bigger than that. Further note, the optimal width maintains the same value when the interline half-pitch is large than 0.32 μm. In general, the optimal width is not larger than 1.2 μm for all cases. Area **ABCD** is a feasible region to provide the designer the optimal dimensional combination in order to avoid unformed links. Using our model, the designer can study trade-off requirements such as resistance and size for improving yield.

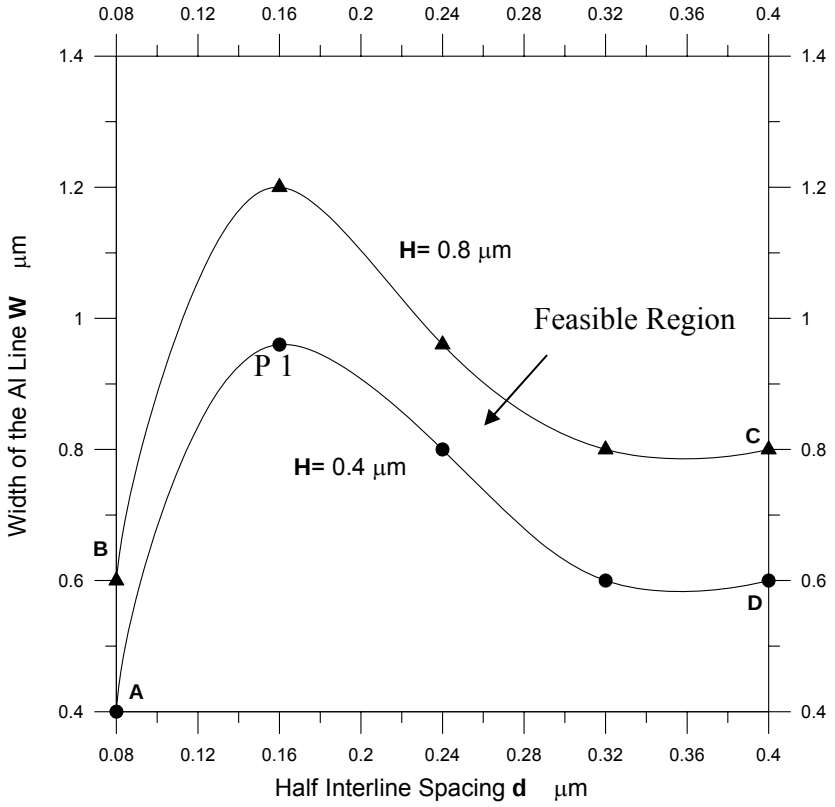

Fig. 7.4 Optimal design diagram for Al-SiO_2 interconnections

7.3 Cu/Low Electric Constant Materials (Cu/Low-k)

Table 7.1 presents the material properties (Cu/Low-k) used in FE modeling. Fig. 7.5 displays the variation of the threshold energies by changing half-distances between two aluminum lines from 0.08 μm to 0.32 μm. The threshold energy monotonically increases with increasing the interline spacing of two copper lines. This means forming a "long" microbridge requires higher

laser energy. Fig. 7.6 presents the variation of the threshold energies by changing width-to-height ratios of the targeted copper line. The height of the copper line is fixed to be 0.4 μm, and the width is changed from 0.8 μm to 1.6 μm, regarding with the ratio from 2 to 4. It can be seen that the lower ratio needs higher energies to form microbridge. If the ratio is lower than 2, much higher energy must be applied to the copper to form a successful microbridge. The intensely high laser energy results in very high temperature within the structure, leading other temperature-dependent failures such as delamination between copper and low-k materials. As the result, the mass effect is large than the distance effect in the Cu/Low-k system. This is a critical design point: geometry of the copper line itself is more important than interline spacing in achieving a high-yield process.

	Cu	**Low-k**
Thermal conductivity (W/mK)	392 [38]	0.25 [48]
Specific heat (J/kgK)	385 [38]	1,500 [53]
Mass density (kg/m^3)	8,941 [38]	1,000 [48]
Melting Point (K)	1,357 [38]	--
Young's modules (GPa)	110 [45]	2.5 [52]
Poisson ratio	0.3 [45]	0.33 [53]
Thermal expansion Coefficient, CTE (1/K)	$17*10^{-6}$ [45]	$66*10^{-6}$ [52]
Absorption Coefficient (Wavelength: 1047 nm)	6.86 [46]	--
Reflectivity	0.85 [46]	--
Toughness (Mpa-$m^{1/2}$)	--	0.6 [52]
Yield Strength (Mpa)	--	--

Table 7.1 The material properties (Cu/Low-k) used in FE modeling

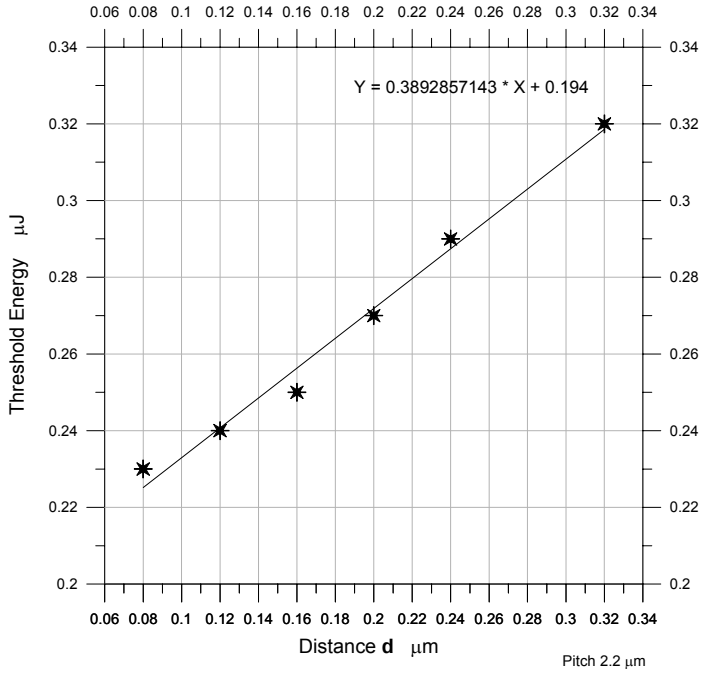

Fig. 7.5 The variation of the related process windows with different interspacing of two Cu lines

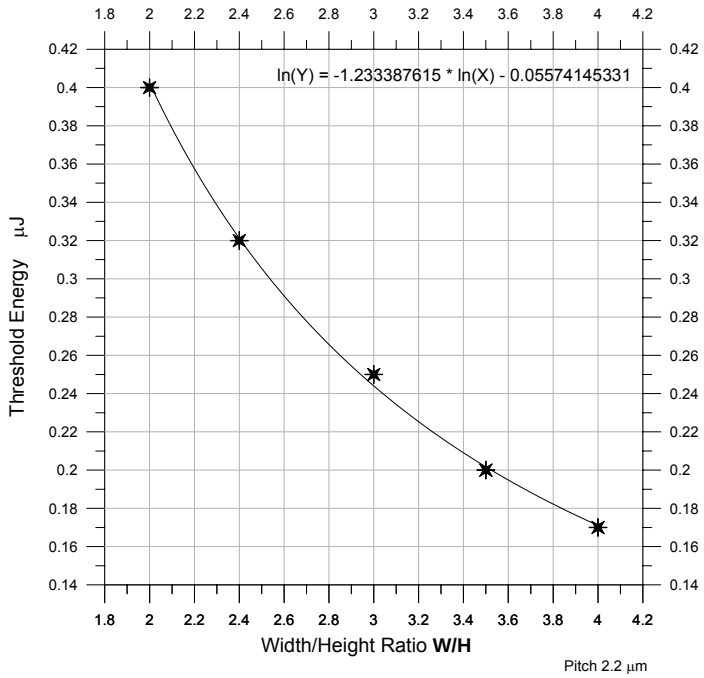

Fig. 7.6 The variation of the related process windows with different width/height ratio of the targeted Cu line

Chapter 8: Conclusions and Future Work

8.1 Conclusions

1. The microbridges were successfully formed for all designs, presenting different performance (link resistances) and productivity (energy windows).
2. The yield improvement is accomplished for each structure by a selected optimal energy.
3. The laser processing experiments show that two-lower-level-metal-line design (structure1 and 2) has higher performance (low link resistance), higher productivity (broad energy window), and higher yield than the three-lower-level-metal-line (structure 3) design. Therefore, it can be considered as the optimal design from the processing point of view.
4. The two-lower-metal-line with lateral gap design (structure 2) provides better scalability and it can be used in next generation ICs.
5. If high-speed is the primary concern, the advanced-lateral design (structure 4) is the best structure, corresponding to its much lower resistance.

6. The median-times-to-failure of all test structures (structure 1, 2, and 4) are great than nine years in operating condition, presenting reasonable cycle times for integrated circuits used in the market. Further note, structure 4 has the best lifetime with its robust arm of microbridge to resist the degradation.
7. A two-dimensional finite element plane models for microbridge formation is developed. Results are compared to the experiments with process windows to present their consistence.
8. The simulation results of interline spacing of the two Al lines are compared with experiments to show that they have the same trend in some specific dimensions. Also, the model is validated with experiment and precisely predicts the best width-to-height ratio (2.4) for the greatest process window.
9. An optimal design diagram for the Al/SiO_2 system is created to provide the designer with criteria to avoid the failure of structure. Trade-off requirements, such as process window and structure size, are also provided.

10. Guidelines are obtained for the Cur/Low-k dielectric system. Also, the aspect ratio of the copper line is shown to be more critical than interline spacing in achieving a successful outcome for this system.

8.2 Future Work

In order to design the more robust microbridge structures to overcome the potential issues of processing, reliability, and scalability in the future, more research must be conducted in following,

1. Apply the microbridge designs presented in this work to different semiconductor interconnect systems to verify their performance, productivity, reliability, and scalability in these systems.
2. Modify the FEM model from two dimensions to three dimensions to simulate more realistic situation of forming microbridges.
3. Consider more design variables such as passivation thickness and location of dummy metals to improve the design optimization.

Appendix A: Structure Dimension

Die size: 

a:705.76; b:1675.8

Note: Structure 1, 2, and 3 have a same frame dimension

Unit: **μm**

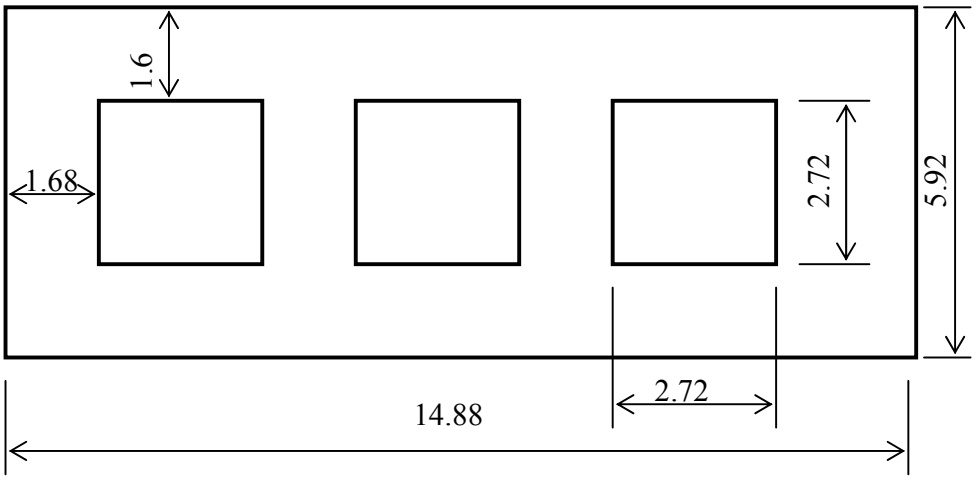

Structure 1

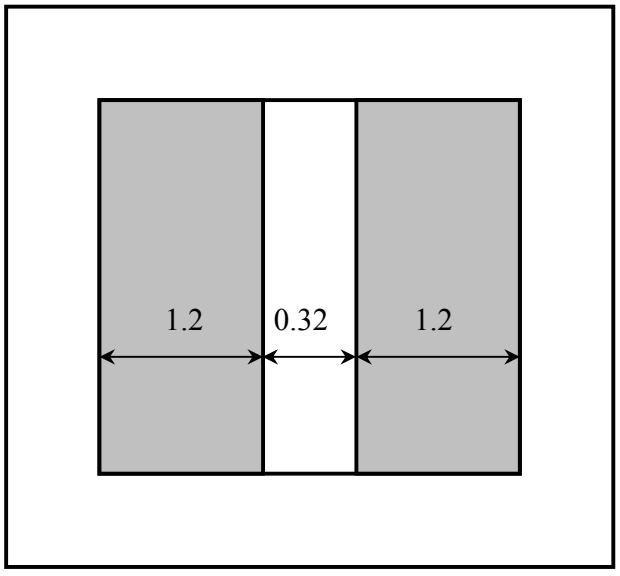

Structure 2

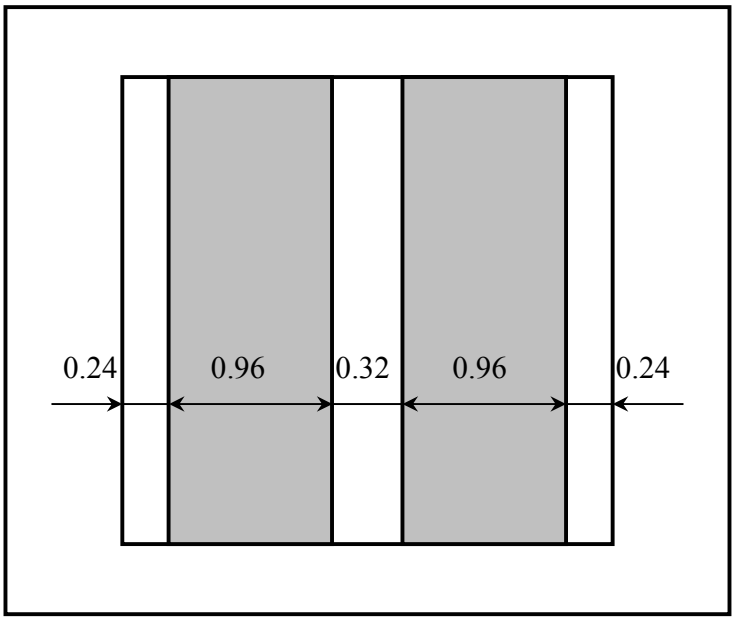

Structure 3

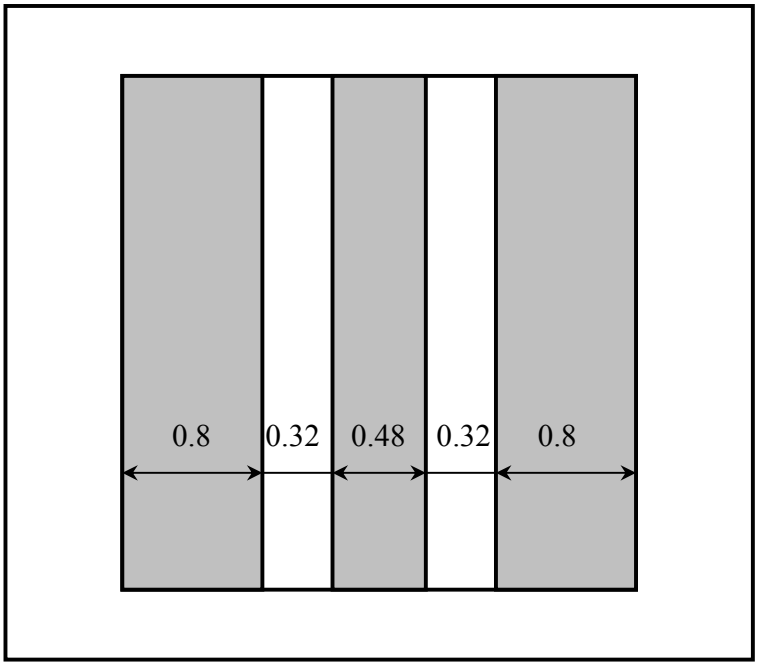

Structure 4

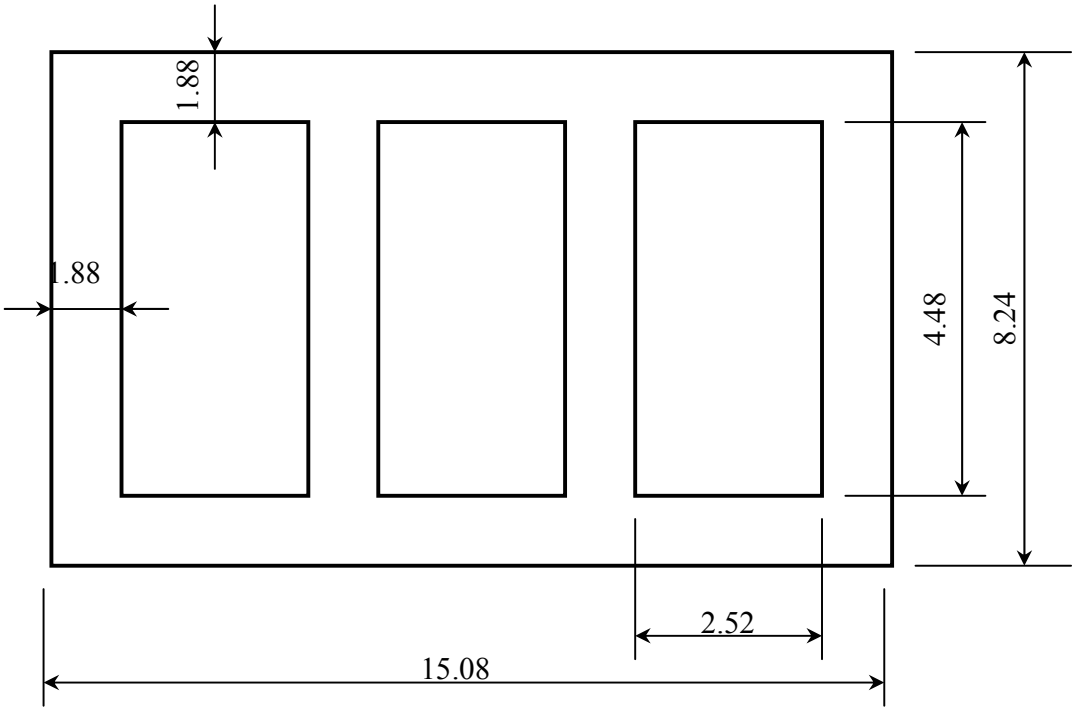

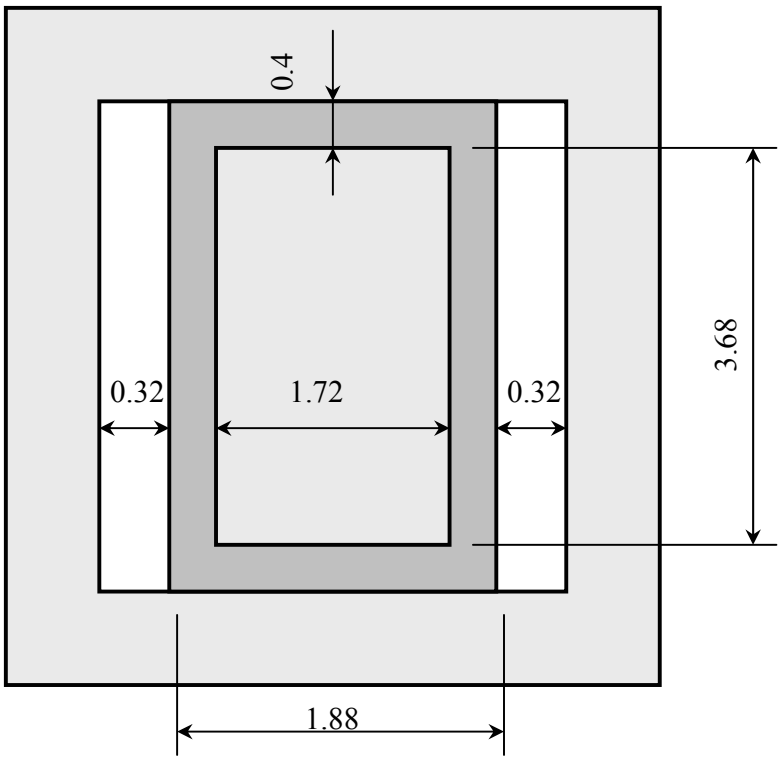

Appendix B: Input Data of Accelerated Stress Tests

Note: for lognormal distribution, t_{50} (median time to failure) = exp(μ)

Structure 1								
	523K 0.54 MA/cm^2		**473K 0.54 MA/cm^2**		**473K 0.33 MA/cm^2**		**423K 0.54 MA/cm^2**	
F: Fail	F	14.40	F	79.23	F	206.55	F	517.11
S: Success	F	18.74	F	85.08	F	224.25	F	688.90
Unit: hour	F	23.01	F	99.28	F	263.69	F	909.86
	F	47.65	F	135.70	F	550.58	S	2974
			F	181.52			S	2974
			F	292.59				
Mean (μ)	3.15		4.87		5.66		6.80	
Std (σ)	0.58		0.55		0.47		0.50	
t_{50} (hr)	23.34		130.32		287.15		897.85	

Structure 2								
	523K 0.54 MA/cm^2		**473K 0.54 MA/cm^2**		**473K 0.33 MA/cm^2**		**423K 0.54 MA/cm^2**	
F: Fail	F	12.38	F	118.14	F	261.01	F	304.67
S: Success	F	24.01	F	170.79	F	529.55	F	478.06
Unit: hour	F	30.06	F	190.03	F	863.61	S	1846
	F	49.44	F	338.61			S	1846
			F	507.84			S	1846
							S	2974
Mean (μ)	3.25		5.44		6.20		6.64	
Std (σ)	0.67		0.66		0.73		0.75	
t_{50} (hr)	25.79		230.44		492.75		765.09	

Structure 4								
	523K 0.54 MA/cm^2		**473K 0.54 MA/cm^2**		**473K 0.33 MA/cm^2**		**423K 0.54 MA/cm^2**	
F: Fail	F	16.03	F	140.71	F	271.36	F	871.29
S: Success	F	18.85	F	260.61	F	341.18	F	1122.54
Unit: hour	F	42.54	F	305.11	F	481.13	S	1846
			F	418.68	F	645.21	S	1846
							S	1846
Mean (μ)	3.15		5.57		6.02		7.21	
Std (σ)	0.60		0.52		0.45		0.39	
t_{50} (hr)	23.34		262.43		411.58		1352.89	

Appendix C: Parameter Calculations (Structure 1 Only)

Note that the structure 2 and 4 are calculated by the same procedures with different input data so that they are not presented in here. According to JEDEC Standard JESD63 [7], the parameters of **n** and $\mathbf{E_A}$ of the structure 1 are calculated as following

1. **n** estimation

$$X_{1i} = ln\, J_i$$
$$X_{11} = 13.21$$
$$X_{12} = 12.69$$

$$Y_i = ln\, t_{50}(J_i)$$
$$Y_1 = 4.87$$
$$Y_2 = 5.66$$

$$N_s = \sum_i s_i = 6 + 4 = 10$$

$$X_{1av} = \sum_i s_i X_{1i} / N_s = \frac{6 \times 13.21}{10} + \frac{4 \times 12.69}{10} = 13.002$$

$$Y_{av} = \sum_i s_i Y_i / N_s = \frac{6 \times 4.87}{10} + \frac{4 \times 5.66}{10} = 5.186$$

$$\begin{aligned} SSX_1 &= \sum_i s_i (X_{1i} - X_{1av})^2 \\ &= 6 \times (13.21 - 13.002)^2 + 4 \times (12.69 - 13.002)^2 \\ &= 0.649 \end{aligned}$$

$$\begin{aligned} SX_1Y &= \sum_i s_i (X_{1i} - X_{1av})(Y_i - Y_{av}) \\ &= 6 \times (13.21 - 13.002)(4.87 - 5.186) + 4 \times (12.69 - 13.002)(5.66 - 5.186) \\ &= -0.986 \end{aligned}$$

$$\hat{n} = -\hat{S} = -\frac{SX_1Y}{SSX_1} = -\frac{-0.986}{0.649} = 1.52$$

2. $\mathbf{E_A}$ estimation

$$X_{2i} = \frac{1}{T_i}$$

$$X_{21} = \frac{1}{523} = 1.91\times10^{-3}$$

$$X_{22} = \frac{1}{473} = 2.11\times10^{-3}$$

$$X_{23} = \frac{1}{423} = 2.36\times10^{-3}$$

$$Y_i = ln\,t_{50}(J_i)$$

$$Y_1 = 3.15$$

$$Y_2 = 4.87$$

$$Y_3 = 6.80$$

$$N_s = \sum_i s_i = 4+6+5 = 15$$

$$X_{2av} = \sum_i s_i X_{2i} / N_s = \frac{4\times1.91\times10^{-3}}{15} + \frac{6\times2.11\times10^{-3}}{15} + \frac{5\times2.36\times10^{-3}}{15} = 2.14\times10^{-3}$$

$$Y_{av} = \sum_i s_i Y_i / N_s = \frac{4\times3.15}{15} + \frac{6\times4.87}{15} + \frac{5\times6.80}{15} = 5.055$$

$$\begin{aligned} SSX_2 &= \sum_i s_i (X_{2i} - X_{2av})^2 \\ &= 4\times(1.91\times10^{-3} - 2.14\times10^{-3})^2 + 6\times(2.11\times10^{-3} - 2.14\times10^{-3})^2 \\ &\quad + 5\times(2.36\times10^{-3} - 2.14\times10^{-3})^2 \\ &= 4.59\times10^{-7} \end{aligned}$$

$$\begin{aligned} SX_2Y &= \sum_i s_i (X_{2i} - X_{2av})(Y_i - Y_{av}) \\ &= 6\times(1.91\times10^{-3} - 2.14\times10^{-3})(3.15 - 5.055) \\ &\quad + 6\times(2.11\times10^{-3} - 2.14\times10^{-3})(4.87 - 5.055) \\ &\quad + 5\times(2.36\times10^{-3} - 2.14\times10^{-3})(6.80 - 5.055) \\ &= 3.7054\times10^{-3} \end{aligned}$$

$$\begin{aligned} SSY &= \sum_i s_i (Y_i - Y_{av})^2 \\ &= 4\times(3.15 - 5.055)^2 + 6\times(4.87 - 5.055)^2 + 5\times(6.80 - 5.055)^2 \\ &= 29.947 \end{aligned}$$

$$k_B = 8.617 \times 10^{-5} \text{ (eV/K)}$$
$$\frac{1}{\mathrm{k_B}} = 11605 \text{ (K/eV)}$$

$$\hat{E}_A = k_B \times \frac{SX_2Y}{SSX_2}$$
$$= 8.617 \times 10^{-5} \times \frac{3.7054 \times 10^{-3}}{4.59 \times 10^{-7}}$$
$$= 0.696$$

$$\hat{C} = Y_{av} - (\hat{E}_A / k_B) X_{2av}$$
$$= 5.055 - 11605 \times 0.696 \times 2.14 \times 10^{-3}$$
$$= -12.23$$

$$\hat{Y}_i = \hat{C} + (\hat{E}_A / k_B) X_{2i}$$
$$\hat{Y}_1 = -12.23 + 11605 \times 0.696 \times 1.91 \times 10^{-3} = 3.20$$
$$\hat{Y}_2 = -12.23 + 11605 \times 0.696 \times 2.11 \times 10^{-3} = 4.81$$
$$\hat{Y}_3 = -12.23 + 11605 \times 0.696 \times 2.36 \times 10^{-3} = 6.83$$

$$SSE = \sum_i s_i (Y_i - \hat{Y}_i)^2$$
$$= 4 \times (3.15 - 3.20)^2 + 6 \times (4.87 - 4.81)^2 + 5 \times (6.80 - 6.83)^2$$
$$= 0.0361$$

Caculate the variance of $\hat{E}_A / k_B$, let N is the number of stress tests

$$s^2(\hat{E}_A / k_B) = \frac{SSE}{(N-2)SSX_2} = \frac{0.0361}{(3-2) \times 4.59 \times 10^{-7}} = 78649.24$$

Calculate the two-side confidence interval, let $\alpha = 0.2$,thus the confidence coefficient $1 - \alpha = 0.8$

$$I_{E50}(1-\alpha) = \hat{E}_A \pm \delta_{E50} = \hat{E}_A \pm \frac{t(1-\frac{\alpha}{2}; N-2) \times \sqrt{s^2(\hat{E}_A / k_B)}}{11605}$$

$$= 0.696 \pm \frac{t(0.9;1) \times \sqrt{78649.24}}{11605}, \{t(0.9;1) = 3.078; \text{Ref.}[6], \text{p.}553\}$$

$$= 0.696 \pm 0.074$$

Bibliography

[1] B. A. Lengyel, "Evolution of lasers and masters," *Am. J. Phys.*, Vol. 34, pp. 903-913, 1966.

[2] R.T. Smith and J. D. Chlipala, "Laser programmable redundancy and yield improvement in a 64k dram," *IEEE J. solid-State Circuits*, vol. SC-16, pp. 506-514, Oct. 1981.

[3] J. B. Bernstein, Y. Hua, and W. Zhang, "laser energy limitation for buried metal cuts," *IEEE Electron. Device Lett*., vol. 19, no. 1, pp. 4-6, 1998.

[4] S. S. Cohen and G. H. Chapman, *Laser Beam Processing and Wafer-Scale Integration. New York*: Academic Press, 1989.

[5] S. S. Cohen, P. W. Wyatt, J. A. Burns, and J. B. Bernstein, "The mechanism of laser-induced vertical links," *J. of Electrochem. Soc.*, vol. 138, no. 10, pp. 3013-3018, 1991.

[6] J. B. Bernstein, and B. D. Colella, " Laser-formed metallic connections employing a lateral link structure," *IEEE Trans. Comp. Packag. Manufact. Technol.* A, vol. 18, pp. 690-692, 1995.

[7] J. B. Bernstein, W. Zhang, and C. Nicholas, " Laser formed metallic connections," *IEEE Trans. Comp. Packag. Manufact. Technol.* A, vol. 21, pp. 194-196, 1998.

[8] J. B. Bernstein, "Technique for producing interconnecting conductive links," U.S. Patent 5 861 325, Jan. 19, 1999.

[9] Y. Shen, S. Surech, and J. B. Bernstein, "Laser linking of metal interconnects: analysis and design consideration," *IEEE Trans. Electron Device*, vol. 42, pp. 402-410, 1996.

[10] W. Zhang, J. H. Lee, Y. Chen, J. B. Bernstein, and J. S. Suehle, "Reliability of laser-induced metallic vertical links," *IEEE Trans. Comp. Packag. Technol*., vol. 22, pp. 614-619, 1999.

[11] S. S. Cohen, P. W. Wyatt, G. H. Chapman, and J. M. Canter, "Laser-induced diode linking for wafer-scale integration," *IEEE Trans. on Electron Devices*, vol. 35, no. 9, pp. 1533-1550, Sep. 1988.

[12] S. S. Cohen, P. W. Wyatt, and G. H. Chapman, "Laser-induced melting of thin conducting films: part I – the adiabatic approximation," *IEEE Trans. on Electron Devices*, vol. 38, no. 9, pp. 2042-2050, Sep. 1991.

[13] S. S. Cohen, P. W. Wyatt, and J. B. Bernstein, "Laser-induced melting of thin conducting films: part II – heat-dissipating substrates ," *IEEE Trans. on Electron Devices*, vol. 38, no. 9, pp. 2051-2057, Sep. 1991.

[14] B. S. Yilbas, "Short-pulse laser heating of gold-chromium layers: thermo-elasto-plastic analysis," *J. Phys. D: Appl. Phys*. Vol. 35, pp. 1210-1217, 2002.

[15] S. S. Rao, *Finite element method in engineering*, 2nd Edition, Pergamon Press Inc, Oxford, 1989.

[16] M. R. Frewin, and D. A. Scott, " Finite element model of pulsed laser welding," *Welding Research Supplement*, pp. 15-22, Jan. 1999.

[17] Adrian Bejan, *Heat transfer*, John Wiley & Sons, Inc., Singapore, 1993.

[18] Edward Coyne, "Laser interaction with SiCr thin film resistors – the bubble theory," *IEEE 41st annual international reliability physics symposium*, pp.553-558, 2003.

[19] W. Nowacki, *Thermoelasticity*, 2nd Edition, Pergamon press, New York, 1986.

[20] Tai-Ran-Hsu, *The finite element method in thermomechanics*, Allen & Unwin, Boston, 1986.

[21] S. S. Cohen, J. B. Bernstein, and P. W. Wyatt, “The effect of multiple laser pulses on damage to thin metallic film,” Journal of Applied Physics, vol. 71(2), pp. 630-637, Jan. 1992.

[22] T.L. Anderson, *Fracture mechanics- fundamentals and applications*, CRC Press, Inc., Florida, 1991.

[23] R. J. Sanford, *Principles of fracture mechanics*, Pearson Education, Inc., New Jersey, 2002.

[24] J. H. Lee, W. Zhang, and J. B. Bernstein, “Scalability study of laser-induced vertical make-link structure,” *IEEE Trans. on Semicon. Manufact*., vol. 13, no. 4, pp. 442-447, 2000.

[25] W. Zhang, J. H. Lee, and J. B. Bernstein, “Energy Effect of the Laser-Induced Vertical Metallic Link,” *IEEE Trans. on Semicon. Manufact*., vol. 14, no. 2, pp. 163-169, 2001.

[26] W. Zhang, J. H. Lee, Y. Chen, and J. B. Bernstein, “Reliability of laser-induced metallic vertical links,” *IEEE Trans. on Advan. Packag*., Vol. 22, No. 4, pp. 614-619, Nov. 1999.

[27] J. R. Black, “Electromigration – a brief survey and some recent results,” *IEEE Trans. on Electron Devices*, vol. ED-16, no. 4, pp. 338-347, 1969.

[28] EIA/JEDEC Standard JESD63, “Standard methods for calculating the electromigration model parameters for current density and temperature,” *JEDEC Solid State Technology Association 2000*, Feb. 1998, Virginia, USA.

[29] J. R. Black, “Electromigration failure modes in aluminum metallization for semiconductor devices,” *Proceedings of the IEEE*, vol. 57, no. 9, pp. 1587-1594, 1969.

[30] Cadence™ white Paper, “Electromigration for designers- an introduction for the non-specialist,” Cadence Design System, Inc., 2002, California, USA.

[31] W. Nelson, “Accelerated testing: statistical models, test plans, and data analysis,” John Wiley & Sons, Inc., 1990, United States.

[32] R. E. Jones, Jr. and L. D. Smith, ”A new wafer-level isothermal joule-heated electromigration test for rapid testing of integrated-circuit interconnect,” *J. Appl. Phys*., Vol. 61, No. 9, pp. 4670-4678, May, 1987.

[33] A. Buerke, H. Wendrock, K. Wetzig, "Study of electromigration damage in Al interconnect lines inside a SEM," *Cryst. Res. Technol*., Vol. 35, pp. 721-730, June 2000.

[34] Y.-L. Shen, S. Suresh, and J. B. Bernstein, "Laser linking of metal interconnects: Analysis and design considerations," *IEEE Trans. on Electron Device*, Vol. 43, No. 3, pp. 402-410, Mar. 1996.

[35] A.S. Grove, *Physics and Technology of Semiconductor Devices*, John Wiley & Sons, Inc., 1967, New York.

[36] K. E. Petersen, Dynamic micromechanics on silicon: techniques and devices," *IEEE Transactions on electron devices*, Vol. ED-25, No.10, pp.1241-1250, Oct 1978.

[37] S. Franssila, *Introduction to micro fabrication*, John Wiley & Sons Ltd., Chichester, 2004.

[38] L. T. Lynch, *CRC handbook of material science*, CRC Press, Cleveland, 1974.

[39] X R. Zhang, and X. Xu, "Finite element analysis of the pulsed laser bending: the effect of melting and solidification," *ASME trans. on Journal of Applied Mechanics*, Vol. 71, pp. 321-326, May 2004.

[40] L. G. Shulz, "The optical constants of silver, gold, copper, and aluminum 1. the absorption coefficient K and 2. the index of refraction n," *J. Opt. Soc. Ame*., vol. 44, no. 5, pp. 357-368.

[41] J. H. Lee, *Analysis of laser processing of metal wires used in microelectronics applications,* Ph. D Dissertation, Univ. of Maryland, College Park, 2001.

[42] Moaveni, *Finite element analysis: theory and application with ANSYS*, 2nd Edition, Pearson Education, Inc., New Jersey, 2003.

[43] S. P. Murarka, and S. W. Hymes, " Copper metallization for ULSI and beyond," Crit. *Rev. Solid State Mater. Sci. (USA),* Vol.20, No.2, pp.87-124, 1995.

[44] T. N. Theis, " The future of interconnection technology," *IBM J. Res. Develop*. Vol. 44, No. 3, pp. 379-390, May 2000.

[45] Y.-L. Shen, and E. S. Ege, "Thermomechanical stress in copper interconnect/low-k dielectric systems," *Mat. Res. Soc. Symp. Proc*., Vol. 812, pp.333-338, 2004.

[46] M. Ordal, R. Bell, R. Alexander, Jr. L. Long, and M. Querry, " Optical properties of fourteen metals in the infrared and far infrared: Al, Co, Cu, Au,

Fe, Pb, Mo, Ni, Pd, Pt, Ag, Ti, V, and W," *Appl. Opt*., Vol. 24, No. 24, pp. 4493-4499, 15 Dec. 1985.

[47] K. Forster, and M. Mills, "Screening criteria and property data for new, low-k ILD materials," The Dow Chemical Company Technical Paper, 2003.

[48] M. Morgen, E. T. Ryan, J.-H. Zhao, C. Hu, T. Cho, and P. S. Ho," Low dielectric constant materials for ULSI interconnects," *Annu. Rev. Mater. Sci*., Vol. 30, pp.645-680, 2000.

[49] ASTM Standard F 1260M-96, "Standard test method for estimating electromigration median time to failure and sigma of integrated circuit metallizations," *Annual book of ASTM Standards*, Vol. 10.04, pp. 371-378, 2004.

[50] C. E. Ebeling, *An introduction to reliability and maintainability engineering*, The McGraw-Hill book Co, 1997, Singapore.

[51] M. J. Fagan, *Finite element analysis- theory and practice*, Longman, 1992, Essex.

[52] K. Foster, M. Mills, "Screening criteria and property data for new, low-K ILD materials," Technical paper, *The Dow Chemical Company*, July 2003, U.S.A.

[53] N. Cheremisinoff editor, *Handbook of polymer science and technology*, M. Dekker, 1989, New York.

[54] Richard L. Fox, *Optimization methods for engineering design*, Addison-Wesley Publishing Com., Reading, Massachusetts, 1971.